Dissertation
submitted to the
Combined Faculties for the Natural Sciences and for Mathematics
of the Ruperto-Carola University of Heidelberg, Germany
for the degree of
Doctor of Natural Sciences

Put forward by
M.Sc. Fabián A. Olivares L.
born in: Santiago, Chile
Oral examination: July 27, 2018

Towards Lattice Gauge Theories in Ultracold Mixtures of Sodium and Lithium

Referees: Prof. Dr. Markus K. Oberthaler

Prof. Dr. Matthias Weidemüller

Te recuerdo Amanda.

Zusammenfassung

Diese Doktorarbeit präsentiert die experimentellen Umsetzungen zur Untersuchung von kohärenten Spin-Austausch Wechselwirkungen in ultrakalten Lithium-Natrium-Mischungen. Die Kontrolle und das Verständnis der Spindynamik ermöglicht den ersten Schritt um Gitter-Eichtheorien in diesem Experiment zu implementieren. Aus diesem Grund wurde die Performance des experimentellen Aufbaus untersucht und verbessert, wobei der Kurs der zukünftigen experimentellen Realisationen in Betracht gezogen wurde. Um den räumlichen Überlapp der Lithium und Natrium Atomwolken zu verbessern wurde der vertikale Einschluss der gekreuzten optischen Dipolfalle erhöht. Zusätzlich wurde ein vielseitiges blau-verstimmtes eindimensionales optisches Gitter implementiert, um beide Atomspezies an derselben Gitterstelle zu fangen. Die Charakteristiken und der experimentelle Aufbau wird beschrieben. Für die Untersuchung der Spin-Austausch Wechselwirkungen ist Kontrolle über die internen Freiheitsgrade der Atome essentiell. Die von uns implementierte aktive magnetische Feldstabilisierung wird beschrieben. Weiter wird die Kontrolle über die relative Population zwischen zwei Zeeman-Zuständen des Natrium Grundzustands präsentiert.

Abstract

This thesis presents the experimental implementations towards the investigations of coherent spin-changing collisions in ultracold mixtures of sodium and lithium gases. The control and understanding of such spin dynamics constitutes the first step towards implementing lattice gauge theories in this experiment. For that purpose, the performance of the experimental setup was examined and improved, considering the course of the forthcoming experimental realizations.

To improve the spatial overlap between the atomic clouds of sodium and lithium, the vertical confinement of the crossed optical dipole trap has been increased. In addition, a versatile blue-detuned one-dimensional optical lattice has been implemented to confine both species in the same lattice site. Its characteristics and the experimental setup is described. For spin-changing collision investigations, control over the internal degrees of freedom of the atoms is crucial. We have implemented and described an actively stabilized offset magnetic field. Further, the control over the relative population between two Zeeman states of the sodium ground state is presented.

Contents

1 Introduction

Since the first achievements of Bose-Einstein Condensation, realized using the alkali metals ^{87}Rb [1], ^{7}Li [2] and ^{23}Na [3], ultracold dilute atoms have become an important system for the understanding of quantum mechanics in a variety of physical phenomena [4, 5]. These recognized experimental studies, awarded with the Physics Nobel prize in 2001 [6, 7], were the confirmation of theoretical investigations on quantum gases started 70 years earlier by Bose and Einstein [8, 9], in which a macroscopic occupation of a single quantum state was predicted, when particles with integer spin are brought below a certain temperature.

Several technical developments were crucial for the aforementioned achievements of trapping and cooling down the atoms to degeneracy. These are the development on laser cooling [10, 11], magnetic traps [12], evaporative cooling [13] and on optical dipole traps [14]. These techniques offer a clean control over the system parameters and a good isolation from external disturbances, which positioned the ultracold atoms as an ideal tool to manipulate and engineer a wide range of physical systems. Following from the optical dipole traps, the employment of optical lattices, created by interfering two or more laser beams, allows to further control the spatial distribution of the trapped atoms. Several experimental realizations could study effects beyond the reach of solid-state physics, such as the Josephson effect in superfluids [15], Bloch oscillations of atoms in optical lattices [16] and the Mott insulator phase transition for interacting bosons [17].

Due to the growing interest on ultracold atoms, great experimental effort was put to employ several other alkali metals and isotopes, such as ^{85}Rb [18], ^{39}K [19], ^{41}K [20], ^{133}Cs [21], and non-alkali atoms as well, such as ^{174}Yb [22] and ^{184}Sr [23], used among others, for atomic clock studies [24]. The magnetic species ^{20}Cr [25], ^{164}Dy [26] and ^{168}Er [27], allow to study new regimes of dipolar gases with ultracold atoms.

At the low working densities ($\sim 10^{15}\mathrm{cm}^{-3}$) and temperatures ($< 1\,\mu\mathrm{K}$) of the ultracold gases experiments, the interaction term governing the dynamics of the atomic alkali systems is the two-body s-wave scattering [28]. For particles with small or zero interaction, problems with thermalization, and thus achievement of quantum degeneracy appear. This is the case of spin polarized fermionic gases, where no s-wave scattering exists due to the Pauli principle [29]. An important step towards the expansion of the range that ultracold atoms can explore in physics, are the experimental studies with distinguishable atomic systems that feature sympathetic cooling, where thermalization via the two-body interaction between distinguishable particles contributes to lower the temperature of the studied atomic cloud. This has been implemented for two spin

states of the same atomic species [30], for two isotopes of the same species [31, 32, 33] and two different atomic species [20, 34].

Ultracold atomic mixtures attracted the attention considering the new physics that they allow to study, namely formation of ultracold molecules [35, 36], impurity physics [37, 38, 39, 40, 41, 42] and studies on magnetism [43, 44]. The possibilities to perform such studies were supported by the implementation of the optical dipole traps, due to their spin-independent trapping potential. This lifts the constraint over the spin state of the magnetically trapped atoms, where in non-pure spin clouds, anti-trapped atoms can suffer spin relaxation and induce atomic trap losses due to heating of the atomic sample [45]. Furthermore, another important tool that works together with the optical dipole trapping, is the application and control of an external homogeneous magnetic field allowing to control the scattering parameter between the atoms through the so-called Feshbach resonances [46]. In bosonic systems, studies on the collapse of a BEC have been performed using Feshbach resonances to change the sign of the interaction. In fermionic systems, using Feshbach resonances has allowed to study condensation of molecules formed from two fermionic atoms [35], as well as observation of the BEC-BCS crossover [47, 48, 49, 50].

The possibility to engineer ultracold atomic gases featuring internal degrees of freedom, opened a complete field focused on spinor gases, where the interplay between superfluidity and magnetism plays a central role in the properties of the system [43, 51]. Within the spinor bose gases, the study of nonequilibrium quantum dynamics has attracted the attention due to the rich manifestation of the internal dynamics of the quantum gases. These studies on spin dynamics with spinor bose gases have been performed in degenerate Bose gases [52, 44] as well as in thermal gas systems [53]. Furthermore, spin dynamics has been observed in Fermi gases [54] and in hetero-nuclear Bose gases [55], extending even more the reach of nonequilibrium quantum dynamics studies using ultracold gases.

In this context, our experimental group is focusing its research on the study of hetero-nuclear spin dynamics between a Bose gas of ^{23}Na atoms and a Fermi gas of ^{6}Li atoms [56]. However, due to technical considerations, the natural first step towards the realization of such studies is to work with the bosonic isotope of lithium and implement the Bose-Bose mixture between ^{23}Na and ^{7}Li. The understanding of such systems constitutes the building block towards the implementations of lattice gauge theories using a mixture of ^{23}Na and ^{6}Li [57, 58]. Gauge theories are a fundamental ingredient of the Standard Model of particle physics, but they are very difficult to study, both theoretically and experimentally. In that regard, ultracold atom experiments are a promising candidate to simulate such systems and provide high flexibility over parameters otherwise hard to tune. Specifically, our goal is to build an analog quantum simulator for quantum electrodynamics in 1+1 dimensions through quantum link models [57, 58, 59]. The gauge-invariant interactions will be experimentally implemented via

coherent spin-changing collisions between fermions and bosons. It is thus important to have a well understanding and control over the coupling and dynamics of such spin states.

This Thesis

The progress made in the experimental system is a result of the team work of all the members of the NaLi experiment at that time, specially Alexander Mil (PhD student).

This thesis describes our experimental setup used to produce ultracold atoms of sodium and lithium, as well as the modifications and hardware updates implemented towards the realization of coherent spin-changing collisions studies between sodium and bosonic lithium. At the beginning of my PhD, I learned how to operate the experimental machine while collaborating with the previous PhD students, Tobias Rentrop and Arno Trautmann. At that moment, the studies were focused on impurity physics, leading to the observation of the phonon-induced Lamb Shift [60]. When they finished and I started working in the machine, although the experiment was operational, its stability was not optimal. Several sections of the experiment needed to be improved. We focused on the investigation, identification and solution of those problems. The main sign that indicated stability problems in the experiment was given by the shot-to-shot fluctuations on the atom numbers. For instance, at that time the laser source used for the sodium atoms was a dye laser. During the time working with such laser system, it was quite common to invest at least $30\,\mathrm{min}$ to $1\,\mathrm{hr}$ at the beginning of each day to achieve the laser running at the correct wavelength and with a sufficient output power.

We investigated each section of the experiment in order to improve the performance. Those sections comprise the vacuum setup, with the different chambers and pumps. The laser setup for both species, including the replacement of the sodium dye laser. The magnetic trap coils, including the water cooling system used to cool down the coils.

After major modifications performed in the experiment, we could create Bose-Einstein Condensates of both sodium and lithium. We increased the magnification of the imaging system and obtained in-situ images of the atoms confined in an effective dipole trap, which consists of the crossed dipole trap along with a new one-dimensional optical lattice. Continuing with the upgrade of the experiment in order to investigate coherent spin dynamics in our system, we performed spectroscopy studies to calibrate a newly implemented actively stabilized offset magnetic field via a magnetic sensitive transition of sodium [1].

[1] At the end of the work here presented, our experiment had high pressure problems which appeared after refilling the oven source and continued during several months.

Outline of the Thesis

Chapter 2 In this chapter we describe the experimental setup and the different steps needed to produce ultracold gases of sodium (^{23}Na) and lithium (^{6,7}Li).

The chapter starts by describing the dual-species oven used to create the atomic beam of sodium and lithium. The influence of the oven in the overall performance of the experiment is discussed. Further, this chapters describes the characteristics of the cooling and trapping procedures for both sodium and lithium, starting from the MOT, continuing with the magnetic trapping, to finally describe the confinement of the atoms in a crossed optical dipole trap. The optical setup for both species is presented, as well as the changes introduced on both of them. The new setup implemented for the imaging is also described.

Chapter 3 This chapter focuses on the experimental techniques used to trap and confine the atoms with optical dipole traps. An overview of the theory of atoms in detuned laser beams, that gives origin to the optical dipole traps is presented. The characteristics of optical lattices are also explained. We discuss the influence of the gravitational acceleration on the effective potential of trapped atoms. We explained the changes done on the crossed optical dipole trap (ODT) in order to reduce the differential gravitational sag. We show qualitative results on Bose-Einstein Condensation of sodium atoms in the new crossed ODT. The design and implementation of a versatile new one-dimensional optical lattice is presented.

Chapter 4 The control and manipulation of the spin degree of freedom of the trapped atoms is investigated in this chapter. In order to exploit the magnetic sensitivity of the different Zeeman states of the atoms, an actively stabilized offset magnetic field is described and implemented. We present Rabi and Ramsey spectroscopies performed by driving the magnetic sensitive transition $|1,1\rangle \longrightarrow |2,2\rangle$. Additionally, we address the time limitation of our MW setup which requires a minimum time to give a second pulse after a first pulse has been delivered. We describe how that limitation is solved by the addition of a MW switch in the same MW line. Further modifications to the MW setup that allow us to manipulate the relative population between the states $|1,0\rangle$ and $|1,1\rangle$ for sodium are described. Finally, we discuss the the experimental procedure to perform a Stern-Gerlach separation, which allow us to obtain information about the population of the different Zeeman states via absorption imaging.

2 Production of Atomic Samples: From a Dual-Species Oven to an Ultracold Gas

This chapter describes the experimental steps required to produce the ultra-cold atomic clouds, as well as the important changes we introduced in our experimental setup aiming for a better performance and stability.

2.1 Atomic Source and Vacuum

The first component of any experiment working with cold atoms is the atomic source. This section will describe the initial hardware of our experiment, explaining where the atomic beam is produced and how the pressure is managed along the experimental chamber. The characteristics of performance of the oven are discussed. The experimental chamber is described, including its different sections and diagnostic elements.

2.1.1 Dual Species Oven

At the beginning, sodium and lithium atoms are evaporated in the same oven to produce an atomic beam, which is then used to load the magneto-optical trap (MOT). The oven is build from stainless steel, following the oven design of Ketterle's group [61]. It consist of three main sections as depicted in Figure 2.4 and in Figure 2.5. Solid chunks of sodium and lithium are deposited inside their separated reservoirs by means of the CF40 flanges placed on top of the oven. The reservoirs are heated up independently until temperatures close to $350\,^{o}\mathrm{C}$ to achieve a high atomic flux. The CF40 flanges are sealed using nickel gaskets as they can stand higher temperatures and do not show chemical reactions with neither sodium nor lithium, as it was the case when using copper gaskets. A small tube of $5\,\mathrm{mm}$ of diameter called mixing nozzle connects the two reservoirs. Due to its higher vapor pressure, sodium vapor enters the lithium chamber through the mixing nozzle, as we can notice, the lithium chamber contains the lithium chunks and it also works as mixing chamber. From here, atoms leave the mixing chamber through a $4\,\mathrm{mm}$ diameter hole (oven nozzle) arriving into the collimation chamber, the last chamber of the oven. To avoid clogging of the nozzles, heating clamps

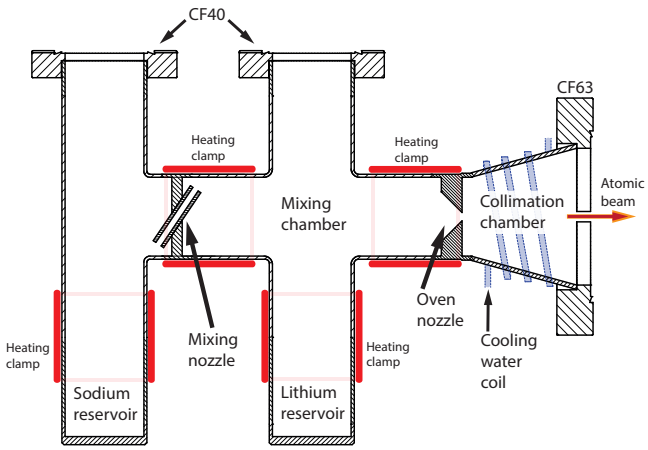

Figure 2.1: Sketch of the used dual species oven. We can see the different chambers of the oven. The sodium chamber is separated and connected to the lithium chamber only through the mixing nozzle. The lithium reservoir works also as a mixing chamber. The cooling water passing through the hollow coil wrapped around the collimation chamber was removed resulting in a better atomic flux.

are placed to keep a temperature of $450\,^{\circ}\mathrm{C}$ on each nozzle. Collimation of the atomic beam is done by the oven nozzle together with the exit nozzle of the oven, of $5\,\mathrm{mm}$ of diameter separated by a distance of about $6\,\mathrm{cm}$. Atoms with a velocity parallel to the axis of the collimation chamber will travel directly into the Zeeman slower and into the glass cell. The conical shape of the collimation chamber allows us to connect the oven to the main experiment via a CF63 flange.

Among the drawbacks with the current oven design, the main one is the difficulty to achieve a reliable high atomic flux coming from the oven. A low atomic flux will result in a poor loading of the MOT and, therefore, low atom numbers in the subsequent steps of the experiment. Increasing the reservoir temperatures increases the atomic flux but it also reduces the MOT lifetime. There are two ways to run the oven temperatures. One approach is to have two temperature states, one for the day, during the working hours ($360\,^{\circ}\mathrm{C}$ for Na and $380\,^{\circ}\mathrm{C}$ for Li) and the second for the night during idle hours ($280\,^{\circ}\mathrm{C}$ for Na and $300\,^{\circ}\mathrm{C}$ for Li). This method allowed to have a high atomic flux but it increases the pressure as well. Therefore, cooling water was installed around the collimation chamber in order to reduce stray atoms wandering around resulting in a pressure increase. Nevertheless, pressure rises during operating hours were impossible to avoid. Additionally, it is detrimental in the long term as it stresses the material due to the constant temperature change. Our most recent approach is to keep the reservoir

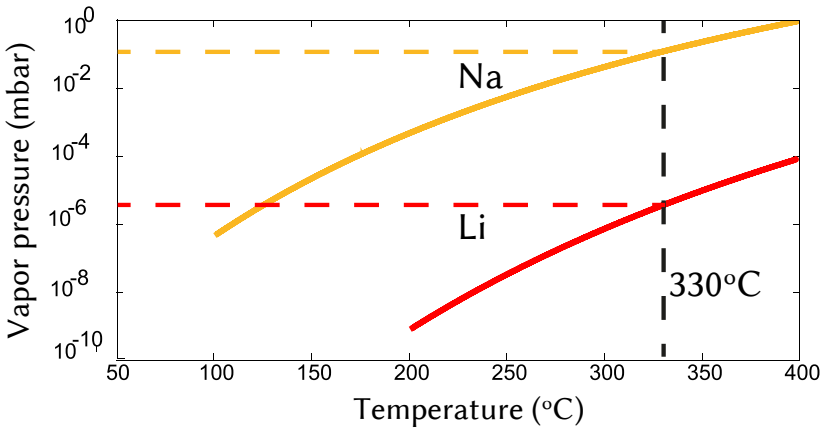

Figure 2.2: Vapor pressure for sodium (yellow, upper) and lithium (red, lower) with respect to the temperature. The vapor pressure of sodium is higher than the vapor pressure of lithium at the same temperature. The vertical dashed line represents the usual working temperature of the dual species oven. Adapted from [62].

temperatures at a constant value in between the previous ones, i.e at around $330\,^{o}\mathrm{C}$. We also removed the cooling water around the collimation chamber, obtaining a good constant flux that allowed us to run the experiment for several months without any temperature adjustment.

When operating the reservoirs with the method of day-and-night temperatures, life span of the material was always close to $1\,\mathrm{year}$. On the other hand, by having the reservoirs at constant temperature, we could run the experiment for more than $1.5\,\mathrm{year}$. Nevertheless, none of the two methods is conclusive as the atomic beam is not reliable in the long term. At the moment, after all the knowledge acquired while working with our current oven, a new oven with a better collimation is being designed. Once the oven starts to empty its reservoirs, the recurrent indications that signal it, are a sudden pressure rise and a decrement of the MOT loading rate, as expected. This is the time when new material chunks need to be introduced into the oven.

The vacuum has to be broken in order to refill the oven. Our vacuum apparatus, which will be described later, features gate valves that can isolate the glass cell chamber, preventing it from contamination that can enter during the refilling. The recommended procedure is to vent the chamber with high purity dry nitrogen beforehand and keep it at room pressure. Once the chamber has been flooded with nitrogen, CF40 flanges on top of the oven can be opened and new material is introduced. As the natural abundance of ^{6}Li is very low, we introduce the same amount of natural ^{7}Li and enriched ^{6}Li. The venting gas will reduce the amount of air entering and contaminating the walls of the

apparatus, which will require longer pumping times in order to achieve low pressures again. Once the material has been introduced, flanges have to be sealed with new nickel gaskets and pumping can be started.

Even though safety measures are followed carefully, it is impossible to achieve working pressures immediately after an oven refilling. Apart of the time needed to pump down the pressure, the chamber walls will acquire surface coverage due to being exposed to the atmospheric gas load as well as the introduced material into the oven.. Cleaning procedure of the chamber is done by heating up the oven and the walls of the apparatus in a standard procedure called bake-out. Large amounts of gas produced during the bake-out are pumped out of the vacuum chamber with a turbo-molecular pump (Varian Turbo-V 70LP). Furthermore, oxide layers on the metal chunks due to air contact have to be removed by heating the reservoirs up to $500\,^{\circ}\mathrm{C}$ for short period of about $15\,\mathrm{min}$. The rest of the apparatus is heated up to $200\,^{\circ}\mathrm{C}$, except the part that were not exposed to dry nitrogen. High temperatures of the bake-out will speed up the out-gassing rate of the contamination deposited on the walls, resulting in a faster achievement of low pressures compared to pumping down the chamber at room temperature as shown in Figure 2.3.

2.1.2 Vacuum setup

Our vacuum apparatus consists of three chambers, we call them: oven, pumping stage, and glass cell chambers, connected via small diameter tubes. Each chamber has its respective ion pump. The oven chamber, first chamber according to the direction of the atomic beam, is a 6-way cross where the oven joints the system. Its normal working pressure is the highest, $\sim 1 \times 10^{-8}\,\mathrm{mbar}$. Along with being connected to the pumping stage chamber, it has a rear arm that can be opened by means of a gate valve and an edge valve. This arm leads to the turbo pump and elements used during bake-out: A pressure gauge, a mass spectrometer and a ventilation valve. During bake-outs we can monitor the pressure and mass spectrum of the gas load in our vacuum. Once good enough pressure has been achieved, we can separate those elements from the experiment. At this point we can turn on the ion pump (Agilent Diode, $55\,\mathrm{l/s}$). This chamber also contains the atomic beam shutter that blocks the beam of atoms once the MOT has been loaded. It consists of a magnetic feed-through shutter (Lesker, DS450VPS) controlled by a servo motor (BMS-661DMG HS).

The next chamber is the pumping stage chamber. As its name points out, this 4-way cross chamber is connected to the oven chamber via a small pumping tube $80\,\mathrm{mm}$ long. The tube has a conical shape, its diameter is $5\,\mathrm{mm}$ on the end that faces the oven, whereas the other side has a diameter of $7\,\mathrm{mm}$. The pressure can be reduced by two orders of magnitude thanks to the low conductivity of the pumping tube and the ion pump in this chamber (Agilent Starcell VacIon 55). Normal working pressure is on the order of $1 \times 10^{-10}\,\mathrm{mbar}$. Both ion pumps, from oven and pumping stage

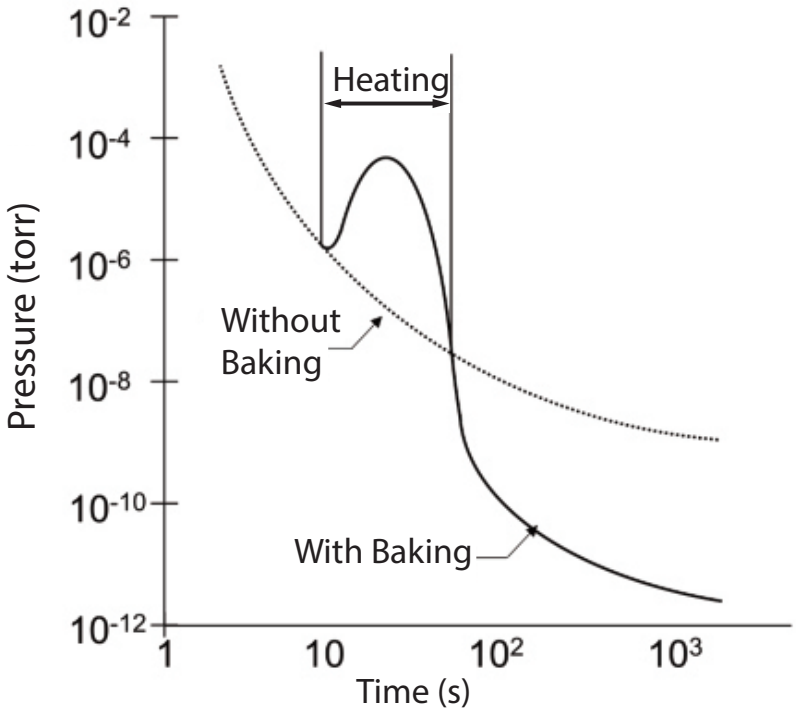

Figure 2.3: Effect of baking on the outgassing rate. Heating the walls of the vacuum chamber increases the outgassing rate of the adsorbed molecules allowing us to reach a low pressure in a shorter period of time compared to time required to reach the same pressure but only pumping the chamber without baking the walls. Adapted from [63].

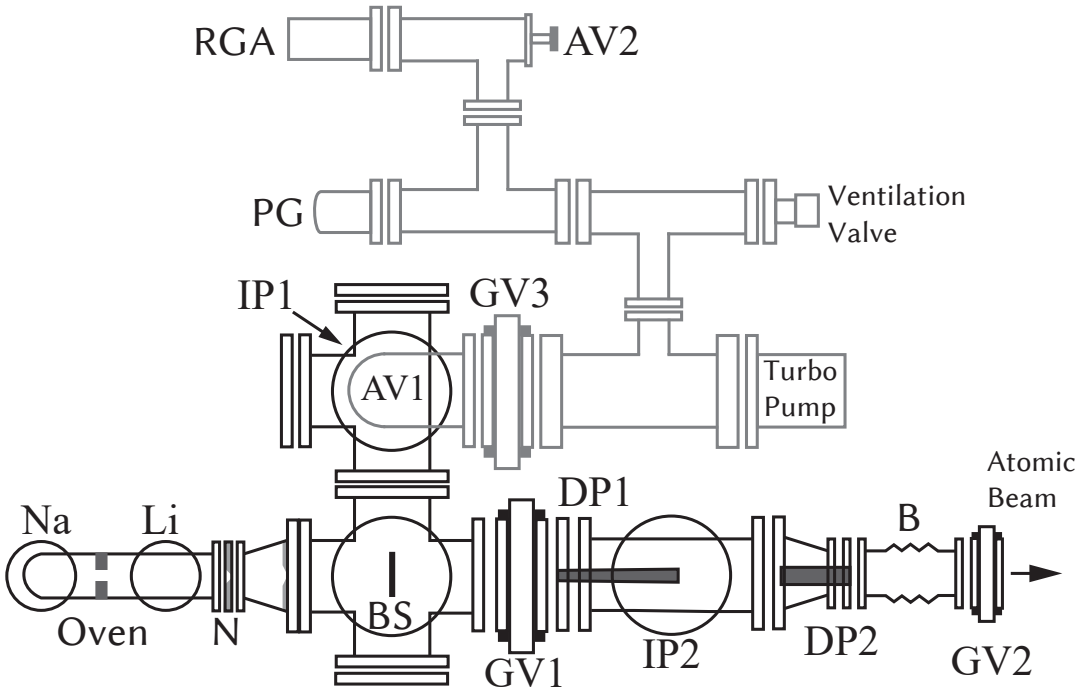

Figure 2.4: Top view. Schematics of the front part of the vacuum setup. The main line of the vacuum setup is connected to the glass cell section by a gate valve (GV2). The elements of the main line are drawn with black lines. The elements in gray are installed at a higher height connected by an angle valve (AV1). In the main line, the atomic beam escaping from the oven can be blocked with the atomic beam shutter (BS) installed in the oven chamber, which is a 6-way cross. The oven ion pump (IP1) is installed in this chamber as well, on a second 6-way cross. Following the atomic beam path, atoms enter the pumping-stage chamber passing through the first gate valve (GV1) and the tapered pumping stage tube (DP1) that collimates the beam. The second ion pump (IP2) is installed in this 4-way cross chamber. In order to continue to the glass cell section in Figure 2.5, the atoms pass through the second pumping tube (DP2), a bellow (B) and the second gate valve (GV2). In the higher line are the components used to ventilate and diagnose the vacuum after the oven has been refilled. These are: a gate valve (GV3), the turbo pump connected to a roughing pump. A ventilation valve. A Bayard-Alpert gauge (PG) and the residual gas analyzer (RGA) that can be separated with an angle valve (AV2). Adapted from [64].

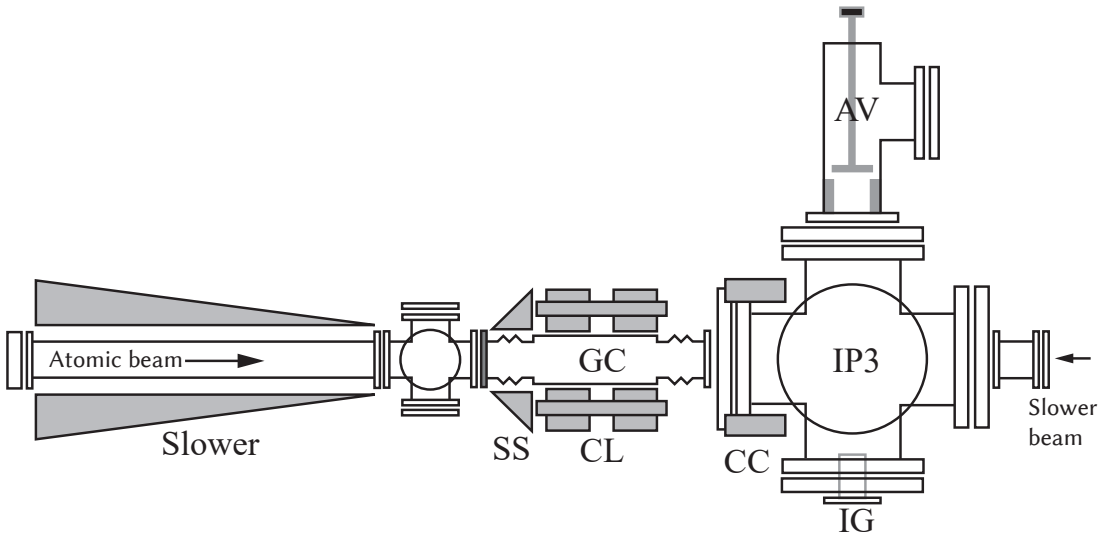

Figure 2.5: Top view. Schematics of the rear part of the vacuum setup, where glass cell is located. Top view. Atoms travel through the slower beam to finally been captured in the glass cell (GC). The cloverleaf trap array (CL) is shown close to the glass cell as well as the small slower (SS) and the compensation coils (CC). The combination ion pump (IP3) is installed in the last 6-way cross after the glass cell, together with the ion gauge (IG) and an angle valve (AV) that gives the possibility to install a turbo pump. The rear face of the 6-way cross features a viewport to let the slower beam enter into the vacuum system. Adapted from [64].

chambers, were installed recently as the performance of the previous ones was not optimal. Another important change in this section was the replacement of the gate valve (HVA 11120-0254) that can separate these two chambers. The previous gate valve was not leak tight anymore as it was coated with the material coming out of the oven after several years of operation. This gate valve is important as it will allow us to refill the oven by breaking the vacuum only in the oven chamber, reducing bake-out times afterwards. Once the machine is running, the pressure reading is estimated from the current reading on the ion pump controller. This is the case for both oven and pumping stage chambers. Although having pressure gauges would be beneficial to know the pressure in the different chambers, the heat generated by them and the difficulty to bake them at very high temperatures is the reason for not installing them.

The last chamber is where the UHV glass cell and the experiments are performed. This chamber can be separated from the previous one by a gate valve as well (MDC E-GV 1500M). A pumping tube $80\,\mathrm{mm}$ long and with a diameter of $10\,\mathrm{mm}$ helps reducing the pressure by one order of magnitude from the pumping stage chamber. A bellow installed between the gate valve and the pumping tube helps centering the atomic beam onto the MOT position. A normal working pressure in the glass cell chamber is in the 10^{-11} mbar regime. This low pressure is achieved by an ion pump, Varian VacIon Plus 150 Combination Pump, which has a titanium sublimation pump to increase the overall pumping speed up to $500\,\mathrm{l/s}$. The pressure is monitored by a Bayard-Alpert ion gauge. The pumps and the ion gauge are attached to the 5-way cross placed immediately after the glass cell. Finally, the atomic beam hits the viewport where the slower beam enters into the apparatus. To avoid lithium to coat the viewport and be detrimental for the slower beam, we constantly heat the viewport area up to $160\,^{\circ}\mathrm{C}$. The lowest detectable pressure of the ion gauge is $2 \times 10^{-11}\,\mathrm{mbar}$. During normal working periods, the ion gauge reading will show error, meaning this threshold has been surpassed.

2.2 Cooling and Trapping

The first step towards the realization of experiments with ultracold atoms is the cooling and trapping of the atoms. This is done in our experiment by means of lasers and magnetic fields. This section describes our equipment and the techniques used for that purpose. Importantly, our laser setup consists of two laser systems, one for each atomic species. They will both be described as well as the introduced updates. Following the experimental sequence, the magnetic trapping is described together with the further cooling procedures such as evaporative cooling in the magnetic trap. Finally, our current crossed optical dipole trap setup is described.

2.2.1 Laser system

Sodium

The laser setup for sodium uses a single source to generate laser light for different purposes: spectroscopy, cooling and repumping. The cooling transition is the D_2-line, at $589\,\mathrm{nm}$ [65]. During the course of this thesis, the laser source for sodium was exchanged. The former ring-cavity laser was a dye laser from Radiant Dyes in bow tie configuration that could typically output a power of $1.2\,\mathrm{W}$. The dye laser system consisted of the cavity, the dye solution being circulated by a 18 bar pump, and the pump laser (Laser Quantum Finesse, $532\,\mathrm{nm}, 14\,\mathrm{W}$) The pump laser excites the dye molecules in the dye solution. Several issues were encountered when working with this dye laser, the most important being the unreliable output power level of it. During the times working the dye laser, the daily routine consisted on at least $1\,\mathrm{h}$ adjusting the cavity to obtain enough output power. Within the same day, temperature changes in the dye solution, due to the constant contact with the $14\,\mathrm{W}$ pump laser power would cause a slowly but steadily power drop. Furthermore, aging of the dye solution also resulted in a reduction of the output power, requiring to change the dye after 4 months of normal operation. Further discussions can be found in [42].

When the new laser arrived, the dye laser setup was completely unmounted. The new laser system is the TOPTICA SHG Pro, a frequency-doubled amplified diode laser. Its seed laser is a DL pro at $1178\,\mathrm{nm}$, which is doubled in the SHG cavity to obtained the required $589\,\mathrm{nm}$ as seen in Figure 2.6. The output power can be set up to 1.5W and is stabilized by the internal power monitoring electronics of the laser. The laser frequency is locked using a commercial vapor cell (Thorlabs CP25075-NA) via Doppler free saturation spectroscopy. In the locking setup, the pump beam is modulated via a $71\,\mathrm{MHz}$ AOM in double pass configuration on the $+1$ order, resulting in a frequency shift of $71\,\mathrm{MHz}$ on the master laser. The error signal employed to lock the laser is obtained from a lock-in amplifier referenced to the same modulation frequency of about $20\,\mathrm{kHz}$ the AOM is modulated with. The locking transition is the crossover $F = 2 \rightarrow F' = 2, 3$.

On our optical table the main laser beam is divided into the following: Imaging, MOT, repumper, slower, umpump and umpump repumper. Frequency shifts relative to the main laser beam are accomplished with AOMs in single pass configuration, except the beam used for spectroscopy as already mentioned. The majority of our AOMs are from Gooch and Housego with the exception of the $1.7\,\mathrm{GHz}$ AOM (TEF-1700-100-589, Brimrose Corp) used on the repumper path, which is an uncommon AOM due to its $1.7\,\mathrm{GHz}$ of working frequency. The mounting of this AOM was always a critical factor within the sodium beam path. It was quite common to see that its efficiency changed from one day to another or even within the same day. In order to improve its mechanical stability we changed its mount from a two-axis mount to a five-axis mount (Newport

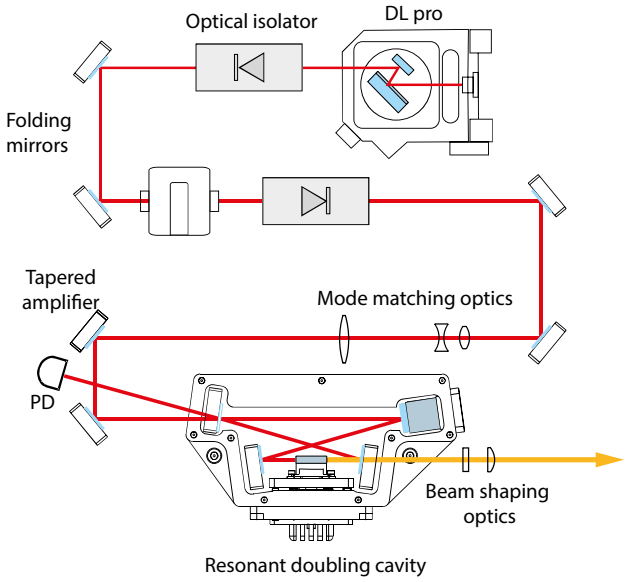

Figure 2.6: Schematics of the TOPTICA SHG Pro. The infrared seed laser from the DL pro is amplified in the Tapered Amplifier (TA) unit. Afterwards, it is mode matched to the cavity crystal mode in order to maximize the doubling frequency and the output power. After the doubling cavity unit, the beam has the required wavelength of 589 nm. Adapted from *TOPTICA Tunable Diode Lasers* Brochure.

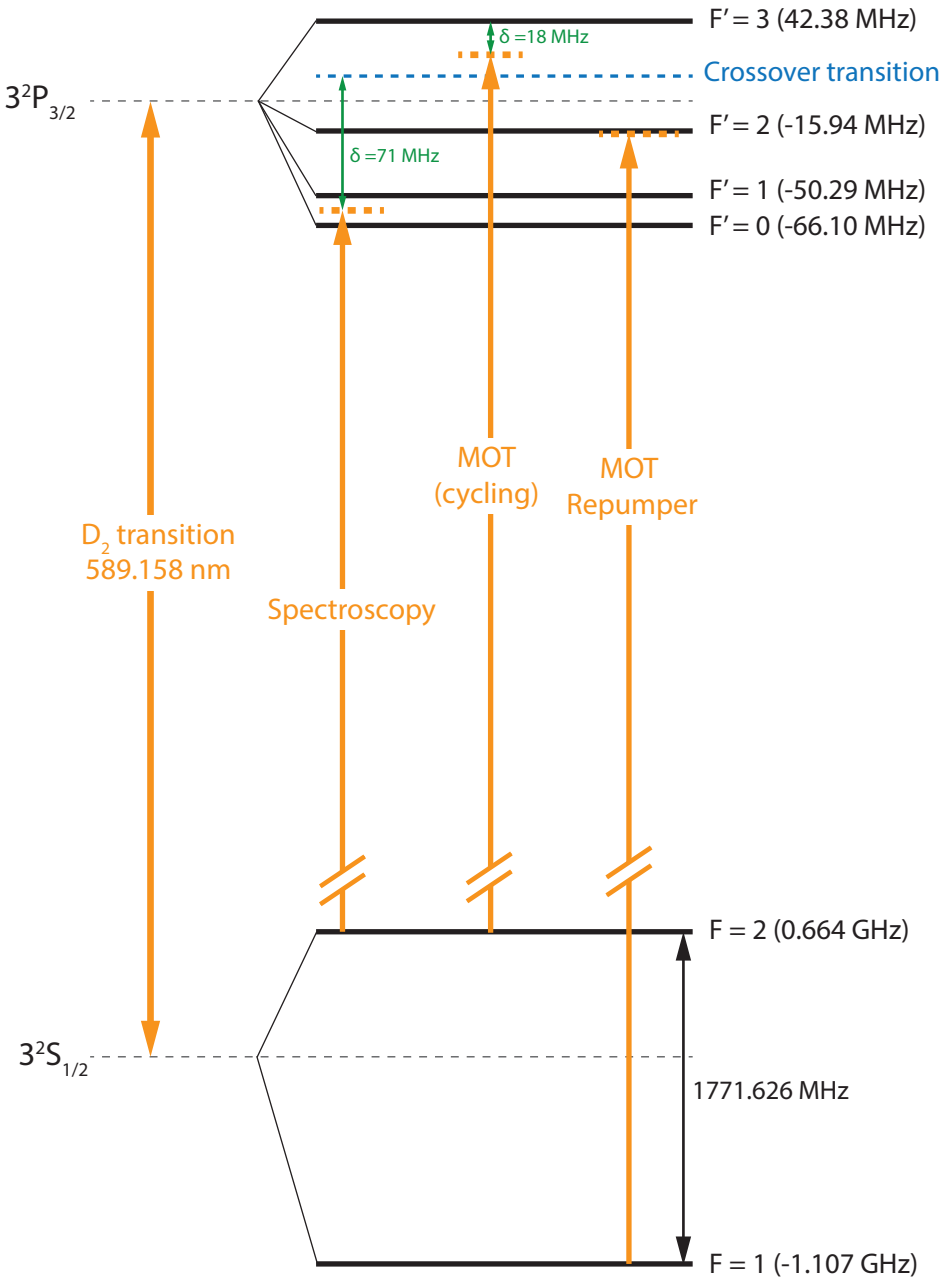

Figure 2.7: Scheme of the transitions used for the cooling and repumping beams for sodium. The laser is locked to the crossover between $F' = 2$ and $F' = 3$. Using an acousto-optic modulator with an RF-frequency of $+ 71\,\mathrm{MHz}$ in the spectroscopy setup, the laser frequency is shifted to the red by the same amount.

9082-M). The reasoning behind choosing the five-axis stage was the spatial constraint on the optical table to have only one mirror before the AOM but also because this new stage is more stable. Stability improved substantially and we could run the experiment for weeks without the need to re-align the big AOM. Its efficiency is on the order of 5 to $10\,\%$. The schematics for the optical setup for the sodium system can be seen in Figure 2.8.

As our optical table is separated from the experimental table, all of our beams, except for the slower, are fiber injected to be transported onto the experimental table. We updated two fiber in-couplers, corresponding to two MOT beams (front and back), because the previous ones were not adjustable. The new couplers are the same ones used for the other fibers, Schäfter & Kirchhoff 60FC-4-M8-33. This change was useful, especially after the main laser was exchanged, because we had to completely adjust and recouple the beam path.

Lithium

The lithium laser system starts differently when compared to the sodium laser system. In the lithium setup there are two lasers sources for the required beams. The master laser is a homebuilt diode laser in external cavity configuration that it is locked in the same way the sodium laser is locked. The vapor cell is a homebuilt heated pipe containing both ^{6}Li and ^{7}Li [66]. It is heated up with a heating clamp to $350\,^{\circ}\mathrm{C}$ during the day and kept at $100\,^{\circ}\mathrm{C}$ over night. The absorption signal is obtained from Doppler free saturation spectroscopy and error signal is obtained from a lock-in amplifier, as done with sodium. Both isotopes are locked to the D_2-line, at around $671\,\mathrm{nm}$. ^{6}Li is locked to the dip of the transition from $F = 3/2$ to the upper manifold F' and ^{7}Li is locked to the dip of the transition from $F = 2$ to the upper manifold F'. The time required to change the lock from one isotope to the other is $\sim 30\,\mathrm{min}$. The temperature of the master laser has to be slightly changed in order to get the other absorption line and the time it takes the temperature control to settle down is the main limitation for this procedure. During the writing of this thesis, the master laser has been exchanged for a DL Pro laser from TOPTICA. It is expected to make those changes faster, along with better stability.

The slave laser is an amplified diode laser from TOPTICA TA Pro, it is specified for a wavelength of $671\,\mathrm{nm}$ with a typical output power of $350\,\mathrm{mW}$. It is locked to the master laser using an offset beat-lock scheme, as explained in [67]. The beat-lock signal is obtained after overlapping both beam on a photodiode, which is mixed with a fixed reference frequency and filtered afterwards. The resulting signal is proportional to the frequency difference between the master and the slave laser. The latter is locked to this beat-lock signal, meaning that by changing the fixed reference frequency we can change the relative frequency between both lasers. The reference frequency that is mixed with the beat signal is created with a tunable voltage controlled oscillator (VCO).

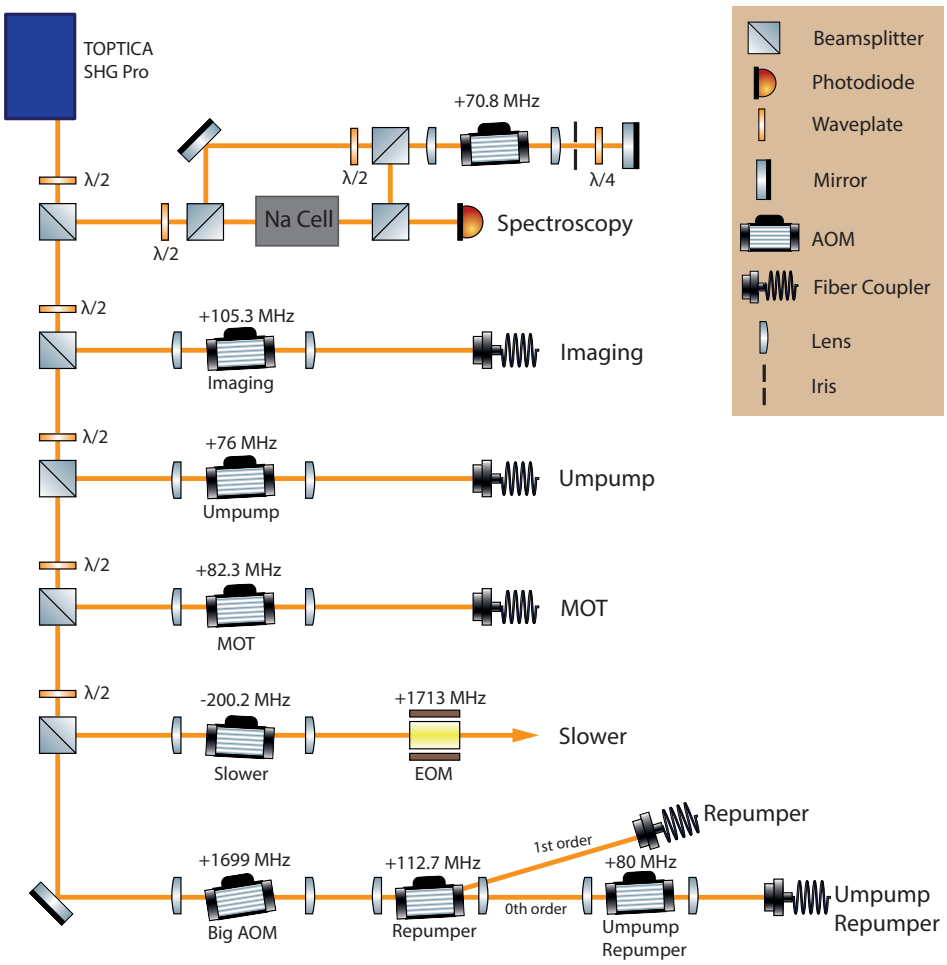

Figure 2.8: Optical setup for sodium. The TOPTICA SHG Pro laser source is used for all the necessary frequencies. [1]

[1] ComponentLibrary by Alexander Franzen is licensed under a Creative Commons Attribution-NonCommercial 3.0 Unported License.

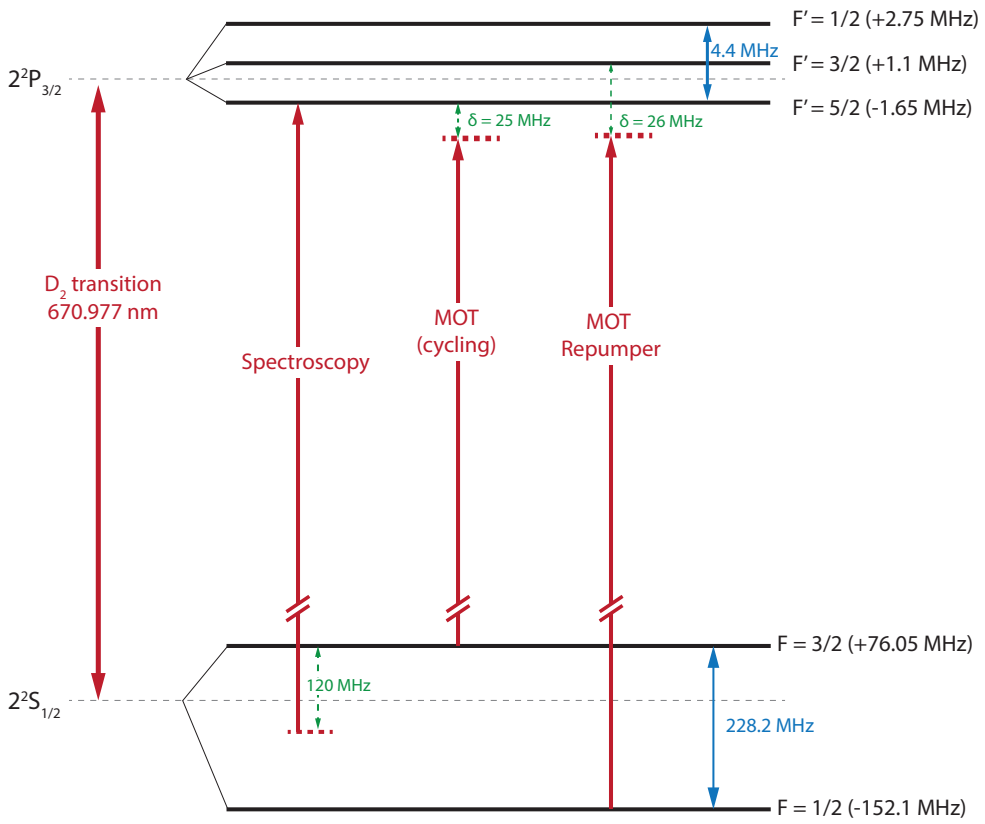

Figure 2.9: Scheme of the transitions used for the cooling and repumping of ^{6}Li. The master laser is locked to the resonance $F = 2 \rightarrow F'$. In the spectroscopy setup, the pump beam is modulated with a $-120\,\mathrm{MHz}$ AOM , therefore the laser frequency is shifted to the blue by the same amount.

In our implementation, we can adjust the relative frequency between both lasers in a range from $0\,\mathrm{MHz}$ to $200\,\mathrm{MHz}$ [66].

The Li beam path concept is similar to the one used for sodium. Several AOMs produce the required frequencies which are then injected into different optical fibers that take the light to the experimental table. It is important to point out that lithium and sodium light are coupled into the same fibers. As it was mentioned before, our experiment can work with two isotopes of lithium. Historically, our Li setup was build for ^{6}Li, therefore the implementation of ^{7}Li was done such that not many changes had to be introduced into the existing setup. This could be achieved without much difficulties because their energy levels are similar. The main difference is the different hyperfine splitting of the ground state, as it can be seen in Figure 2.9 and in Figure 2.10. For ^{6}Li, the splitting is $228\,\mathrm{MHz}$, whereas for ^{7}Li it is $805\,\mathrm{MHz}$.

Before implementing the ^{7}Li setup, several options were discussed as described in [66]. In the ^{6}Li setup, MOT and repumper beams are both $20\,\mathrm{MHz}$ to $30\,\mathrm{MHz}$ red detuned with respect to the upper manifold. The implemented setup for ^{7}Li features an extra AOM ($\mathrm{AOM}_{7\mathrm{Li}}$) in double-pass configuration that is added to the repumper beam path in order to cover the ground state splitting of $805\,\mathrm{MHz}$. Detailed description of the repumper path is: master laser is locked to the $F = 2 \rightarrow F'$ transition with a modulated AOM working at $120\,\mathrm{MHz}$ on the -1 order. In absence of an offset lock, that would translate to a blue shift of our slave laser by $120\,\mathrm{MHz}$. In our experiment, an offset frequency of $65\,\mathrm{MHz}$ is present during the MOT phase, therefore, we are $55\,\mathrm{MHz}$ blue detuned after the spectroscopy lock. Taking as a reference the repumping transition $F = 1 \rightarrow F'$, we are $750\,\mathrm{MHz}$ red detuned. The next element is the repumper AOM working at $150\,\mathrm{MHz}$ on the $+1$ order. Up until now, the setup is exactly to ^{6}Li setup. Now in the extra part for ^{7}Li, the beam path continues on the double pass through $\mathrm{AOM}_{7\mathrm{Li}}$ that is working at $290\,\mathrm{MHz}$ on the $+1$ order. The resulting beam is a repumper beam $\sim 30\,\mathrm{MHz}$ red detuned.

Even though the ^{7}Li implementation worked out well, its performance was limited by the power of the repumper beam. This limitation came from the efficiency of $\mathrm{AOM}_{7\mathrm{Li}}$ that was around $25\,\%$ after the double pass, reducing enormously the available power. In order to solve this limitation we did two changes: We replaced the AOM model with another more suitable to the RF frequency. And secondly, we added a homebuilt tapered amplifier (TA) to the repumper beam path. The TA design is described in [68].

The input RF frequency of $\mathrm{AOM}_{7\mathrm{Li}}$ is $290\,\mathrm{MHz}$ and the previous AOM was specified to $350\,\mathrm{MHz}$. Usual AOMs bandwidth is $\pm\ 25\,\mathrm{MHz}$, explaining its low performance with $290\,\mathrm{MHz}$ of RF frequency. We changed the AOM for a $270\,\mathrm{MHz}$ unit from the same company Gooch and Housego. After recoupling the beam path we could obtain an efficiency of about $55\,\%$.

The power loss caused by the fact that $\mathrm{AOM}_{7\mathrm{Li}}$ is in the beam path affected negatively the performance of ^{7}Li MOT. This could be seen in the $20\,\mathrm{s}$ of MOT loading time, a factor of two slower compared to ^{6}Li. To get more repumper power, a homebuilt seeded TA laser was installed in the repumper beam path. The TA is located after the double pass $\mathrm{AOM}_{7\mathrm{Li}}$ setup, on a breadboard that receives and returns the repumper light from the main optical path via optical fibers. The use of optical fibers ensures us to seed the TA and the forthcoming slower AOM with a Gaussian beam. The TA amplifies the repumper beam from a seed power of about $15\,\mathrm{mW}$ to an output power around $400\,\mathrm{mW}$. Due to the bad mode of the output beam of the TA, the efficiency of the optical fiber that brings the beam back to the main optical path is $20\,\%$, deriving in a repumper beam of about $80\,\mathrm{mW}$. This is enough compared to the $70\,\mathrm{mW}$ of repumper power we had for ^{6}Li before including the $\mathrm{AOM}_{7\mathrm{Li}}$ arm. Schematics of the optical setup for lithium can be seen in Figure 2.11.

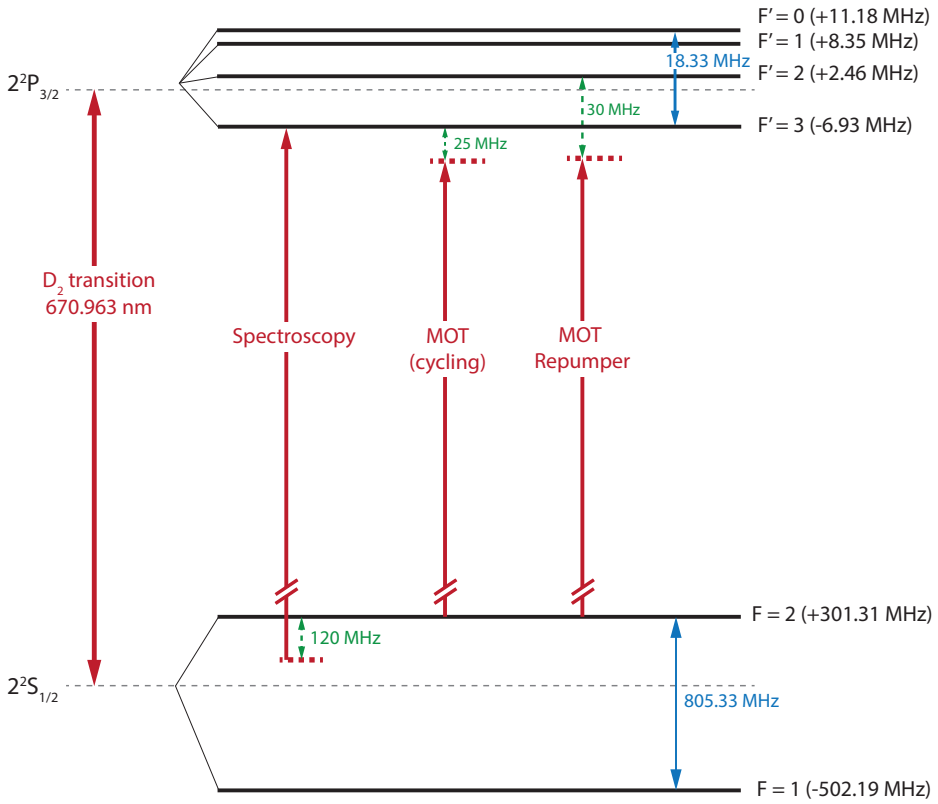

Figure 2.10: Scheme of the transitions used for cooling and repumping of ^{7}Li. Locking setup is the same as for ^{6}Li. Main difference in frequency is the splittin energy of 805.33 MHz of the ground state compared to the 228.2 MHz of ^{6}Li.

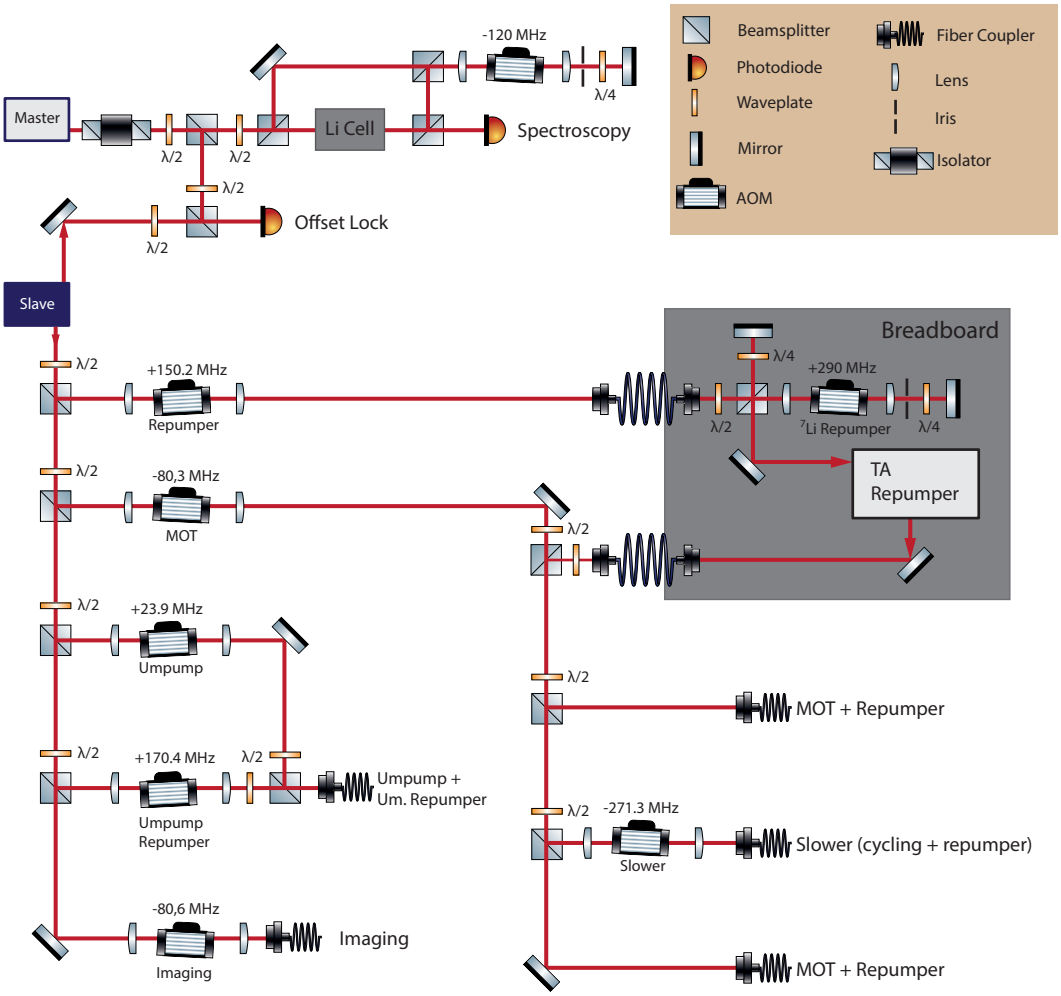

Figure 2.11: Optical setup for lithium. When working with ^{7}Li, the double pass AOM on the extra breadboard has to be included in the path, otherwise it can be bypassed by adjusting the half-waveplate before the beamsplitter. The master laser is locked to the required spectroscopic transition, depending whether ^{7}Li or ^{6}Li is used, in the Doppler-free saturation spectroscopy setup with a modulated pump beam [66].[1]

[1] ComponentLibrary by Alexander Franzen is licensed under a Creative Commons Attribution-NonCommercial 3.0 Unported License.

Changes for both beam paths

We also did some modifications on the optical table that affected both, Na and Li beam paths. Imaging path on the optical table was tangled among other's paths making it quite difficult to track down and optimize afterwards due to the reduced space. We took the imaging light into a fiber and moved the group of optical elements to a $50\times 35\,\mathrm{cm}$ breadboard. This makes clear that the optics involved in the imaging light is well separated, i.e. imaging AOM, lenses and shutter. Another change we made on the beam path was the modification of a periscope that lifts and a telescope that expands the slower beams. We went from having a telescope and a periscope afterwards to the opposite situation: a periscope and later, a telescope. We reduced the volume the 2 inches mirrors of the periscope were occupying and we simplified the path for both slower beams. Lastly, we changed the last lens that focuses the slower beam onto the oven exit. Lens is placed right next to the viewport were the slower beam enters the vacuum chamber. The focal length was chosen according to the distance to the oven exit. Position was adjusted while maximizing the Na MOT loading rate.

2.2.2 Zeeman Slower and MOT

An atomic beam of sodium and lithium atoms flying together out of the oven are decelerated with a spin-flip Zeeman slower and trapped in the MOT. A detailed description of the Zeeman-slower can be found in [69]. Our MOT consists of 6 beams, 2 of them are counter-propagating beams, 2 retro-reflected beams and a magnetic field gradient. An additional beam for the repumper light is included for sodium. Experimental sequence in this section has remained unchanged as it was described in [56]. A double MOT is created by trapping first lithium and then sodium. Lithium MOT lifetime is longer and its loading rate is slower compared to Na, therefore no problems are faced in this configuration. Usual MOT loading times are $4\,\mathrm{s}$ for sodium and $8\,\mathrm{s}$ for lithium. Na features a dark SPOT MOT that increases the MOT density by blocking the center area of the repumper beam [70]. For lithium, a compressed MOT phase increases its density shortly before the loading of the magnetic trap.

2.2.3 Spin Polarization

After cooling the atoms in the MOT, a magnetic trap is needed for cooling the atoms further down. To trap the atoms in the magnetic trap, magnetically trappable states are necessary. In the case of sodium, magnetic trapping has been performed in the lower ($|F=1,m_F=1\rangle$) and in the upper ($|F=2,m_F=2\rangle$) hyperfine state of the ground state [42]. Constraints appear when trying to trap sodium and lithium atoms together. From previous works [42, 56], the best approach to trap the mixture Na, ^{6}Li is to have Na in the stretched state $|2,2\rangle$ and ^{6}Li in the state $|3/2,3/2\rangle$, in the upper manifold as

well. For the mixture with bosonic lithium, the best way is to trap them both in the stretched state $|2, 2\rangle$.

The sodium MOT is mostly composed of atoms in the $F = 1$ manifold which are not suitable for our trapping purposes. Thus, a spin polarization scheme to prepare the atoms in the right state is fundamental. A spin polarization scheme consisting of two circularly polarized resonant beams, umpump and umpump repumper, together with a homogeneous offset magnetic field is applied right before the atoms are loaded into the magnetic trap. Both resonant beams optically pump the atoms until the final state $|2, 2\rangle$. The umpump beam is resonant to the MOT cycling transition, it polarizes the atoms in $F = 2$ to $|2, 2\rangle$. The umpump repumper beam is resonant to the repumper transition, hence it effectively pumps the atoms in $F = 1$ up to upper $F = 2$ manifold. As the probability for them to decay to the $F = 2$ ground state manifold is higher, they are then shifted by the former Umpump beam. The applied magnetic field is of at least $30\,\mathrm{G}$ to ensure the separation of the magnetic states.

The spin polarization procedure for fermionic lithium follows the same procedure, the *umpump* and *umpump repumper* beams optically pump the magnetic states until the $|3/2, 3/2\rangle$ state while the external magnetic field lifts their degeneracy. In comparison, the setup for bosonic lithium does not have an *umpump repumper* beam. In that case, at the end of the MOT phase atoms are exposed to repumper light only, resulting in a higher population of the $F = 2$ manifold. This is the starting point for the spin polarization, which is also done with the *umpump* beam for ^{6}Li. The energy offset between both isotopes is covered by the offset lock. Finally, the repumper beam is turned off letting the *umpump* to pump the $|F = 2, m_F\rangle$ substates until the required $|F = 2, m_F = 2\rangle$.

2.2.4 Magnetic Trap and Evaporative Cooling

Once we have the atoms in the suitable magnetically trappable states, they are transferred to the magnetic trap for further cooling. The cooling procedure differs from one species to another. Sodium is cooled down evaporatively by use of microwave (MW) radiation. While lithium, due to its favorable scattering with sodium [56], is cooled down sympathetically [71, 72].

The coils used to create the magnetic trap in our experiment are Cloverleaf Ioffe-Pritchard coils, described in detail in [64]. This configurations produces the same trapping potential produced by the Ioffe-Pritchard coils but without the bars of the original design [73]. This results in that the Cloverleaf Ioffe-Pritchard coils have a higher optical access. In our setup, the coils are embedded into two coil holders and are installed at about $1\,\mathrm{cm}$ from the glass cell, on both sides. The complete coils setup inside the coil holders is formed by; first, a group of eight coils in cloverleaf-shaped configuration, and second; three pairs of coils that by means of a series of insulated gate bipolar transistor (IGBT) can be connected in different configurations.

The cloverleaf array consists of 4 pairs of coils on each holder and it produces the radial confinement via its quadrupole field. We call them *gradient* coils and they are driven by their own power supply (Delta Elektronika SM15-400) up to $400\,\mathrm{A}$. Our magnetic trap confines the atoms in an approximately harmonic magnetic field minimum, but the center of the trap cannot be zero to avoid Majorana losses [74], therefore a small magnetic field offset has to be applied. This is achieved driving the other group of coils, the *Curvature* coils together with the *Antibias* coils, specifically. The antibias coils are in Helmholtz configuration resulting in a homogeneous field across the atoms. On the other hand, the Curvature coils have a smaller diameter but are separated by the same distance as the Antibias, resulting in a magnetic field with saddle point shape. When driving them both pairs, the total magnetic field produces an axial confinement with almost zero magnetic field offset at the center, which can be controlled at will with one power supply called bias. The third pair of coils is called *Finetune*, which are also in Helmholtz configuration but with less windings compared to the Antibias coils, resulting in a fast homogeneous field that is used in the spin polarization scheme explained in the previous section. For more details on the electronic circuit used to drive the Cloverleaf Ioffe-Pritchard trap of our experiment, see [56].

Although the spin-polarization scheme described in subsection 2.2.3 has been optimized, still a few atoms are present in unwanted magnetic substates. Atoms not in the stretched state $|2,2\rangle$ will highly likely collide heating the sample and therefore affecting negatively the final atom number. An extra step that can be seen as the final step of the spin polarization is done once the atoms have been already loaded into the magnetic trap. It consist on applying a MW frequency sweep onto the atoms that will drive the transition $|2,1\rangle \rightarrow |1,0\rangle$ thus removing them from the trap. We call this step the Spin Cleaning.

Evaporative cooling for sodium is performed by driving the transition $|2,2\rangle \rightarrow |1,1\rangle$ as that state is expelled from the trap. The MW transition is driven by applying a microwave sweep that decreases in frequency. It is divided into two sweeps, first one lasts $9\,\mathrm{s}$ with a frequency sweep range of $100\,\mathrm{MHz}$. The second sweep lasts $6\,\mathrm{s}$ and it sweeps a range of about $20\,\mathrm{MHz}$. One drawback of cooling down and therefore increasing the density of sodium atoms trapped in the state $|2,2\rangle$ is the atom loss due to its high three-body loss rate [75].

An important detail when cooling via microwave radiation is the antenna used for it. As described in [42], it gave better results to build and place an antenna on top of the glass cell than to use the ones already built in the coils holder, which are shown in [64]. Afterwards, we found out that the MW cooling was very sensitive to the antenna position when it was placed on top. One had to be careful not to clip the MOT beams with the antenna but also not to be far away from the atoms which will reduce the Rabi coupling. Our solution of placing the homebuilt antenna vertically between the glass cell and one of the coils holders has shown to be much more stable. The antenna is not

clipping any beam and also it is not susceptible to involuntary displacements that can affect its coupling to the driven transitions.

2.2.5 Crossed Dipole Trap

Our sequence is built to perform the experiments in a crossed dipole trap. The experiments will take place in the lower manifold of the ground state, i.e. $F = 1$ for bosonic species and $F = 1/2$ for fermionic lithium. From subsection 2.2.4, we know our atoms are magnetically trapped in the upper manifold and that if the density is too high, three-body collisions would induce atom losses. Our approach is to transfer them to the lower manifold at the beginning of the Dipole Trap sequence via a MW transfer, instead of using optical pumping as in subsection 2.2.3. Contrasted with magnetic traps, atoms in different magnetic substates can be trapped in the same dipole trap, allowing us to perform experiments where the spin state is considered a degree of freedom [14]. A description of the dipole force responsible for the trapping of the atoms using off-detuned laser beams can be seen section 3.1.

The experimental setup has not changed from what is described in [42], dipole trap source is an infra-red Nd:YAG laser with a wavelength of $\lambda = 1064\,\mathrm{nm}$ (DiNY cwQ 50) . The output beam is split into two beams following separated paths to finally cross at the atoms position forming the optical crossed dipole trap.

The horizontal beam, called waveguide, propagates following the axial direction of the magnetic trap with a relative angle of $8\,^{\circ}$, and it enters the glass cell through the aperture of the coils holder. It has a elliptically shaped beam waist, compressed vertically with cylindrical telescope. The horizontal beam waist is $60\,\mu\mathrm{m}$, whereas the vertical is $30\,\mu\mathrm{m}$. This modification, as explained in section 3.3, increases the vertical trapping frequency, reducing thus the differential gravitational sag that comes from the effective potential of the combined dipole trap and the gravitational acceleration. The power of the waveguide beam goes up to $8\,\mathrm{W}$, four times the power of the second beam which is of about $2\,\mathrm{W}$.

The second beam, called dimple, with a beam waist of $60\,\mu\mathrm{m}$ crosses the waveguide diagonally from bottom to top with an angle of $\sim 40^{\circ}$ with respect to the horizontal plane, as seen in Figure 3.1. To help the alignment of both dipole trap beams, the last mirror of each beam path is mounted on a piezoelectric mirror mount that can be controlled from the computer control, allowing us to fine adjust the position of the dipole trap beam.

The intensity of both dipole trap beams is actively stabilized. For each beam, a fraction of the total intensity, obtained by a pick-off plate, is measured using a quad-photodiode, giving us the information about the intensity and the position of the beam. The signal corresponding to the intensity is then fed in to a loop amplifier that controls the RF frequency input of an AOM implemented in the dipole trap beam path. The working frequency of the AOMs is $80\,\mathrm{MHz}$, diffracting the $+1$ order on one of the beams and

the -1 order on the second. This frequency shift between both beam modulates the trap on a timescale much higher than the trapping frequencies. The stable control of the dipole trap beams allows us to ramp up, maintain the intensity and perform evaporative cooling in a controlled way.

Before the dipole trap, atoms are evaporatively cooled down in the magnetic trap with a reduced axial magnetic confinement to avoid losses due to three-body collisions, therefore any transfer to the dipole trap has to be performed in a reduced confinement to not suddenly heat the atoms up and lose them from the trap. This process is done in several steps, we start by lowering the magnetic confinement in both directions in $500\,\mathrm{ms}$ in a stage we call expanded magnetic trap. Now that the atoms are distributed inside this new geometry, we ramp up the waveguide beam in $150\,\mathrm{ms}$ until its full power. This focused single beam features high radial trapping potential and low axial trapping potential, similarly to the last stage of the magnetic trap. The transfer finishes when the current flowing through the coils is ramped down to zero in $1500\,\mathrm{ms}$. The atoms can now expand along the waveguide as it can be seen in Figure 2.12, and as a result of the absence of magnetic trapping, their spin degree of freedom can be manipulated to prepare the states we want to work with.

We define a magnetic field axis perpendicular to the waveguide, with a magnitude of about $2\,\mathrm{G}$ using another group of coils called Offset Coils that will be described in chapter 4. This homogeneous magnetic field sets the quantization axis for the MW radiation that will drive the transitions from $|2,2\rangle$ to $|1,1\rangle$ in the case of bosonic species and from $|3/2,3/2\rangle$ to $|1/2,1/2\rangle$ for fermionic lithium. As soon as the atoms are transfered to the lower manifold, the dipole trap confinement can be increased without suffering from the aforementioned three-body collisions.

The crossed dipole trap is finally created when the dimple beam is ramped up during $100\,\mathrm{ms}$ to its full power of about $2\,\mathrm{W}$, confining the atoms to the volume enclosed by the two crossing beam, as shown in Figure 2.13. In order to reach the final temperatures, the confinement of the atoms in the crossed dipole trap is followed by a evaporatively cooling stage, consisting of linearly ramping down the intensity of both dipole trap beams. This is performed during $5\,\mathrm{s}$ until a final power below $1\,\mathrm{W}$ for the waveguide beam and of about $1.5\,\mathrm{W}$ for the dimple beam.

2.3 Final States Preparation

The experiments on spin-changing collisions (SCC) we are aiming to perform with the sodium-lithium mixture will use a superposition of two Zeeman levels in the lower manifold of each species. In the case of sodium and bosonic lithium, these states are $|1,1\rangle$ and $|1,0\rangle$. As we described in the previous section, at the end of the dipole trap sequence the bosonic atoms are in the $|1,1\rangle$ state. The particular initial condition we want to be able to prepare is: a 50:50 superposition of the sodium atoms between

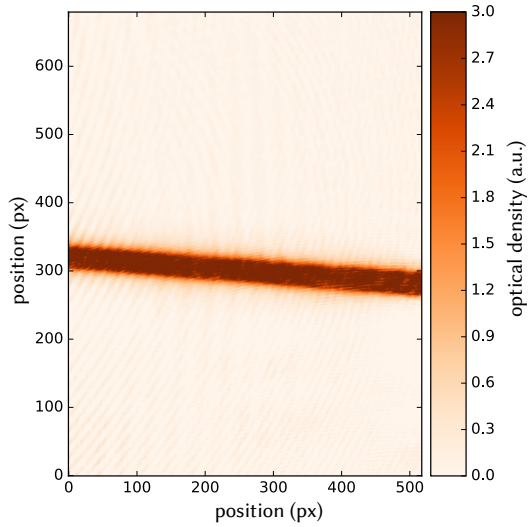

Figure 2.12: Sodium atoms in $|1,1\rangle$ loaded into the waveguide beam from the magnetic trap. The atoms expand along the waveguide due to its low axial confinement.

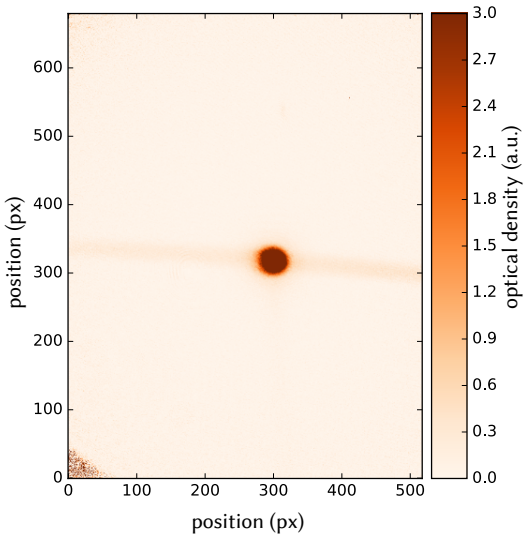

Figure 2.13: Crossed optical dipole trap loaded with sodium atoms in $|1,1\rangle$. The crossed dipole trap is created starting from the atoms loaded in the waveguide beam. Immediately after the atoms are loaded into the waveguide beam, the dimple beam is linearly ramped up during $200\,\mathrm{ms}$. The atoms are then kept within the attractive potential created by the two dipole trap beams.

$|1,0\rangle$ and $|1,1\rangle$ states, whereas all the bosonic lithium atoms in the $|1,1\rangle$ state. The SCC experiments have to take place in a homogeneous magnetic field of about $B_0 = 1.95\,\mathrm{G}$. At this magnetic field the energy difference between $|1,1\rangle$ and $|1,0\rangle$ for sodium, equals the energy difference between the states $|1,0\rangle$ and $|1,1\rangle$ for lithium. Allowing thus for coherent spin dynamics between both species.

To prepare the initial conditions for the states involved in the SCC experiment, we had two options. One approach is to drive the transition within the lower manifold, directly from $|1,1\rangle$ to $|1,0\rangle$ for bosonic atoms. The second approach is to perform a two-step preparation. For sodium it would consist on driving the transition $|1,1\rangle \longrightarrow |2,0\rangle$ first, followed by a MW pulse to drive the transition $|2,0\rangle \longrightarrow |1,0\rangle$. To perform the first type of preparation, one has to be careful with the energy splitting between the Zeeman levels of sodium and lithium. At low magnetic field they both have similar energy splittings between the Zeeman states and therefore, any attempt to independently control the state population of one atomic species would be coupled to transitions driven on the second atomic species.

Considering that in our experimental sequence, the bias magnetic field B_0 is applied and stabilized during the ODT stage. The best suited approach for us it therefore to prepare the final state by driving the sodium atoms through the state $|2,0\rangle$ before arriving to the state $|1,0\rangle$.

The experimental implementation to prepare the required state population is described in section 4.3.

2.4 Absorption Imaging

The images used to study the atoms are obtained by shining a beam of resonant laser light onto the atoms and recording its intensity profile $I_{\text{atoms}}(x,y)$ on a camera chip. As the imaging light is resonant to a certain transition of the atoms, the intensity profile on the camera chip will have a shadow casted by the atomic cloud that scattered the resonant photons. Due to the interaction with the imaging light, the atoms are excited away and lost from the imaging frame. Secondly, another image of the intensity profile is taken $I_{\text{beam}}(x,y)$ where no atoms are left. This second image will include any characteristics of the beam and the imaging path, i.e speckles created by dust particles on the optics, the beam profile. Finally, a third image $I_{\text{off}}(x,y)$ where imaging beam is switched off, is taken to account for any stray light that can be leaking onto the imaging camera as well as to characterize properties of the such as dark currents and faulty pixels. From these three images one obtains the two images used to determine the atomic cloud profile: $I_{\text{in}}(x,y) = I_{\text{atoms}}(x,y) - I_{\text{off}}(x,y)$ is the corrected incident imaging beam, whereas $I_{\text{out}}(x,y) = I_{\text{beam}}(x,y) - I_{\text{off}}(x,y)$ is the imaging beam after the interaction with the atomic cloud and corrected for the background light.

In general, the relationship between an incident $I_{\text{in}}(x,y)$ and an outgoing $I_{\text{out}}(x,y)$

beam is described using the known Beer-Lambert law considering the effect of the saturation [76]:

$$I_{\text{out}}(x,y) = I_{\text{in}}(x,y)\mathrm{e}^{-\sigma(\tilde{\delta},I_{\text{in}})\tilde{n}(x,y)}, \tag{2.1}$$

where the generalized cross section is defined as:

$$\sigma(\tilde{\delta}, I_{\text{in}}) = \alpha\frac{3\lambda^2}{2\pi}\frac{1}{1+4\tilde{\delta}^2/\Gamma^2}\frac{1}{1+s(\tilde{\delta})}, \tag{2.2}$$

λ is the imaging wavelength. The parameter α accounts for the multi-level structure of the driven transition during imaging. The factor $\tilde{\delta} = [1/(\omega_0 - \omega_\lambda) + 1/(\omega_0 + \omega_\lambda)]$ is the generalized detuning between the atomic transition ω_0 and the light frequency ω_λ. The parameter $s(\tilde{\delta})$ is the saturation parameter:

$$s(r,\tilde{\delta}) = \frac{I(r)/I_{\text{sat}}}{1+4\tilde{\delta}^2/\Gamma^2}. \tag{2.3}$$

From Equation 2.1, $\tilde{n}(x,y)$ is the atomic density integrated along the beam path, z-direction in this example:

$$\tilde{n}(x,y) = \int n(x,y,z)dz, \tag{2.4}$$

also called column density.

In the limit of low intensities $I \ll I_{sat}$, the generalized cross section (Equation 2.2) can be considered as a constant $\sigma \simeq \sigma_0$ as long as the imaging beam is resonant. Solving then, the Equation 2.1 for the column density, one obtains:

$$\tilde{n}(x,y) = -\sigma_0 \ln\frac{I_{\text{out}}(x,y)}{I_{\text{in}}(x,y)}, \tag{2.5}$$

which are the intensity profiles described and that we measure at the end of our experimental sequence.

2.4.1 Experimental Implementation

We updated the hardware of the imaging setup using the optical setup designed in [77]. It consists of a new $f = 33\,\mathrm{mm}$ objective lens mounted on the same unit (TOWER) together with secondary lenses for each species and their respective mirrors, as shown in Figure 2.14. The first mirror after objective lens is a dichroic mirror that reflects sodium imaging beam onto the sodium camera and let lithium imaging light pass through. The lower mirror is a regular mirror that reflects lithium imaging beam onto the lithium camera. The cameras are not attached to the TOWER but on translation

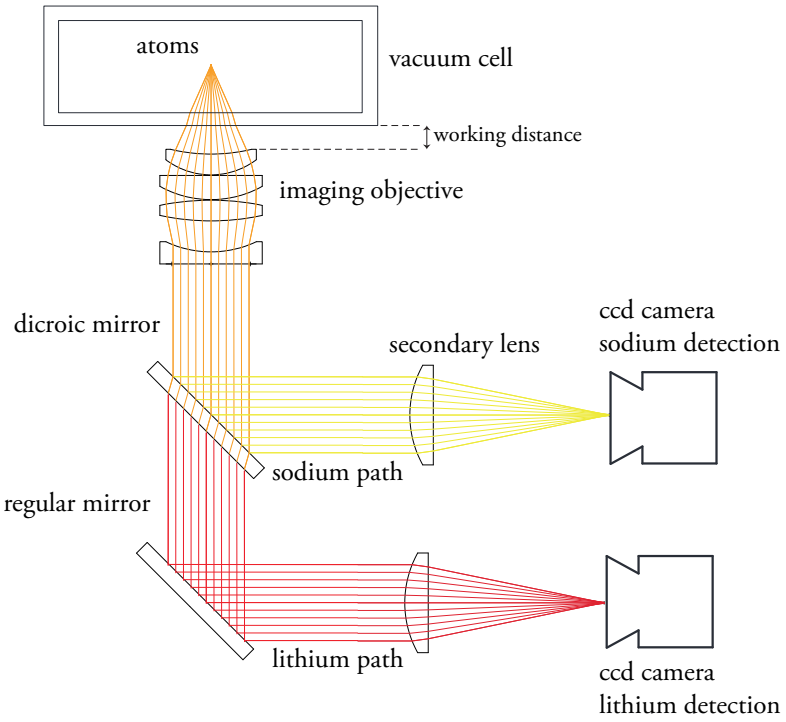

Figure 2.14: Schematics of the imaging setup used in the experiment after beam interacts with the atoms in the glass cell. Imaging light for sodium is reflected on the dichroic mirror and imaged on the upper camera. On the other hand, lithium imaging light passes through the dichroic mirror but it is reflected on the lower regular mirror to finally hit the lithium camera. Image taken from [77].

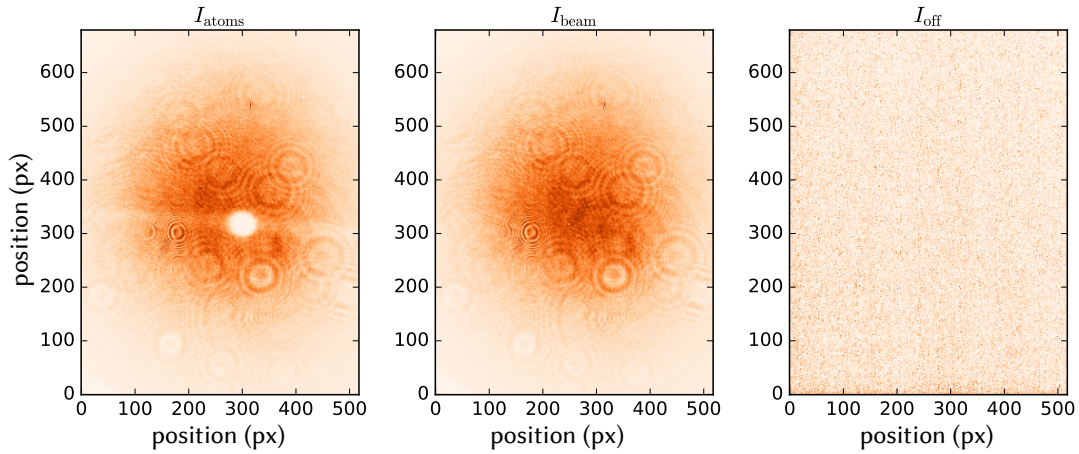

Figure 2.15: Images taken to produce an absorption image of Figure 2.13. **Left:** Atoms in the crossed ODT cast a shadow on the CCD camera via absorption of the imaging beam, atoms left in the waveguide can also be seen. **Center:** Image shows only the imaging beam after atoms are pushed away as a consequence of the first imaging pulse. It accounts for fringes and artifacts of the imaging path. **Right:** Image is taken without imaging beam. It accounts for stray light reaching the camera.

stages allowing for final adjustments. The secondary lens of the sodium path is a $f = 20\,\mathrm{mm}$ lens mounted on a cage system attached to the TOWER which aligns it with respect to the dichroic mirror, resulting in a magnification of $M = 6$. The secondary lens for lithium was also a $f = 20\,\mathrm{mm}$ lens mounted on a cage system, however, during the course of this thesis a new lithium camera was installed (Nüvü HNü 512 EMCCD camera) at a larger distance from the atoms compared to the original lithium camera, therefore the optical path needs further adjustments.

As it happens with the MOT beams, the imaging beam comes to the experimental table from the optical table in an single mode polarization maintaining fiber. The imaging beam travels through the atoms along the gravity axis, from top to bottom, resulting in images viewed from the bottom of the glass cell. This results in images with different time of flight still being in the center of the frame. Before hitting the atoms, imaging beam is reflected on a $1\,\mathrm{in}$ polarization beam splitter cube placed on top of the glass cell to reflect it downwards. This optical path is shared with the optical lattice beams detailed in chapter 3.

In the case of sodium, the transition driven during the imaging process is the $F = 2 \rightarrow F' = 3$ closed transition, therefore, in order to image the $F = 1$ atoms an additional imaging pulse of repumper light is needed, pumping the atoms from $F = 1$

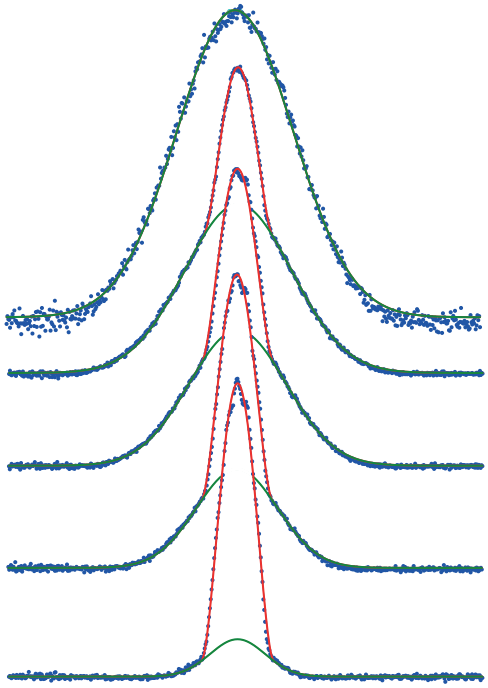

Figure 2.16: Exemplary atomic profiles of sodium atoms imaged with the absorption imaging technique. The sequence of profiles shows the transition from a thermal cloud to a Bose-Einstein Condensate from top to bottom. The green curve is a Gaussian fit of the thermal component of the cloud, whereas the red curve is the total fit, i.e. the sum of both thermal and condensate fits. The condensate fraction of the lower profile is $80\,\%$.

to $F = 2$. The pulse duration is $15\,\mu\mathrm{s}$ for both repumper and imaging pulse, however the latter has a delay of $5\,\mathrm{us}$ with respect to the repumper. The reference image $I_{\mathrm{beam}}(x, y)$, containing only the imaging beam, is taken $200\,\mathrm{ms}$ after the atoms were imaged, $I_{\mathrm{atom}}(x, y)$. The same applies to the background image $I_{\mathrm{off}}(x, y)$ where neither atoms nor imaging beam is present. Example for such images can be seen in Figure 2.15.

For lithium, the width of the three hyperfine states of the excited manifold of ^{6}Li is $4.4\,\mathrm{MHz}$, whereas for the four hyperfine excited states of ^{7}Li it is $18.3\,\mathrm{MHz}$. This causes the $6\,\mathrm{MHz}$ of linewidth of the lithium imaging beam to drive open transitions, such as $F = 3/2 \rightarrow F' = 3/2$ for ^{6}Li, decaying to the off resonant state $F = 1/2$. For that reason, repumper light is shone in at the same time the imaging beam is applied, to finally pump the atoms back into the resonant manifold.

2.5 Concluding Remarks

In this chapter we have presented the experimental setup employed to create ultracold gases of sodium and lithium. The complete experimental sequence is rather standard for ultracold atoms experiments.

The stability of the experiment was our main concern during the examination of each section of the experimental setup. We presented how the oven plays a key role in the overall performance of the experiment. We could obtain a reliable and high loading of the MOT by keeping the temperature of the oven at a constant value of $330\,^{o}\mathrm{C}$. Furthermore, by removing the cooling water of the collimation chamber of the oven the experiment could be used continuously for several months. The new sodium laser improved the stability of the experiment and it helped to dramatically reduce the adjusting time needed to run the previous dye laser.

We presented the changes in the vacuum setup. We exchanged the ion pumps for the oven chamber and for the pumping stage chamber. We installed new diagnostic elements, such as a Residual Gas Analyzer (RGA) and a new Bayard-Alper pressure gauge. This elements are useful during a bakeout of the vacuum chamber, which is performed usually after opening the chamber to refill the oven.

We presented the changes introduced in the optical setup of both species. We improved the stability of the $1.7\,\mathrm{GHz}$ AOM used in the repumper beam path for sodium by mounting it on a 5-axis translation stages. For lithium, we improved the available power for the repumper beam by installing a homebuilt Tapered Amplifier, improving thus the loading of the lithium atoms into the MOT.

3 Control over External degrees of Freedom

In recent years, optical dipole traps have shown to be a powerful tool to trap cooled atoms [14]. The fact that the internal states of the trapped atoms can be considered as a degree of freedom, will allow us to use this platform to study spin dynamics.

In general, when working with an ultracold mixture, the spatial overlap between the atomic clouds trapped in the same dipole trap is not automatically guaranteed, as the gravitational acceleration is a key factor causing a spatial mismatch. For a given trapping potential, clouds with different atomic masses have different effective trapping potentials and thus different centers of mass. A low spatial overlap would negatively influence the rate of the spin dynamics we are interested in [59]. It is possible to overcome this limitation by increasing the confinement of both species. This results in a reduction of the influence of the gravitational acceleration over the vertical mismatch of the center of mass of the atomic clouds.

This chapter starts describing the characteristics of optical dipole traps. Followed by a description of the crossed dipole trap used in this experiment. The modifications to improve the spatial overlap of the atomic clouds along the vertical direction of the crossed dipole trap are detailed.

Subsequently, the chapter describes the design and implementation of a versatile blue detuned optical lattice that confines both sodium and lithium atoms. This design allows for modifications of its components without much difficulties, emerging as a good first step towards future optical lattice implementations with higher complexity.

3.1 Optical Dipole Traps

Optical dipole traps are used in our experiment to perform the last stages of the trapping and cooling procedures bringing the atoms to degeneracy [subsection 2.2.5]. The working principle of optical dipole traps relies on the interaction between the light induced dipole $\vec{p}$ and the light of a far-detuned laser field $\vec{E}$ where it is immersed in. This interaction leads to a potential that relates both terms, given by time average:

$$U_{dip} = -\frac{1}{2}\langle \vec{p}\vec{E} \rangle, \tag{3.1}$$

where the electric dipole oscillates following the driving frequency ω of the laser field.

General expressions for the dipole potential U_{dip} and the photon scattering rate Γ_s are derived from a simplified picture but are still valid for the regime of our interest of large detuning [14]. Those expressions are read:

$$U_{\text{dip}}(r) = -\frac{3\pi c^2}{2\omega_0^3}\left(\frac{\Gamma}{\omega_0-\omega}+\frac{\Gamma}{\omega_0+\omega}\right)I(r), \tag{3.2}$$

and

$$\Gamma_{\text{sc}}(r) = -\frac{3\pi c^3}{2\hbar\omega_0^3}\left(\frac{\omega}{\omega_0}\right)^3\left(\frac{\Gamma}{\omega_0-\omega}+\frac{\Gamma}{\omega_0+\omega}\right)^2 I(r), \tag{3.3}$$

where ω_0 is the resonant transition frequency of the atom. Γ is the natural linewidth of the same transition, $2\pi \cdot 9.8\,\text{MHz}$ for sodium [65] and $2\pi \cdot 5.9\,\text{MHz}$ for lithium [78]. The intensity of the laser beam is related to the laser field as $I = 2\epsilon_0 c\,|E|^2$. Considering the detuning $\Delta = \omega - \omega_0$, for the case of $\Delta \ll \omega_0$, Equation 3.2 and Equation 3.3 can be simplified via the Rotating-Wave Approximation, in which the term $\omega_0 + \omega$ is neglected. The equations now read:

$$U_{\text{dip}}(r) = \frac{3\pi c^2}{2\omega_0^3}\left(\frac{\Gamma}{\Delta}\right)I(r), \tag{3.4}$$

and

$$\Gamma_{\text{sc}}(r) = -\frac{3\pi c^3}{2\hbar\omega_0^3}\left(\frac{\Gamma}{\Delta}\right)^2 I(r). \tag{3.5}$$

Both expressions scale linearly with the intensity $I(r)$ but the scattering of photons $\Gamma_{\text{sc}}(r)$ decays faster than the dipole potential $U_{\text{dip}}(r)$ with respect to the detuning Δ. It is thus preferable to build dipole trap potentials using far detuned laser light with high intensities for a certain trap depth, in order to maintain the scattering rate low. Furthermore, the sign of the detuning plays in important role on the nature of the potential. For a negative detuning, also named red detuning, i.e. when the driving frequency ω is smaller than the resonant transition frequency ω_0, the potential of Equation 3.4 is negative and the atoms experience a potential minimum in the regions where the intensity of the laser field has a maximums. On the other hand, when the detuning is positive ($\omega > \omega_0$, blue detuned), the atoms experience a potential minimum where the intensity of the laser field is minimum, resulting in optical traps where the light repels the atoms.

For red-detuned laser beams, the simplest trap geometry it to confine the atoms in a single focused Gaussian laser beam [79, 80]. The intensity distribution of a Gaussian beam propagating along z is given by:

$$I(r,z) = \frac{2P}{\pi w^2(z)} \exp\left(-2\frac{r^2}{w^2(z)}\right), \tag{3.6}$$

where P is the power of the beam and the radial coordinate r is perpendicular to the propagation direction. As it can be noted, the beam size w depends on z, this dependency is given by:

$$w(z) = w_0\sqrt{1+\left(\frac{z}{z_R}\right)^2} \tag{3.7}$$

where $z_R = \pi w_0^2/\lambda_{\text{ODT}}$ is the Rayleigh length and w_0 is the beam waist, the minimum beam size. λ_{ODT} is the wavelength of the dipole trap laser.

The trap is now fully described by Equation 3.2 and Equation 3.6. For low temperatures, the atoms will experience the center of the trap and therefore the trap can be approximated by a harmonic potential. The trapping frequencies are found to be:

$$\omega_r = \sqrt{\frac{4U_0}{mw_0^2}}, \tag{3.8}$$

for the radial direction, whereas for the propagating direction:

$$\omega_z = \sqrt{\frac{2U_0}{mz_R^2}}, \tag{3.9}$$

where $U_0 = U_{\text{dip}}(r=0, z=0)$ is the trap depth.

3.2 Crossed Optical Dipole Trap

The trapping geometry of the previously described single-beam optical dipole trap is not isotropic. This can be seen from Equation 3.8 and Equation 3.9, where the trapping frequencies along the radial and along the axial directions are different. For the particular case of our optical dipole trap beam, with a wavelength of $\lambda_{\text{ODT}} = 1064\,\text{nm}$ and a typical beam waist of $w_0 = 60\,\mu\text{m}$. The ratio between both trapping frequencies is $\omega_r/\omega_z \simeq 250$, reflecting the very elongated geometry of the single beam optical dipole trap. Single-beam optical dipole traps are very useful to perform experiments with a cigar shaped cloud, but that is not what we want to work with.

A more isotropic trap can be created by crossing two optical dipole trap beams at an angle of about 90° . The crossed-beam optical dipole trap employed in our experiment consists of two red detuned dipole trap beams, with a wavelength of $\lambda = 1064\,\text{nm}$, crossing at an angle of about 90° . The plane containing both beam does not lie on the horizontal plane, but it makes an angle of about 40° with it, as it can be seen in

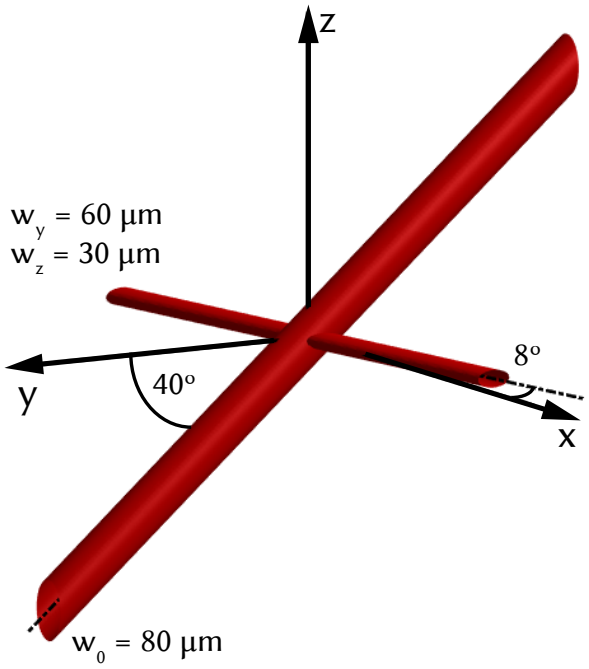

Figure 3.1: Spatial configuration of the laser beams used to create the crossed dipole trap. The waist of the waveguide was compressed along the vertical direction with a cylindrical telescope. The dimple beam crosses diagonally with an angle of 40° with respect to the horizontal plane from bottom to top. Adapted from [81].

Figure 3.1. This is due to the placement of the second beam (dimple) that crosses the waveguide beam diagonally from bottom to top. The horizontal beam (waveguide), which is aligned with the magnetic trap axis, has a higher power and therefore, it can create deeper trapping potentials. This is used when the atoms are transfered into the dipole trap from the magnetic trap. When the temperature of the trapped atoms is lower than the depth trap, the effective potential seen by the atoms can be well described by a 3D harmonic oscillator [14]:

$$V(x,y,z) = \frac{1}{2}m\left(\omega_x^2 x^2 + \omega_y^2 y^2 + \omega_z^2 z^2\right), \tag{3.10}$$

with ω_i the trapping frequency along the i-direction and m the mass of the trapped atom. For a given wavelength λ, the trapping potentials along the different directions depend on the characteristics of the laser beams, namely their powers and their waists, see Equation 3.8.

Due to the configuration of our dipole trap beams, the axes coordinates is referenced on the waveguide beam and on the vertical direction along gravity. The x-axis follows the waveguide beam axis, which makes an angle of 8° with the magnetic trap axis. The y-axis lies on the horizontal plane and it points along the direction of the atomic beam. Finally, the z-axis points upwards along the vertical direction.

3.2.1 Trapping Frequency Measurements

The measurements of the three different trapping frequencies were performed by means of two imaging cameras. Employing the Retiga camera, also used in the experiment for the normal absorption imaging, we are able to extract the information about the trapping frequency ω_y along the y-axis, as well as ω_x. An example of those two measurements can seen in Figure 3.2. By using another camera (Guppy F044B, Allied Visions) placed at the height of the glass cell and almost centered on the magnetic field axis created by the magnetic trap coils, we can extract information about the vertical trapping frequency ω_z, seen in Figure 3.4.

To experimentally measure the trapping frequencies of the optical dipole trap, the atoms are displaced from its center of mass by a fast perturbation that induces oscillations as the atoms probe the potential. In our experiment, the oscillations are induced by applying a magnetic field pulse that exerts a force onto the atoms. The atoms oscillate within the trap during a variable hold time t to be finally released from the optical dipole trap and freely expand. The oscillations are observed by time-of-flight measurements, that consist on imaging the atoms after a fixed flying time t_{TOF}. The initial displacement of the atoms has to be small enough to avoid probing non-harmonic part of the dipole potential or also to prevent falling off the dipole trap.

The experimental sequence to perform both trapping frequencies seen in Figure 3.2 was different. For the measurements **a)** and c), a slightly displacement of the atoms

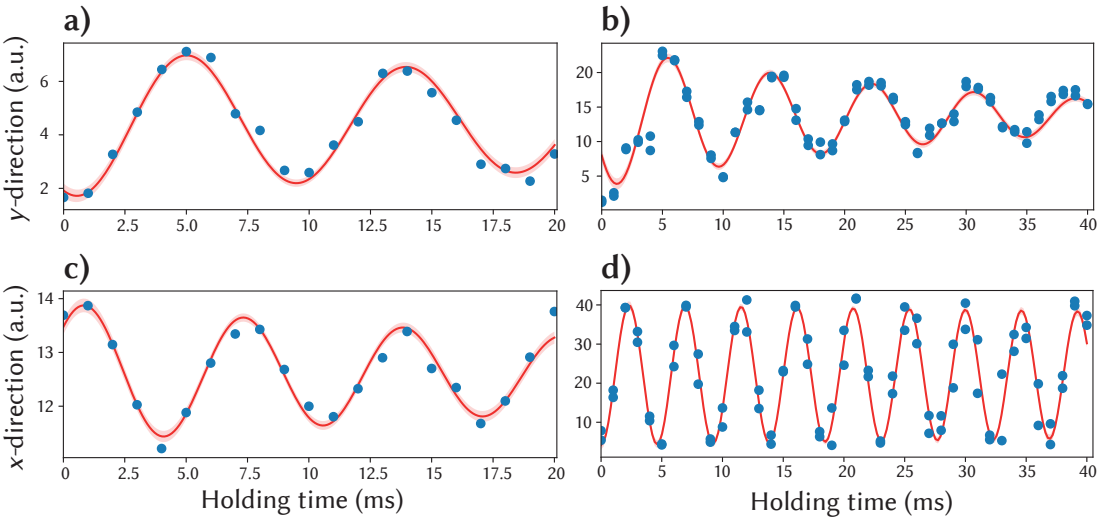

Figure 3.2: Two oscillation measurements of sodium atoms in the crossed dipole trap on the horizontal plane. Both images on the left hand side correspond to one experimental preparation, whereas the two images on the right hand side correspond to another experimental preparation. The preparation difference comes from the strength of the magnetic field pulse used to initially displace the atoms, which for the measurement on the right hand side, was stronger by a factor of about 2 compared to the one used for the measurement on the left hand side. This is expressed in the larger oscillation amplitude of images **b)** and **d)**, compared to images **a)** and **c)** respectively. Furthermore, a different frequency and a stronger damping is expected from a stronger pulse, due to the higher harmonics of the trap and the non-harmonic regions probed by the atoms. In our experiment, the magnetic field pulse is applied along the x-direction, therefore the effect of a stronger pulse is expected to be seen in **d)** compared to **c)**. The obtained trapping frequencies are: **a)** $\omega_y = 2\pi\times112(2)$ Hz. **b)** $\omega_y = 2\pi\times120(1)$ Hz. **c)** $\omega_x = 2\pi\times154(2)$ Hz. **d)** $\omega_x = 2\pi\times217(1)$ Hz. For all measurements, the atoms are kept for a variable holding time before they are released from the dipole trap and imaged. All the images are taken after a time of flight of $8\,\mathrm{ms}$. The power of the dipole trap beams is the same for both measurements.

was performed with a magnetic field pulse oriented mainly along the x-axis, inducing periodic oscillations with a larger amplitude along the same axis. Damping can be observed on both measurements. The trapping frequency obtained from the image **a)**, after fitting a sinusoidal function is: $\omega_y^{\text{left}} = 2\pi\times112(2)\,\text{Hz}$, whereas the trapping frequency along the perpendicular direction in **c)** is: $\omega_x^{\text{right}} = 2\pi\times154(2)\,\text{Hz}$.

For the second trapping frequency measurement, seen in the right hand side of Figure 3.2, a magnetic field pulse with a strength incremented by a factor of about 2, was employed. This magnetic field pulse is oriented mainly along the x-direction, therefore a stronger effect is expected in the oscillation amplitude along the same direction. If the atoms would probe a non-harmonic region of the trapping potential, that would be reflected in a different trapping frequency, as well as stronger damping in the oscillation amplitude. Similarly to the measurements performed with a weaker magnetic field pulse, the damping in the oscillation amplitude can be observed in both measurements, but they are more clear along the y-direction. The trapping frequency obtained from **b)**, which correspond to the y-direction, is: $\omega_y^{\text{left}} = 2\pi\times120(1)\,\text{Hz}$, which is a 7% increment with respect to the first measurement in **a)**. From the measurement in **d)**, along the y-direction, the trapping frequency is: $\omega_x^{\text{right}} = 2\pi\times217(1)\,\text{Hz}$, which is an increment of about 40% with respect to the first measurement in **c)**. To ensure the atoms were trapped in the same trapping geometry, the power of the dipole trap beams was the same for both measurements. To image the atoms, all measurements were taken after $8\,\text{ms}$ of time of flight.

3.2.2 Effective Beam Waist of the Waveguide Beam

Regarding the dimensions of the waveguide beam, the beam waist along the y-axis is $w_y = 60\,\mu\text{m}$. On the other hand, the vertical waist of the waveguide beam w_z has been modified with a cylindrical telescope. This modification changes the trapping frequency along the vertical direction compared to the horizontal direction for the same laser power. The telescope was implemented to correct for the differential gravitational sag, explained in section 3.3, that is present when working with ultracold atomic mixtures of different masses. The used telescope compresses the beam along the vertical direction, thus increasing the optical confinement along the same axis.

To characterize the crossed dipole trap along the gravity direction, several trapping frequency measurements were performed with different laser beam powers, which are shown in Figure 3.3. The relationship between the laser beam power and the trapping frequency for a given beam waist, can be obtained from Equation 3.8, but the optical dipole trap depth U_0 has to be generalized to non-equal beam waists. That is:

$$U_0 = \tilde{U}\frac{2P}{\pi w_z w_y} \tag{3.11}$$

where w_z is the compressed beam waist along the z-direction, whereas w_y is the beam waist along the y-direction, that it has no been modified. By combining Equation 3.8 with Equation 3.11 one obtains:

$$\omega_z = \sqrt{\frac{8\tilde{U}}{m\pi w_z^3 w_y}}\sqrt{P}, \tag{3.12}$$

where it is possible to see the square-root scaling of the trapping frequency with the respect to the dipole trap beam power P. For our experiment, the size of the unmodified beam waist is $w_y = 60\,\mu\mathrm{m}$ With Equation 3.11 and the known parameters it is possible to estimated the beam waist along the vertical direction. This is obtained by fitting a function of the form $f(P) = C_{\text{fit}}\sqrt{P}$ to the experimental data and comparing the prefactor C_{fit} of the fit to the prefactor of Equation 3.11.

For the measurement shown in Figure 3.3, the obtained value for the effective vertical beam waist is $w_z = 33.4(5)\,\mu\mathrm{m}$, which translates to an effective compression of the beam waist by a factor of about 1.8. The expected value for the compressed beam waist along the vertical direction is $w_z^{\text{expected}} = 20\,\mu\mathrm{m}$, due to the compression factor of 3 of the installed telescope. The difference between the measured and the expected value might be due to a slightly diverging beam coming from the telescope, resulting in a larger beam waist at the position of the atoms. Another cause of the difference between both values might come from the trapping geometry of the crossed dipole trap, due to the crossing angle of the dimple beam. Performing the trapping frequency measurement using only the waveguide beam is a good confirmation of the measurement presented here.

3.3 Gravitational Sag

The gravitational acceleration has an effect along the vertical direction of a dipole trap that has to be considered when describing the forces involved. This influence is seen as a shift on the trap minimum, given by:

$$\Delta_{\text{grav}} = \frac{g_{\text{ac}}}{\omega^2}, \tag{3.13}$$

where g_{ac} is the gravitational acceleration and ω is the trapping frequency along the same direction. From Equation 3.13, the only available knob to control the displacement of the effective trap center is the trapping frequency of the designed trap.

When trapping a mixture of more than one species, each species experiences a different gravitational sag due to the mass dependency of the trapping frequency. This spatial shift decreases the spatial overlap among the clouds, influencing the rate of the spin-changing collisions we will study. The influence of the gravitational sag onto the

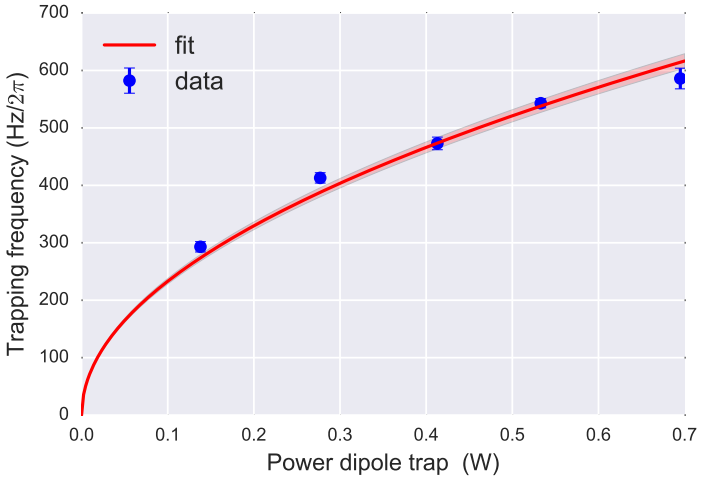

Figure 3.3: Trapping frequency measurements along the vertical direction for different dipole trap beam powers. The trapping frequency scales with the square root of the laser beam power according to Equation 3.12. From the prefactor C_{fit} of the fit of the form $f(P) = C_{\text{fit}}\sqrt{P}$, the effective beam waist can be obtained.

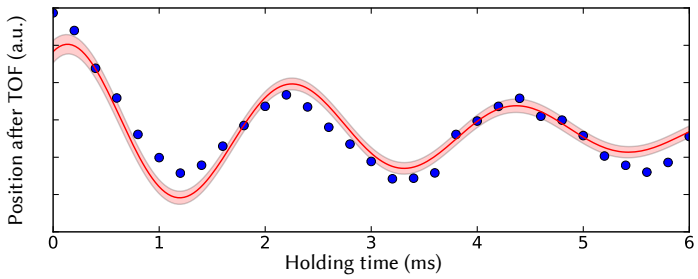

Figure 3.4: Oscillations of sodium atoms along the gravity direction in the crossed dipole trap for a trapping frequency of $\omega_z = 2\pi \times 473(11)$ Hz . Imaging was performed with another camera (Guppy F044B, Allied Visions) placed at the height of the glass cell, hence it can image the vertical displacement of the atoms.

cloud atoms can be reduced by increasing the trapping frequencies for each species. In the experiment, a larger trapping frequency along the vertical direction was obtained by a cylindrical telescope placed in the waveguide beam path, reducing the beam waist from $w_z^{\text{before}} = 60\,\mu\text{m}\; w_z =$ to $w_z^{\text{after}} = 33.4(5)\,\mu\text{m}$. Considering the measured trapping frequency of $\omega_y^{\text{wg}} = 2\pi\times 120(1)\,\text{Hz}$ for sodium along the horizontal direction of the waveguide beam, where the waist has not been modified. The vertical trapping for sodium atoms in the same dipole trap is about $\omega_z^{\text{wg}} = 2\pi\times 215\,\text{Hz}$.

The spatial separation between the clouds of sodium and lithium can be directly calculated for a fixed trapping frequency. For the original trapping frequencies, before the implementation of the telescope, the calculated vertical separation between the clouds of sodium and lithium is $13.8\,\mu\text{m}$, which is comparable to the typical size of the trapped atomic clouds. After the reduction of the beam waist by a factor of 1.8, the differential gravitational sag is reduced to $1.36\,\mu\text{m}$. Even thought the reduction of the beam waist is nearly by a factor of 2, the reduction of the differential gravitational sag is by one order of magnitude, explained by the w_0^4 scaling of the gravitational sag with respect to the beam waist.

3.4 Condensation of Trapped Atoms

When describing the properties of trapped gases, several considerations have to be taken into account, being the trapping potential, the temperature and the inter-atomic interaction among them. This section aims to give a qualitatively description following the work presented in [28], focusing on harmonic the trapping potential used in this experiment, given by Equation 3.10.

For bosonic atoms, the distribution of the occupation number of single-states is given by:

$$f^0(\epsilon_\nu) = \frac{1}{e^{(\epsilon_\nu-\mu)/k_BT-1}}, \tag{3.14}$$

where ϵ_ν is the energy of the single-particle state and the chemical potential μ is a parameter introduced from the condition of conservation of particles. At high temperatures and low densities, the atoms can be described as free particles confined by the external potential $V(r)$. In this regime, the separation of the energy levels becomes negligible and the Boltzmann distribution is a good representation of the distribution function of the atomic states:

$$f^0(\epsilon_\nu) \simeq e^{-(\epsilon_\nu-\mu)/k_BT}. \tag{3.15}$$

At a critical temperature T_c, Bose-Einstein condensation occurs as the occupation number of the single-particle ground state can increase macroscopically. For our trapping potential the critical temperature is given by:

$$T_{\mathrm{c}} \approx 0.94\hbar\bar{\omega}\frac{N^{1/3}}{k_B}, \tag{3.16}$$

where $\bar{\omega} = \sqrt[3]{\omega_x\omega_y\omega_z}$ is the geometric mean of the three trapping frequencies of the harmonic oscillator trap. N is the total atom number. A useful expression for experiments, Equation 3.16 can be written in the form:

$$T_c \approx 4.5\left(\frac{\bar{f}}{100\mathrm{Hz}}\right)N^{1/3}\ \mathrm{nK} \tag{3.17}$$

where $\bar{f} = \bar{\omega}/2\pi$. For typical experimental values of $N \sim 3\times10^5$ atoms and a geometric mean of $\bar{f}$ =200 Hz, it translates to a critical temperature of about $T_c = 600\,\mathrm{nK}$.

Below the critical temperature T_c, a fraction of the atoms is macroscopically populating the ground state whereas the rest is populating the excited states. The number of particles in the condensate is given by:

$$N_0 = N\left[1-\left(\frac{T}{T_c}\right)^3\right], \tag{3.18}$$

where the condensate fraction is defined as $\eta = N_0/N$.

From Equation 3.18 and Equation 3.16, a relation between condensed fraction and critical temperature makes possible to estimate the absolute temperature T of the cloud for intermediate temperatures. The condensed fraction can be experimentally accessed with time of flight measurements of the atomic profile, as shown in Figure 3.5.

Experimentally, what can be accessed via absorption imaging is the density profile of the atoms. For the case of non-condensed atoms, the density is well represented by the Boltzmann distribution:

$$n(r) = \frac{N}{\pi^{3/2}R_xR_yR_z}e^{-\frac{x^2}{R_x^2}}e^{-\frac{y^2}{R_y^2}}e^{-\frac{z^2}{R_z^2}}, \tag{3.19}$$

as it is confirmed in the fit curve of a) in Figure 3.5.

3.4.1 Interacting Bosons

When considering the interaction between the atoms, an important length scale is the inter-particle distance. In a dilute gas, the separation of the atoms is on the order of $10^2\,\mathrm{nm}$, which is much larger than the typical two-body scattering length. For example in the case of sodium atoms, the scattering length is $a_{\mathrm{Na}} = 55a_0$, with a_0 the Bohr's radius. Corresponding to a length scale of $\sim 3\,\mathrm{nm}$. Therefore, the atom-atom

interaction is the leading contribution to the interaction term, over three-body and higher orders interactions.

At low temperatures, the interaction between indistinguishable bosonic atoms in the same internal state is dominated by s-wave scattering. This is captured in the effective contact interaction:

$$g = \frac{4\pi\hbar^2 a}{m}, \tag{3.20}$$

where a is the s-wave scattering length. In the case of fermionic particles, the effective interaction vanishes due to symmetry considerations on the scattering cross section.

3.4.2 Gross-Pitaevskii Equation

Including the interactions between the atoms, the Gross-Pitaevskii equation describes the properties of a dilute gas at zero-temperature.

$$\frac{-\hbar^2}{2m}\nabla^2\psi(r) + V(r)\psi(r) + g|\psi(r)|^2\psi(r) = \mu\psi(r) \tag{3.21}$$

where the nonlinear term accounts for the mean field produced by the other bosons. The total potential acting onto the atoms is then the sum of the external potential $V(r)$ and the mean field $g|\psi(r)|^2$. The density of the atoms is given by

$$n(r) = |\psi(r)|^2 \tag{3.22}$$

For atoms with repulsive interactions ($a > 0$), the solution of the Equation 3.21 for the atomic density within the Thomas-Fermi approximation is:

$$n(r) = |\psi(r)|^2 = \frac{[\mu - V(r)]}{g}, \qquad \mu > V(r), \tag{3.23}$$

and zero for $\mu < V(r)$. The Thomas-Fermi approximation is a valid description of the ground state wavefunction of the atomic sample, and it is obtained by neglecting the contribution of the kinetic energy term in the Gross-Pitaevskii equation for large atom numbers.

Writing explicitly the shape of the harmonic potential (Equation 3.10), the obtained solution for the density in Equation 3.23 can be arranged as:

$$n(r) = n(0)\left[1 - \left(\frac{x^2}{R_x^2} + \frac{y^2}{R_y^2} + \frac{z^2}{R_z^2}\right)\right], \tag{3.24}$$

where

$$R_\alpha^2 = \frac{2\mu}{m\omega_\alpha^2}, \tag{3.25}$$

is the extent of the cloud along the α direction, and $n(0) = \mu/g$ is the peak density. It is important to point out the inverted parabolic shape of the density distribution for the atoms in the ground state.

The total atom number, obtained from $N = \int dr|\psi(r)|^2$, is related the chemical potential and the trapping frequency by:

$$N = \frac{8\pi}{15}\left(\frac{2\mu}{m\bar{\omega}^2}\right)^{3/2}\frac{\mu}{g}. \tag{3.26}$$

3.4.3 Density profiles and Temperature

When the sodium atoms are transfered into the the crossed dipole trap, their temperature is not sufficiently low to observe condensation. For typical experimental parameters of the trap, the value of the critical temperature is on the order of $0.6\,\mu\mathrm{K}$. To achieve condensation, trapped atoms are cooled by evaporative cooling which consists on linearly reducing the power of the dipole trap beams. For the images in Figure 3.5, the only beam power that was reduced was the power of the waveguide beam. To be able to image the differentiate the thermal density profile from the condensed part, the atoms are released from the dipole trap and imaged after a time of flight of $8\,\mathrm{ms}$.

In Figure 3.5, the optical density profile of the atoms is obtained by integrating the two-dimensional optical density of the imaged atoms along one axis . It is possible to observe the Boltzmann distribution of the thermal density profile, fitted using Equation 3.19. This was used in the four shown images, including where the BEC is present. For the BEC profile, Equation 3.24 is used.

From the images in Figure 3.5, the mean trapping frequency of the dipole trap varies from $\bar{f} \simeq 320\,\mathrm{Hz}$ for the image in **a)** until $\bar{f} \simeq 200\,\mathrm{Hz}$ for a condensate fraction of $\eta = 0.76$ in **d)**. While during free expansion, the width of the thermal profile increases according to the temperature of the sample. This allows to find another expression to estimate the temperature of the expanding cloud, from the width σ of the thermal profile, after a time of flight $t_{\mathrm{TOF}} \gg 1/\omega_{x,y,z}$:

$$\sigma_{x,y,z} = \sqrt{\frac{2k_BT}{m}}t_{\mathrm{TOF}}. \tag{3.27}$$

A temperature of $T = 428\,\mathrm{nK}$ is estimated using Equation 3.27 on Figure 3.5 **c)**. In comparison, using the obtained condensate fraction η and Equation 3.18, a temperature of $T = 750\,\mathrm{nK}$ is estimated.

To have better quantitative results, several adjustments and calibrations have to be performed yet. For example, to estimate the critical temperature of the cloud, a good calibration of the atom number is needed, as well as a better estimation of the trapping frequencies of the dipole trap. However, it is possible to qualitatively understand the behavior of the trapped gas.

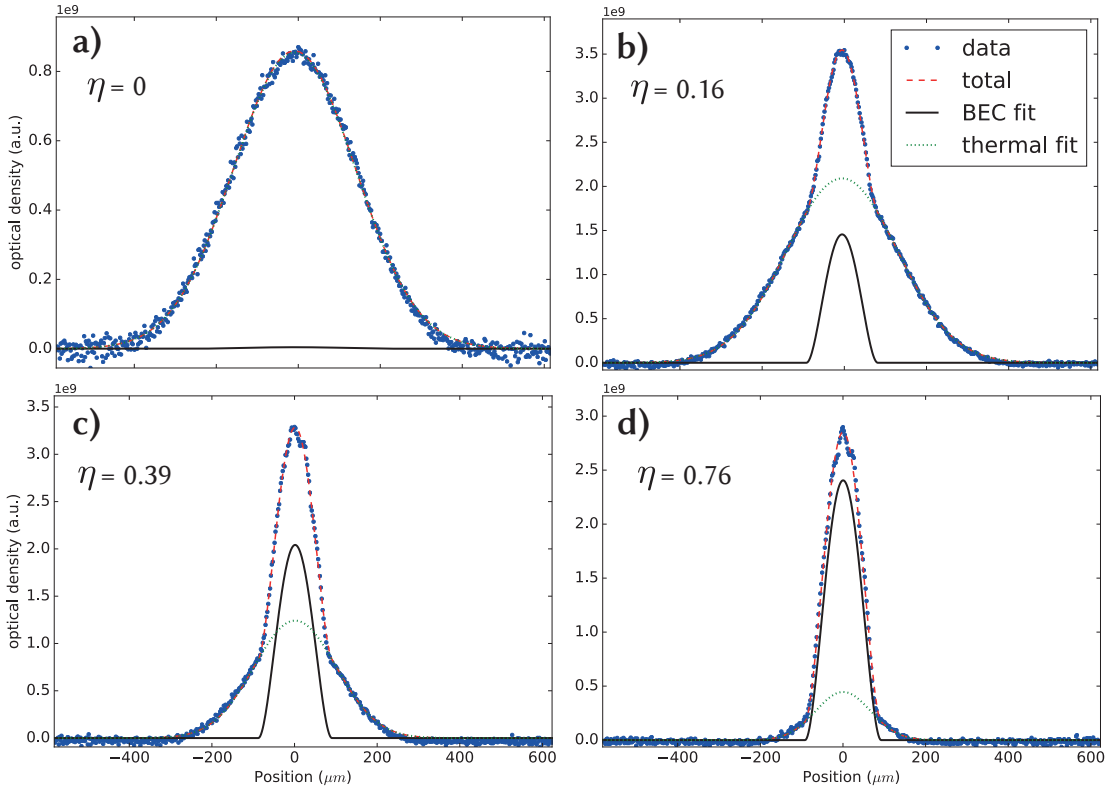

Figure 3.5: A qualitative behavior of the condensate fraction of sodium atoms in the crossed dipole trap. The different condensate fractions are achieved by evaporative cooling in the dipole trap. Images were taken with $8\,\mathrm{ms}$ of time of flight. The *total* curve is the sum of the fits of both thermal and BEC profiles. **a)** The thermal cloud is well described by the Boltzmann distribution of Equation 3.19. **b)** Once the temperature of the atoms is below the critical temperature T_c, a bimodal profile is seen indicating the condensation of a fraction of the atoms. **c)** Reducing the temperature further down increases the condensate fraction. The BEC profile is well described by the Gross-Pitaevskii equation in the Thomas-Fermi approximation of Equation 3.24. **d)** Furthermore, the width of the thermal cloud is reduced as the temperature is reduced.

3.5 Optical Lattice

From Equation 3.2 we can see that at a certain optical detuning, the potential shape is given by the spatial dependency of the laser intensity $I(r)$. In both configurations mentioned in section 3.2, the spatial dependency of the beam is set via focusing the dipole beams, resulting in useful and simple traps. In comparison, an optical lattice involves the interference of two laser beams resulting in a standing wave with a periodic modulation of the laser intensity, and thus of the optical dipole potential.

The simplest optical lattice is the one-dimensional lattice and the simplest way to built it is to use a retro-reflected beam. The drawback of such a setup is that the lattice spacing is fixed and it is given by half the wavelength of the used laser beam. Therefore, to change the lattice spacing a different laser wavelength is needed. On the other hand, to build a one-dimensional lattice with a specific lattice spacing different than half the wavelength of the laser beam, the laser beams have to be crossed at a different angle instead of retro-reflecting them.

In a general description, the dipole potential for a one-dimensional lattice with laser beams traveling with wave-vectors $\vec{k}_1$ and $\vec{k}_2$, is given by:

$$V_{lat}(\vec{r}) = V_0 \sin^2 \left[\frac{\left(\vec{k}_1 - \vec{k}_2\right) \cdot \vec{r}}{2} \right]. \tag{3.28}$$

where V_0 is the trap depth. By solving the product $\left(\vec{k}_1 - \vec{k}_2\right) \cdot \vec{r}$ with equal wavevector magnitude $|\vec{k}_1| = |\vec{k}_2|$, meaning both beams have the same wavelength, one obtains for the lattice spacing:

$$\Delta y = a_{lat} = \frac{\lambda}{2\sin(\alpha)}, \tag{3.29}$$

according to the scheme of Figure 3.6. From Equation 3.29 one can see that the lattice spacing is directly proportional to the wavelength of the laser beam and to the crossing angle of the beams. The smallest lattice spacing is obtained for $\alpha = \pi/2$, where the simplest setup of two counter-propagating beams is recovered.

Following the same analysis done with the crossed dipole trap, the trapping frequency of the confined atoms is given by:

$$\omega_x^{\text{latt}} = \sqrt{\frac{8U_0\pi^2}{m\, a_{\text{latt}}}} \tag{3.30}$$

where U_0 is the trap depth, often given in terms of the recoil energy

$$E_R = \frac{\hbar^2 k^2}{2m}. \tag{3.31}$$

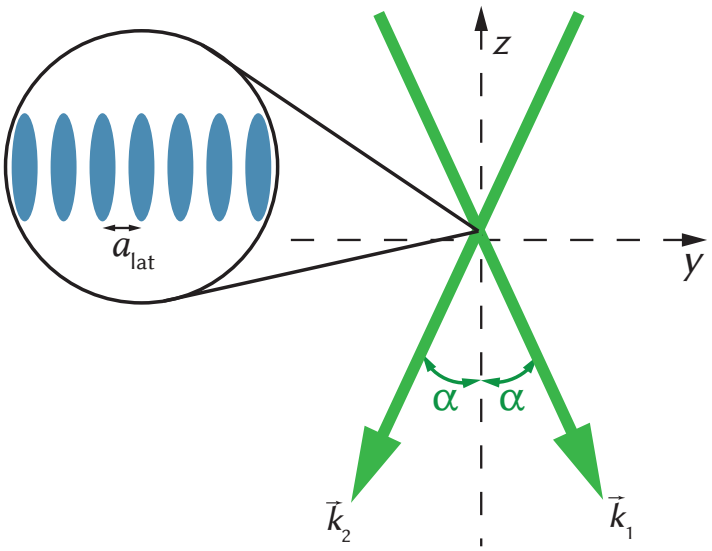

Figure 3.6: Geometric scheme of a one-dimensional lattice with two crossing beams. The lattice spacing a_{lat} depends on the laser wavelength and on the crossing angle α according to Equation 3.29.

3.5.1 Experimental Implementation

We implemented a new one-dimensional optical lattice that increases the confinement of the atoms in the optical dipole trap by employing a $532\,\mathrm{nm}$ laser beam (Verdi V10, Coherent), thus creating a blue detuned periodic potential for both sodium and lithium.

Our design starts with two parallel beams separated by a distance d and passing through a lens of focal distance f before reaching the atoms. As a result, the two beams cross at the focal point of the lens and produce the one-dimensional lattice as depicted in Figure 3.7. To create the parallel beams we built a beam splitter that consists on a $50{:}50$ non-polarizing beamsplitter cube and a mirror, both components are mounted on one plate. The cube is glued onto the surface of the plate while the mirror is on a mirror mount with two adjustable screws. Another possible setup would be to replace the mirror for a right angle prism mirror and build a fixed splitter by gluing the prism next to the cube. We continued working with the design that features the mirror due to its adjustable nature.

We installed a new optical table on top of the experimental table, allowing for the lattice beams to vertically enter the glass cell from above. The laser beam is brought to this table with an optical fiber and all the optics needed to create the two parallel beams is placed on this table, as well. As the imaging setup is built in such a way that the imaging beam also enters the glass cell vertically from above, a polarizing beam splitter was installed to join the optical lattice beams path with the imaging beam path

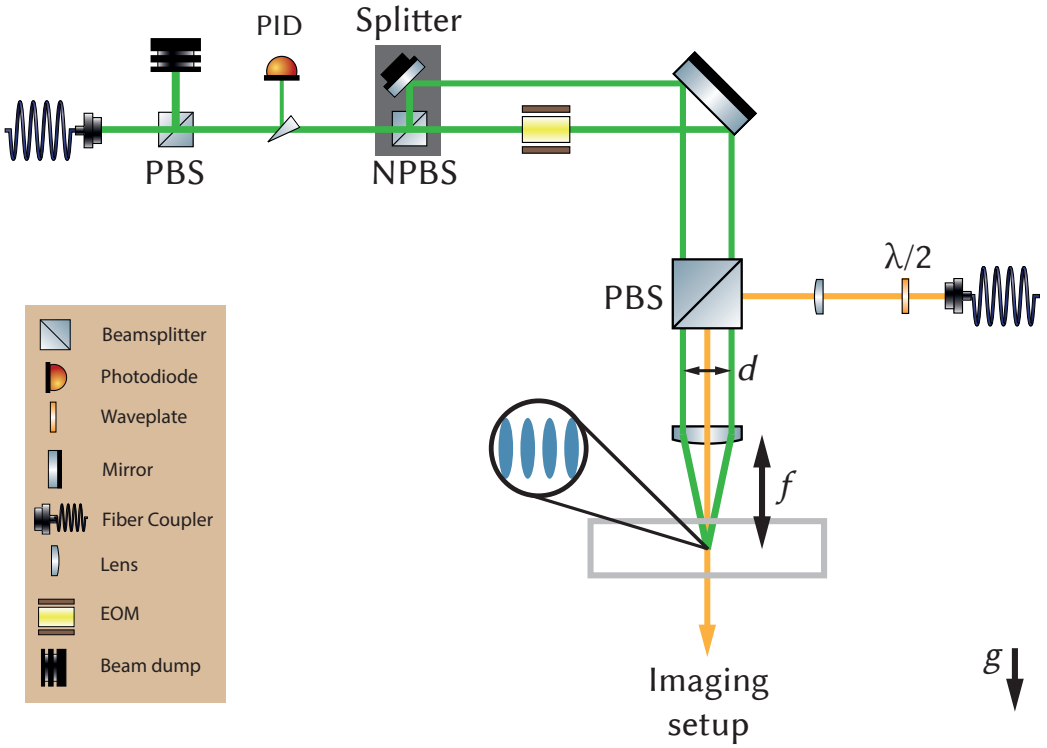

Figure 3.7: Experimental implementation one-dimensional optical lattice. The crossing angle of the beams depends on the separation of the beam d and on the focal distance f of the focusing lens. After the last polarizing beamsplitter, the optical path is shared with the imaging beam. We placed specific filters on front of the cameras to avoid saturation due to the lattice beams. [1]

and keeping the imaging path in place, as shown in Figure 3.7. To avoid saturation of the imaging cameras, filters are placed on front of them. For the D2 line of sodium at $589\,\mathrm{nm}$, a bandpass filter (Semrock Brightline HC $590/20$) centered at $590\,\mathrm{nm}$ with a FWHM of $20\,\mathrm{nm}$ is installed. For the D2 line of lithium at $671\,\mathrm{nm}$, a longpass filter (Edmund Optics RG-665) with a cut-off position at $\lambda_c = 665(6)\,\mathrm{nm}$ is installed.

The lattice beams are intensity stabilized following the same method used for the ODT beams. The output beam from the laser source passes through an $80\,\mathrm{MHz}$ AOM which changes the intensity of the first diffracted order via adjusting the RF power. A pick-off plate placed before the beam splitter on the new optical table obtains a signal proportional to the total intensity, which is then used in the servo that controls the power of the AOM RF signal.

[1] ComponentLibrary by Alexander Franzen is licensed under a Creative Commons Attribution-NonCommercial 3.0 Unported License.

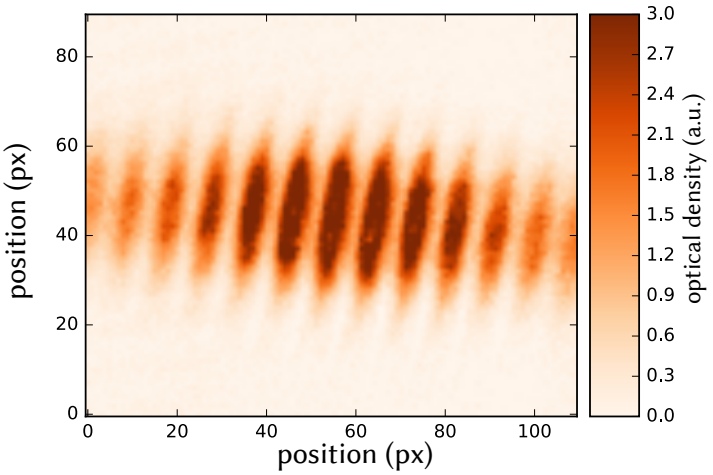

Figure 3.8: In-situ image of a one-dimensional lattice confining sodium atoms in $|1,1\rangle$. After atoms are trapped in the crossed ODT, lattice is ramped up during $400\,\mathrm{ms}$ to a final power of $10\,\mathrm{mW}$. The power calibration in terms of control voltage is $25\,\mathrm{mW/V}$

3.5.2 Lattice Characteristics

The geometry of the lattice is shown in Figure 3.6, where two laser beams cross at a certain angle α and produce the lattice. The crossing angle of the beams, and therefore the lattice spacing, is obtained from trigonometry rules using the separation d and the focal length f of the focusing lens, that is:

$$a_{lat} = \frac{\lambda f}{d}, \quad f \gg d. \tag{3.32}$$

For a lattice created using a $f = 200\,\mathrm{mm}$ focusing lens, and a separation of the beams of $d = 10\,\mathrm{mm}$, a spacing of $a_{\mathrm{lat}}^{\mathrm{calc}} = 10.6\,\mu\mathrm{m}$ is obtained from Equation 3.32. To compare this calculated value with the experimental realization, a sine function fit over several images of the lattice, as the one seen in Figure 3.8, resulted in a lattice spacing of $a_{\mathrm{lat}}^{\mathrm{fit}} = 10.57(13)\,\mu\mathrm{m}$, in agreement with the reference value.

The periodic potential is created after the atoms have been cooled down in the crossed dipole trap. The lattice beams are simultaneously ramped up and superimposed with the dipole trap. The periodic potential slices the atomic cloud in several pancake-like clouds along the waveguide direction, increasing thus the trapping frequency along that direction. The confinement of the dipole trap is still present along the other two directions.

For the optical lattice in Figure 3.8 where sodium atoms in the $|1,1\rangle$ state are confined, both lattice beams are focused down to a waist of about $170\,\mu\mathrm{m}$ and each lattice beam has

a power of about $10\,\mathrm{mW}$. The trap depth in this configuration is $U_0 \simeq h\times 1.5\,\mathrm{kHz}$, or $U_0 \simeq 75\,\mathrm{E_R}$ as well, where the recoil energy for sodium in this lattice is $E_R = h\times 20\,\mathrm{Hz}$. The blue detuned light of the optical lattice confines the atoms at the intensity minima of the periodic potential. The maximum trapping frequency is about $\omega_x^{\mathrm{latt}} = 2\pi\times 1\,\mathrm{kHz}$.

3.6 Concluding Remarks

In this chapter we presented the techniques used to confine the atoms in real space and control that confinement according to our needs. In this regards, the optical dipole potential was a crucial ingredient along the techniques presented in this chapter.

We described the crossed optical dipole trap used to confine the atoms after they have been cooled in the magnetic trap. We increased the vertical confinement of the trap by reducing the waist of the waveguide beam by a factor of almost 2. This modification helps us to reduce by one order of magnitude the differential gravitational sag between the sodium and the lithium cloud.

To further control the spatial distribution of the trapped atoms, we presented the design and implementation of a one-dimensional lattice. The lattice slices the atoms along the waveguide beam using blue detuned light at $532\,\mathrm{nm}$. The lattice spacing is of about $10\,\mu\mathrm{m}$.

The optical lattice setup can be tuned according to our needs by modifying several components. For instance, a different lattice spacing can be obtained by replacing the current $f = 200\,\mathrm{mm}$ focusing lens . The available laser power of the laser source used for the lattice, allows for further increments of the lattice confinement, increasing thus the trap depth and the trapping frequency.

4 Control over Internal Degrees of Freedom

This chapter describes the implementation of an active stabilization setup designed to control the magnetic field dependent spin-changing collisions between sodium and lithium ultracold atoms. This bottom-up approach starts with the study of the dynamics between sodium and bosonic ^{7}Li, because stability requirements are more accessible compared to the ones needed for the Na^{6}Li mixture [56].

As in many stabilization implementations, we make use of a closed feedback loop to control the magnetic field created by a dedicated group of coils, detailed in this chapter. A voltage signal proportional to the magnetic field is obtained from a fluxgate sensor placed close to the glass cell, where the atoms are trapped. Signal is then fed in to a PID board which controls the power supply driving the magnetic field coils.

To calibrate the applied magnetic field we perform spectroscopy measurements on a magnetic dependent transition of sodium. We present the modifications implemented in the MW setup that allow us to perform such measurement. In addition, we present the control over the population of two Zeeman states of the ground state of sodium via a 2 MW pulse procedure.

4.1 Oscillations at a Critical Magnetic Field

From the studies performed in [56], we focused the experimental work towards the realization of spin-changing collisions for the ^{23}Na ^{7}Li mixture, employing the $|1,0\rangle$ and $|1,1\rangle$ states. In this context, to obtain an intuitive picture, it is helpful to look at the two-body description of the dynamics. Starting from the Hamiltonian describing the molecular interaction between two spin-1 particles with states of the form $|f,m\rangle$, a generalized Rabi frequency expression can be found [55], that couples the two atomic states:

$$\Omega = \sqrt{(E_1(B) - E_2(B))^2 + (g_2 - g_1)^2}/\hbar \tag{4.1}$$

where $g_F = 4\pi\hbar^2 a_F/\mu$ is the two-body interaction term for the molecular channel with total spin $F = f_1 + f_2$, reduced mass μ, and scattering length a_F. $E_1(B)$ is the Zeeman energy of the configuration Na = $|1,1\rangle$, ^{7}Li = $|1,0\rangle$, and vice-versa for $E_2(B)$. This model predicts larger oscillations for a vanishing differential energy

$\Delta E(B) = E_1(B) - E_2(B) = 0$. Although, this model does not include the many-body effects that are present in the rigorous mean-field description of the spin-spin interaction, the intuitive picture of resonant oscillations at a critical magnetic field B_0 still holds [55, 56].

Using the Breit-Rabi formula [82], for a magnetic field B:

$$E_{|J=1/2\ m_J\ I\ M_I\rangle} = -\frac{\Delta E_{\text{hfs}}}{2(2I+1)} + g_I\,\mu_B\,m\,B \pm \frac{\Delta E_{\text{hfs}}}{2}\left(1 + \frac{4mx}{2I+1} + x^2\right)^{1/2} \tag{4.2}$$

where ΔE_{hfs} is the hyperfine splitting, $m = m_I \pm m_J$, I is the nuclear spin, J is the total angular momentum, g_i is the Landé g-factor for the quantum number i, and

$$x = \frac{(g_J - g_I)\mu_B B}{\Delta E_{\text{hfs}}} \tag{4.3}$$

which applies for the ground state of both Li and Na [65], one can calculate the critical field B_0 at which the energy difference for investigated process $\text{Na}|1,0\rangle{}^7\text{Li}|1,1\rangle \leftrightarrow \text{Na}|1,1\rangle{}^7\text{Li}|1,0\rangle$ vanishes. The obtained value for the calculation of the critical field is

$$B_0 = 1.953\,\text{G} \tag{4.4}$$

with a sensitivity of $dE_{\text{Na}^7\text{Li}}/dB = h\cdot\,650\,\text{Hz/G}$.

The next section of this chapter will focus in the stabilization of an external magnetic field at the aforementioned critical value B_0.

4.2 Active Magnetic Field Stabilization

4.2.1 Experimental Implementation

To create the required homogeneous magnetic field we employ the offset coils [56]. These coils are a set of three pairs of squared coils close to be in Helmholtz configuration with a side length of about $1\,\text{m}$. They are installed in pairs, with each pair producing a homogeneous field along each axis. The coils are designed to produce $1\,\text{G}$ per $10\,\text{A}$ and each pair is driven by a voltage controlled current source (Delta Elektronika SM35-45). The offset coils are initially used to passively cancel any DC stray magnetic field acting onto the atoms trapped in the crossed dipole trap. A known magnetic sensitive MW transition of the sodium atoms is used to probe the external magnetic field. After the DC external magnetic field is cancelled, a bias magnetic field is applied along the y-axis (see Figure 4.2) and roughly calibrated to be at $1.95\,\text{G}$.

The external bias magnetic field is actively stabilized using a closed feedback loop following the setup in [83]. In general, the feedback control starts with a voltage signal

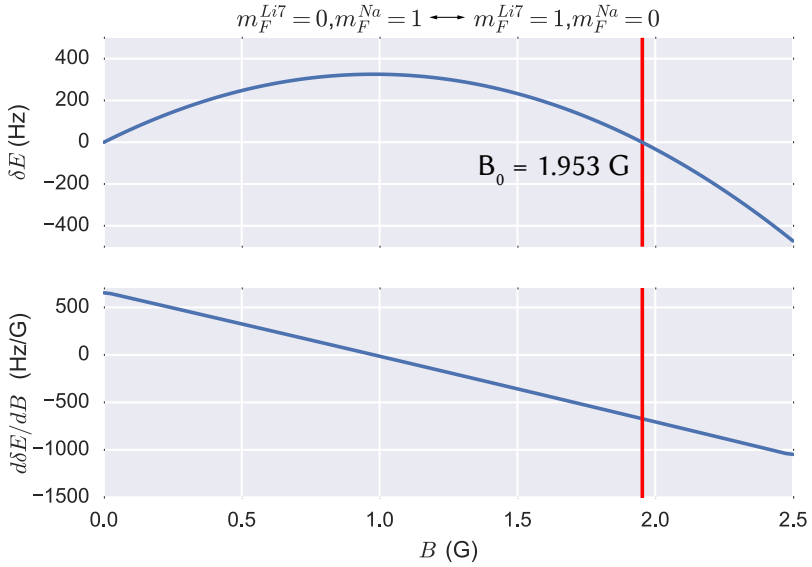

Figure 4.1: Critical magnetic field for vanishing differential Zeeman energy between the states $|1,0\rangle$ and $|1,1\rangle$ of both Na and ^{7}Li. The calculated critical field is $B_0 = 1.953\,\mathrm{G}$, indicated by the vertical line.

$r(t)$ proportional to the magnetic field acting onto the atoms, which is compared in a proportional-integral-differential (PID) controller, with a calibrated reference voltage signal $p(t)$. As a result of this comparison, the PID controller outputs a control voltage $u(t)$ used in the current source of the coils producing the magnetic field. The PID control voltage $u(t)$ is such that the difference between $r(t)$ and $p(t)$ is minimized. It is important for our experiment thus to calibrate the reference signal $p(t)$ in order to achieve the required magnetic field for the atoms.

The signal proportional to the magnetic field $r(t)$ is measured with a low noise three-axes fluxgate magnetometer (Bartington MAG-03MS1000). This magnetic field sensor has a bandwidth of $3\,\mathrm{kHz}$ within the range of $\pm 10\,\mathrm{G}$ and its output voltage is of $1\,\mathrm{V/G}$. It is installed close to the atoms, at a distance of about $10\,\mathrm{cm}$. A closer position is impossible without blocking the optical access used by the laser beams. However, due to the large size of the coils, compared to the distance from the fluxgate to the atoms, we can assume a constant difference between the magnetic field on both locations. In practice, the atoms are used to calibrate the magnetic field on the sensor.

Before feeding the analog voltage from the fluxgate sensor into the PID controller, the former is pre-processed in a board designed in [83]. This pre-process board can subtract an offset to the sensor voltage, it can amplify the resultant signal and it features a notch filter to eliminate the characteristic $15\,\mathrm{kHz}$ of working frequency of the fluxgate sensor. Its use is explained by the small ratio between the magnetic field fluctuations and the

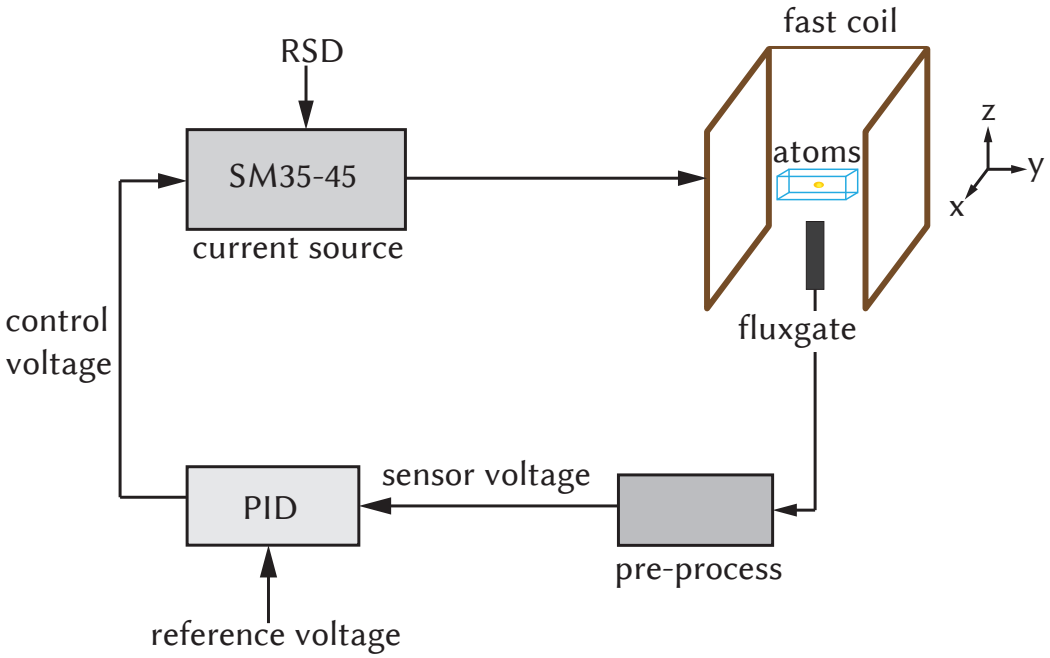

Figure 4.2: Schematics of the implementation of the active stabilization of the bias magnetic field. The voltage from the fluxgate sensor is processed before entering into the PID controller. A calibrated reference voltage is applied from the computer control and compared to the voltage measured by the sensor. The PID drives the voltage controlled current source of the coils, which can be remotely deactivated by a TTL signal connected on the remote shutdown input. The deactivation of the current source is used to bypass the active stabilization during the stages of the experimental sequence when no stabilization is needed, i.e. during the MOT, the magnetic trap and the Stern-Gerlach separation.

total signal from the fluxgate sensor. Particularly, we are working at a bias magnetic field of $1.95\,\mathrm{G}$ and the magnetic field fluctuations are expected to be much smaller than that. By subtracting a fixed voltage offset to the sensor signal and amplifying the resultant signal afterwards, the voltage from the fluxgate sensor has a larger ratio between the magnetic field fluctuations and the total average voltage. This resultant pre-processed voltage is better handled by the PID controller to correct for drifts.

Due to the low speed of the offset coil along the y-axis, that features a $3\,\mathrm{db}$ bandwidth at $36\,\mathrm{Hz}$, an additional *fast coil* was installed in the same aluminum holder where the offset coil is. This fast coil consists on only one winding and it is driven by a power supply of the same model the offset coil is driven (Delta Elektronika SM35-45). In total, the field along the y-axis is created using both coils, each one with an independent power supply in constant current (CC) mode. In this mode, the power supply keeps the output current at a constant value set by the analog control voltage coming from the experimental control. If the coils heat-up due to the energy disipated by the flowing current, meaning the resistance of the coils increases, the power supply will compensate by increasing the internal driving voltage. The offset coil with its $0.9\,\mathrm{G/V}$ creates a fixed offset field, passively stabilized with an analog control voltage. On top of that offset voltage, the fast coil with its $40\,\mathrm{mG/V}$, creates the field that is actively stabilized in the feedback loop.

During a experimental sequence, the magnetic field changes within a wide range of values, including the MOT phase, followed by the loading into the Magnetic Trap phase and the final Stern-Gerlach pulse used for magnetic population readout. During those sections, the fluxgate sensor is constantly sensing the magnetic field and its changes, which can result in disturbances if the active stabilization of the magnetic field is activated and tries to keep the magnetic field constant. To avoid the PID control to compensate for the magnetic field when it is not needed, the feedback circuit is set to open by disabling the output of the fast coil power supply with a TTL signal acting on the remote shutdown (RSD) control.

4.2.2 Spectroscopy with Active Stabilization

The first procedure, once the experimental implementation of the fast coil and the feedback loop is installed, is to calibrate the control voltage of the power supplies in order to have the required bias field of $B_0 = 1.953\,\mathrm{G}$ at the atoms position. The calibration is performed by driving the magnetic sensitive transition $|1,1\rangle \rightarrow |2,2\rangle$ of the sodium atoms trapped in the crossed dipole trap.

The magnetic field dependency of the $F = 2$ Zeeman levels of the sodium ground state scale with $m_F{\times}0.7\,\mathrm{MHz/G}$. For the atoms in the $F = 1$ manifold, the scaling goes as $-m_F{\times}0.7\,\mathrm{MHz/G}$ [65]. This information in enough to calculate the resonant frequency for the hyperfine transition $|1,1\rangle \rightarrow |2,2\rangle$ at the magnetic fied B_0. This resonance frequency is found to be ω_0^{12} =1775.7336 MHz. Considering we are working

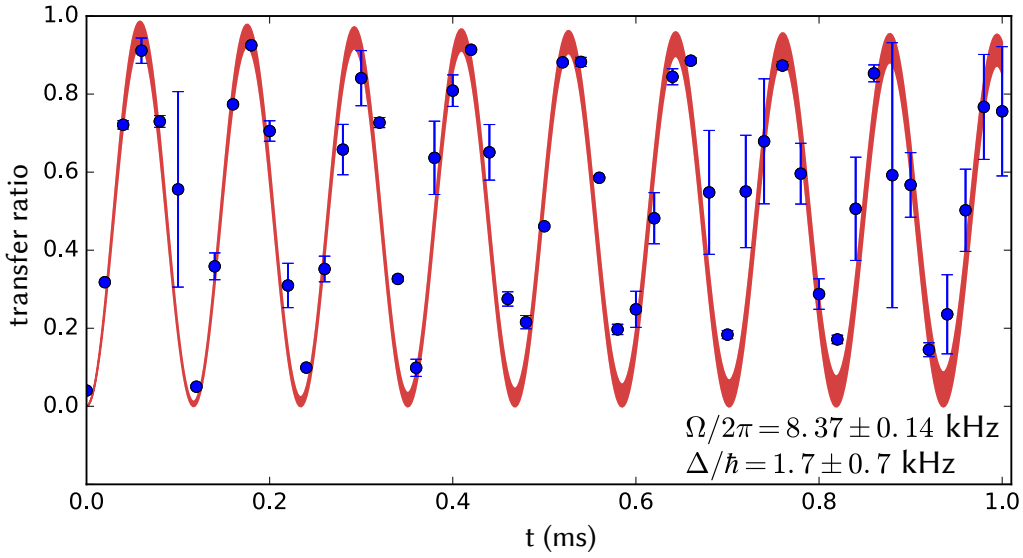

Figure 4.3: Rabi Oscillations for sodium atoms in the crossed dipole trap between $|1,1\rangle$ and $|2,2\rangle$. The plot shows the ratio of transfered atoms over non-transfered atoms, starting from $|1,1\rangle$. The fitted Rabi frequency is $\Omega = 2\pi \times 8.37(14)\,\mathrm{kHz}$.

at almost 2 G and the $0.7\,\mathrm{MHz/G}$ of difference between neighboring Zeeman levels, the different transitions from $|1,1\rangle$ to the upper manifold are well separated and can be easily discriminated when performing MW spectroscopy.

The calibration of the magnetic field starts by searching for the feature of the $|1,1\rangle$ to $|2,2\rangle$ transition with rough MW sweeps around the known frequency ω_0^{12}. This is done by adjusting the MW sweep range and the bias magnetic field in a recursive manner, until the resonant frequency is close to the required value. At this point, Rabi oscillations are performed as it can be seen in Figure 4.3. No more MW sweeps are performed but MW pulses at a fixed frequency ω_0^{12}. The scanned parameter is the duration of the Rabi MW pulse. Regarding the specific frequency ω_0^{12} we apply, our DDS setup [56] is programmed in units of Hz, thus there is no problem in programming the frequency ω_0^{12}. From the fitted detuning Δ in the Rabi oscillations measurements, we obtain a FWHM for the magnetic field to be at $\sim 1\,\mathrm{mG}$, which would correspond to energy fluctuations on the order of $dE = h \times 0.65\,\mathrm{Hz}$ according to the sensitivity of the energy difference at the critical field.

The estimated Rabi frequency from the Rabi oscillations measurement is useful for further adjustments of the bias magnetic field performed by Ramsey spectroscopy, as shown in subsection 4.2.3. Once the Rabi frequency is known, it is possible to prepare any coherent superposition between both states involved in the transition. It

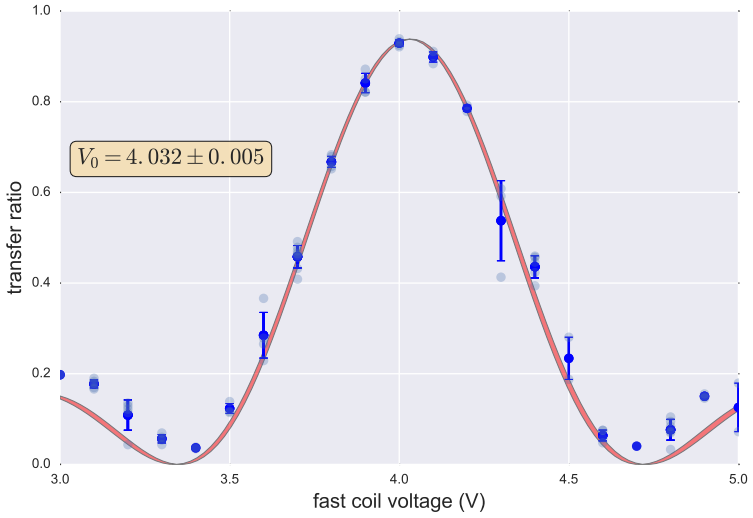

Figure 4.4: Rabi detuning for a fixed Rabi pulse driving the transition $|1,1\rangle \rightarrow |2,2\rangle$ on sodium atoms. Using the Equation 4.5 it is possible to estimate the resonant voltage of the fast coil power supply, which is found to be $V_0 = 4.032(5)$ V. The used Rabi frequency was 8.6 kHz and the images were taken after 8 ms of time of flight.

is also important to point out that before the implementation of the active magnetic field stabilization, Rabi oscillations were not possible to observe for such a transition, making it impossible to characterize the Rabi frequency of the system.

Once the Rabi frequency for the transition has been estimated, the finer calibration for the applied magnetic field consists on scanning the detuning Δ and studying the ratio of transfered atoms using the known expression for the probability to find an atom in the excited state $|2,2\rangle$:

$$P_{\mathrm{e}}^{\mathrm{Rabi}} = \frac{1}{2}\frac{\Omega^2}{\Omega^2 + \Delta^2}\left[1 - \cos\left(\sqrt{\Omega^2 + \Delta^2}\, t_{\pi/2}\right)\right] \tag{4.5}$$

where Ω is the Rabi frequency, $\Delta = \omega_{\mathrm{MW}} - \omega_0$, is the detuning, with ω_{MW} the incident MW frequency and ω_0 the resonant frequency, has the same form seen for the dipole force scenario. In Figure 4.4 a scan of ω_0 was performed by varying the magnetic field applied by the fast coil and keeping the applied MW frequency constant at the calculated value ω_0^{12}.

4.2.3 Ramsey Measurements

The Ramsey spectroscopy has shown to be a powerful method to perform precise frequency measurements, obtained from the understanding of the detuning Δ between

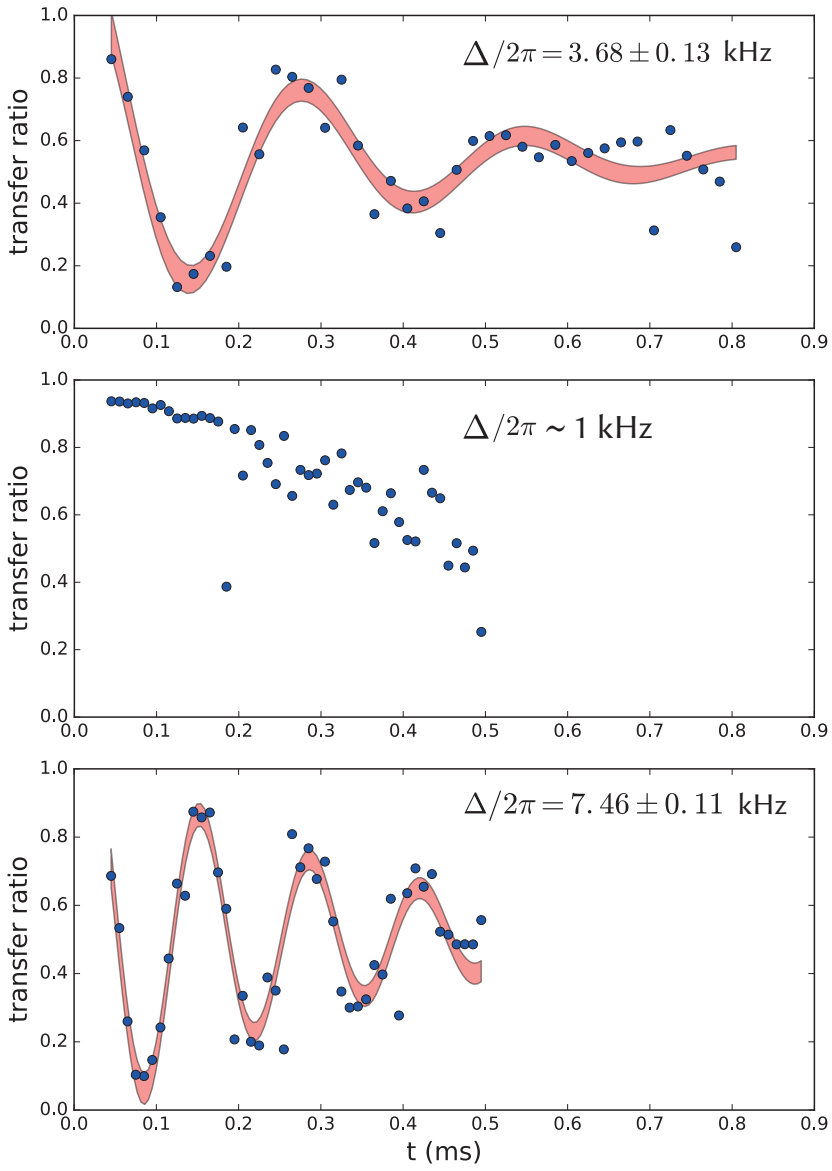

Figure 4.5: Different Ramsey fringes for sodium atoms in the crossed dipole trap at different driving frequencies ω_{MW}. The spectroscopy is done between the states $|1,1\rangle$ and $|2,2\rangle$ at a magnetic field of about B_0 =1.95 **a)** The applied driving frequency is $\omega_{\mathrm{MW}} = 1775.7336\,\mathrm{MHz}$, which according to our calculations corresponds to the resonance frequency at the required bias field B_0. **b)** A change in the driving frequency shows a completely different Ramsey fringe, where the detuning decreased, signaling the driving field is closer to the resonant transition. **c)** A further change in the driving frequency recovers the Ramsey fringe with a higher detuning compared to **a)**. All the fits include an exponential decay of the form $\exp(-t/\tau)$ to account for the contrast loss in the Ramsey fringes. For **a)** and **b)** the decay constant was found to be about $\tau = 0.3\,\mathrm{ms}$.

the driving field ω_{MW} and the resonant transition ω_0 [60, 84] . This method consists on applying two $\pi/2$-pulses separated by a long evolution time $\Delta t_{\mathrm{Ramsey}}$. Much more different than the Rabi method, where the driving field is present all the time.

The main idea of the Ramsey spectroscopy can be explained in three steps:

- The first $\pi/2$-pulse creates a coherent equally populated superposition between the studied ground state and excited states.
- During the free evolution time $\delta t_{\mathrm{Ramsey}}$, a phase $\phi = \omega_0 t$ builds up.
- For the readout of the final population, the second $\pi/2$-pulse is applied, projecting the state along the quantization axis.

From the formal calculation is obtained that for the zero detuning case $\Delta = 0$, the accumulated phase is zero and the final state is exactly the excited state. Furthermore, the periodic evolution of the probability to find an atom in the excited state evolves as:

$$P_{\mathrm{e}}^{\mathrm{Ramsey}} = \cos^2\left(\frac{\Delta\ \delta t_{\mathrm{Ramsey}}}{2}\right). \tag{4.6}$$

This is an important signature that allows us to find the correct external magnetic field for a given transition frequency ω_0^{12}. In Figure 4.5, a qualitative study was performed by Ramsey spectroscopy on sodium atoms, between the $|1,1\rangle$ and $|2,2\rangle$ states. The parameter changed among the images is the frequency of the MW driving field ω_{MW}. In **b)** can be seen a smaller detuning Δ manifested in a slower time evolution of the probability P_e^{Ramsey}. When changing ω_{MW} to either blue or red detuned frequencies, the oscillating frequency increased for both Ramsey measurements.

Due to its high sensitivity, the Ramsey spectroscopy gives us clear indications about the measurement of the resonant transition ω_0. Moreover, the decay time of the Ramsey fringe also contains information about the system, because it is closely related to the decoherence time T_2 [41]. In the measurements performed in Figure 4.5, the decay time constant τ in the exponential decay of the form $e^{(-t/\tau)}$ is for both **a)** and **c)** of about $\tau = 0.3\,\mathrm{ms}$. Although we have not investigated it in detail, a possible explanation would be magnetic field gradients along the atomic cloud causing the observed dephasing. This dephasing along the cloud would be possible to investigate with the implemented one-dimensional lattice, considering that several independent Ramsey spectroscopy will be performed, showing the detuning relationship among the lattice sites.

4.3 Preparation of the Initial Conditions

Together with the implementation of the bias magnetic field and its stabilization (section 4.2), the control over the population of the different Zeeman states within the lower

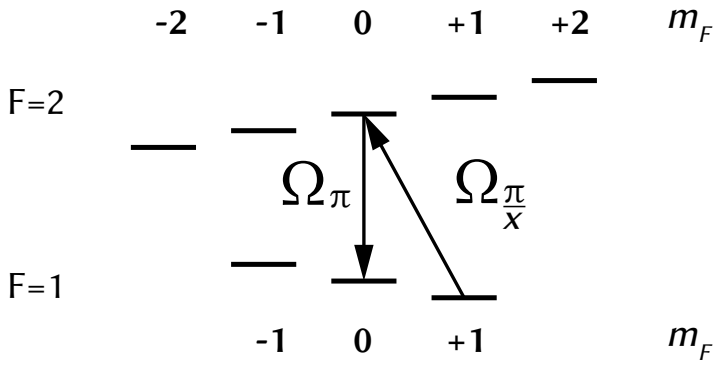

Figure 4.6: Schematics of the MW sequence to prepare an arbitrary population ratio in the ground state of sodium. The second pulse is a π-pulse to transfer all the atoms to the final state $|1,0\rangle$, whereas the first pulse defines the population ratio. A first $\pi/2$-pulse creates a balanced population between the states $|1,0\rangle$ and $|1,1\rangle$.

manifold of each atomic species is a fundamental tool for the studies on spin-changing collisions (SCC) we want to perform. A functional control over the initial population of the trapped atoms would allow us to prepare any initial condition for our atomic clouds. In our experiment, those studies will be performed within the $F = 1$ ground state manifold of sodium and lithium, specifically between the states $|1,1\rangle$ and $|1,0\rangle$.

As already discussed in section 2.3, we want to control the initial population of the sodium atoms. The required initial population for sodium is a 50:50 population balance between the states $|1,1\rangle$ and $|1,0\rangle$. In the crossed ODT stage, the sodium atoms are in $|1,1\rangle$, therefore a transfer to the $|1,0\rangle$ state has to be implemented. This will be realized by employing a two-step approach, where the atoms will be transfered first to the $|2,0\rangle$ state to be immediately transfer to their final state $|1,0\rangle$.

Driving the transition $|2,0\rangle \longrightarrow |1,0\rangle$ immediately after the transition $|1,1\rangle \longrightarrow |2,0\rangle$ has been driven was not possible with our current MW source (DDS) setup, described in [56]. The limitation comes from the time the DDS setup needs between receiving the instructions to create a pulse (or ramp) and outputting it. We measured this waiting time to be in the order of $600\,\mu s$. It is worth mentioning that this limiting time is independent of the type of programmed input, i.e. it will be there even if the two programmed pulses are identical. Waiting for $600\,\mu s$ after transferring sodium atoms to the state $|2,0\rangle$ is detrimental for our total atomic number. We observed noticeable heating and atom losses after holding the sodium atoms in $|2,0\rangle$ for $500\,\mu s$. This is a known behavior of that state [85].

In our setup, with Rabi frequencies at around $8\,kHz$, the π-pulse that completely

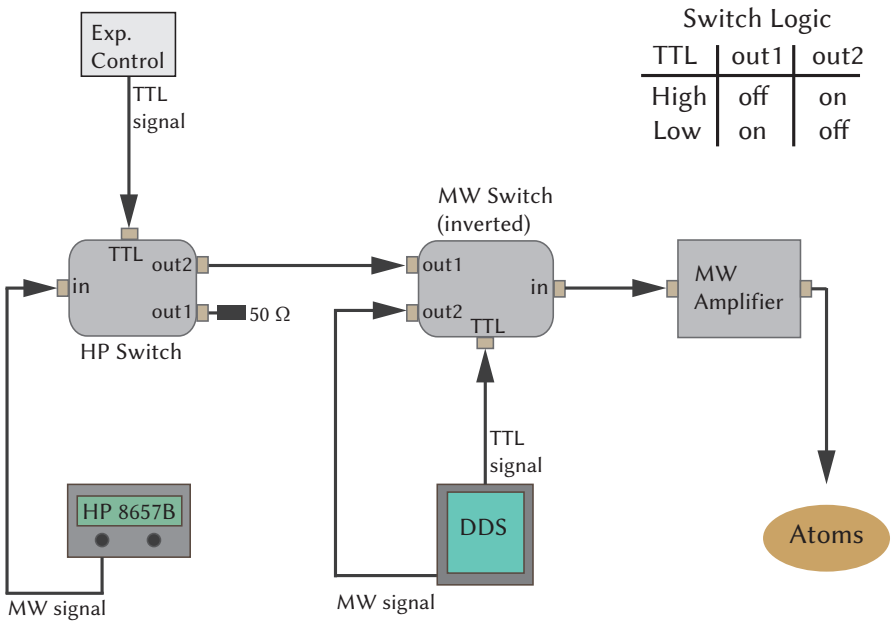

Figure 4.7: Schematics of the setup for two consecutive MW pulses. This overcomes the DDS limitation of 600 µs of waiting time between two pulses. One pulse is applied by the DDS and the other by the HP-8657B function generator. Everything is controlled by the RF switches in the line.

transfer the atoms from the initial state to the final state, is about 60 µs long.

To solve the *waiting time* problem of the DDS setup, we implemented a solution that consists on the addition of a function generator (HP-8657B) to the MW setup. This way, for the two-pulses preparation approach, the first pulse is performed by the DDS system while the second one is created by the added programmable function generator. The function generator is programmable via GPIB communication, therefore it was integrated to the computer control system to perform MW spectroscopies.

In the case of sodium, starting with the atoms in the $|1,1\rangle$ state, the first pulse to drive the atoms from $|1,1\rangle$ to $|2,0\rangle$ will be the one controlling the final population ratio between $|1,1\rangle$ and $|1,0\rangle$. For instance, to prepare a 50:50 ratio, the first pulse has to be a $\pi/2$-pulse and the second one from $|2,0\rangle$ to $|1,0\rangle$ has to be a π-pulse to completely transfer the atoms. A few changes were done to the MW setup in order to add the new source on the line, as it can be seen in Figure 4.7.

We did not use the function generator HP-8657B to perform the two required pulses, due to the long time it requires to give two pulses at different frequencies. It takes several µm to change the carrier frequency and give a second pulse, which does not meet our required time resolution of having the second pulse immediately after the first one. The function generator cannot be triggered externally with a TTL signal

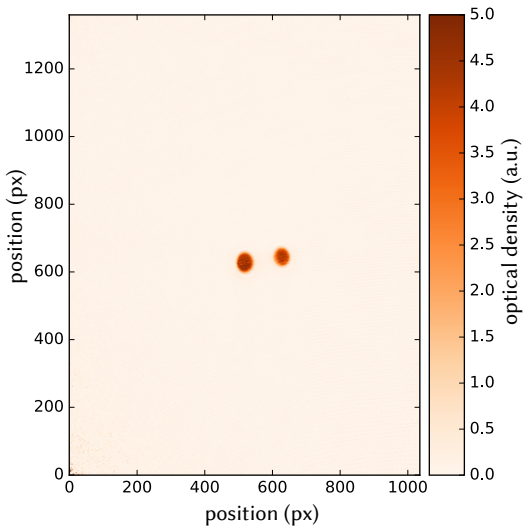

Figure 4.8: A mixture of sodium atoms in $|1,1\rangle$ and $|1,0\rangle$ states. Population imbalance is $60\,\%$ in $|1,1\rangle$ (left) and $40\,\%$ in $|1,0\rangle$ (right). Preparation was done via the setup of two consecutive MW pulses described in section 4.3. Absorption image was obtained after a Stern-Gerlach separation.

either, therefore to use it in the MW setup, the function generator output is constantly turned on at the resonant MW frequency. An RF switch (HP switch in Figure 4.7) is in charge of blocking the MW signal during the whole experimental sequence except when we need it. This is controlled with a TTL signal coming from the experimental control acting directly into the switch. For the second switch (MW Switch in Figure 4.7), the MW output signal from DDS setup is controlled by a TTL signal that comes from the DDS as well. When a MW pulse from HP-8657B is needed, a TTL signal from the DDS goes to LOW, connecting thus **out1** to **in** on the MW Switch and allowing the MW signal to be transmitted onto the atoms. This setup showed to be successful for sodium, because different population ratios were possible to prepare. As it can be seen in Figure 4.8 for a preparation of sodium atoms with a population imbalance of 60:40.

4.4 Stern-Gerlach Spin Separation

Our experiments take place within the crossed optical dipole trap at a low external bias magnetic field of $\sim 1.95\,\mathrm{G}$ with the atoms populating the lower hyperfine manifold of the ground state. As detailed in the previous section, imaging procedure consists on optically pumping the atoms to the upper manifold of the ground state where imaging

beam is resonant. This imaging technique drives all the atoms within that manifold regardless of their spin degree of freedom, hence another approach is needed in order to resolve the population of individual magnetic levels. We tackle this limitation by employing a Stern-Gerlach spin separation technique, which relies on the different magnetic moments of the spin states within the same hyperfine manifold.

The working principle of the Stern-Gerlach separation originates from the force exerted on an atom in a magnetic state when immersed in an external magnetic field gradient. Starting from the magnetic potential that reads:

$$V_{mag} = -\vec{\mu} \cdot \vec{B}, \tag{4.7}$$

the magnetic force is then:

$$\vec{F}_{mag} = \nabla(\vec{\mu} \cdot \vec{B}) \tag{4.8}$$

where $\mu = m_{\mathrm{F}}\, g_{\mathrm{F}}\, \mu_{\mathrm{B}}$ the magnetic moment of the atom in the Zeeman state $|F, m_{\mathrm{F}}\rangle$. μ_{B} is the Bohr's magneton, g_{F} is the gyromagnetic factor, m_{F} denotes the quantum number of the magnetic level of the atom and B is the magnetic field magnitude. One can immediately observe that for a given magnetic field B, different magnetic levels m_{F} experience different forces, thus accelerating in different directions. It is also clear that for atoms in Zeeman states $|F, m_{\mathrm{F}=0}\rangle$ there is no magnetic force acting on them, staying on the same position during a Stern-Gerlach separation diagnostics.

4.4.1 Investigating the Spin Separation Direction

In practice, spin separation via Stern-Gerlach is the last procedure performed before imaging takes place. The required magnetic field gradient is applied with a pair of coils contained in the magnetic coil holder and it lasts for $\sim 1\,\mathrm{ms}$ to $5\,\mathrm{ms}$, followed by a time of flight free expansion of also several ms of duration. The spatial separation is proportional to the time of flight and each one of the aforementioned variables, however high magnetic field strengths can heat up the atoms or introduce fluctuations due to bandwidth limitations of the power supply driving the coils.

In previous experiments [56, 42], the Stern-Gerlach pulse was applied using either the same configuration employed for the MOT (one Antibias and one Curvature coil) or using only one Finetune coil [64]. Both configurations result in a Stern-Gerlach separation along the axial direction of the magnetic trap, which has an angle of 8° with respect to the waveguide beam. A Stern-Gerlach separation using the MOT configuration can be seen in Figure 4.10.

In our current experiment we want to change the direction of the magnetic field gradient to be perpendicular to the waveguide, keeping it on the horizontal plane. This modification is based on orientation of the new 1-dimensional optical lattice implemented to improve the overlap of the atomic clouds. As it is explained in chapter 3,

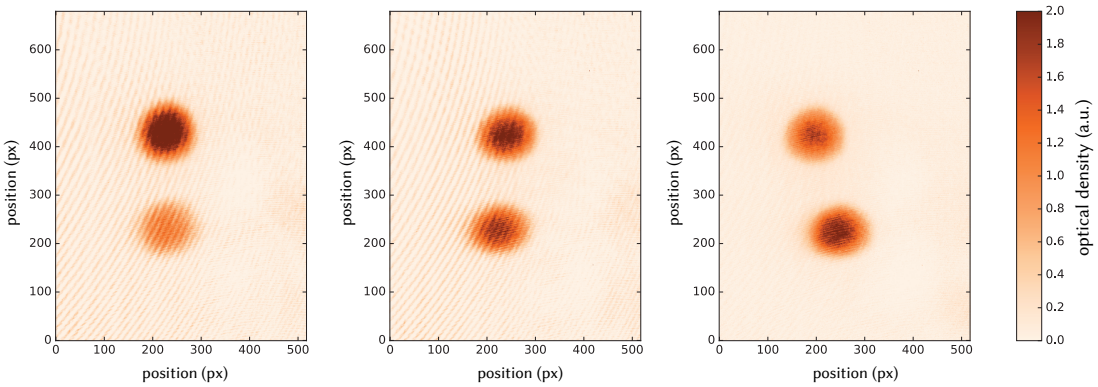

Figure 4.9: Stern-Gerlach separation perpendicular to the waveguide. Observable fluctuations on the direction of the separation of the atoms after the same Stern-Gerlach pulse. Images are taken after a time of flight of $8\,\mathrm{ms}$, Stern-Gerlach pulse has a duration of $2\,\mathrm{ms}$ and a driving voltage of $0.5\,\mathrm{V}$. Data is from a Rabi measurement, explaining the difference in population among the three pictures.

the lattice consists of lattice sites along the waveguide direction. Therefore, a Stern-Gerlach separation in the perpendicular direction is able to resolve the different magnetic states populations and more importantly, it is done individually for each lattice site, allowing us to perform the spin-changing collisions experiments.

The implementation is done using also the coils in MOT configuration with a driving voltage of $\sim 0.6\,\mathrm{V}$, which is twice the voltage used during the MOT ($0.3\,\mathrm{V}$) but much less compared to the $10\,\mathrm{V}$, that corresponds to $230\,\mathrm{A}$, used when magnetic trap is ramped up and atoms are loaded in. Separation follows the direction of the bias field as seen in Figure 4.9. However, the non symmetric nature of this pair of coils and their high inductance introduce magnetic field fluctuations [56] that are manifested in a non well defined direction for the Stern-Gerlach separation as seen in Figure 4.9.

While investigating on how to create a gradient along this new direction, the gradient coils (cloverleaf shaped) were the natural choice because they are responsible for the radial confinement during the magnetic trap. However, when testing the Stern-Gerlach separation using these coils, we observed that it separates the atoms vertically along the gravity direction even though the bias field is on the horizontal plane. This is due to the mismatch between the position of the crossed dipole trap with respect to the center of the quadrupole trap created with the cloverleaf coils. A vertical difference in the trap minima results thus in an effective gradient along the vertical direction regardless of the bias field on the horizontal plane.

Supported by the Stern-Gerlach separation, we can verify whether our spin-state

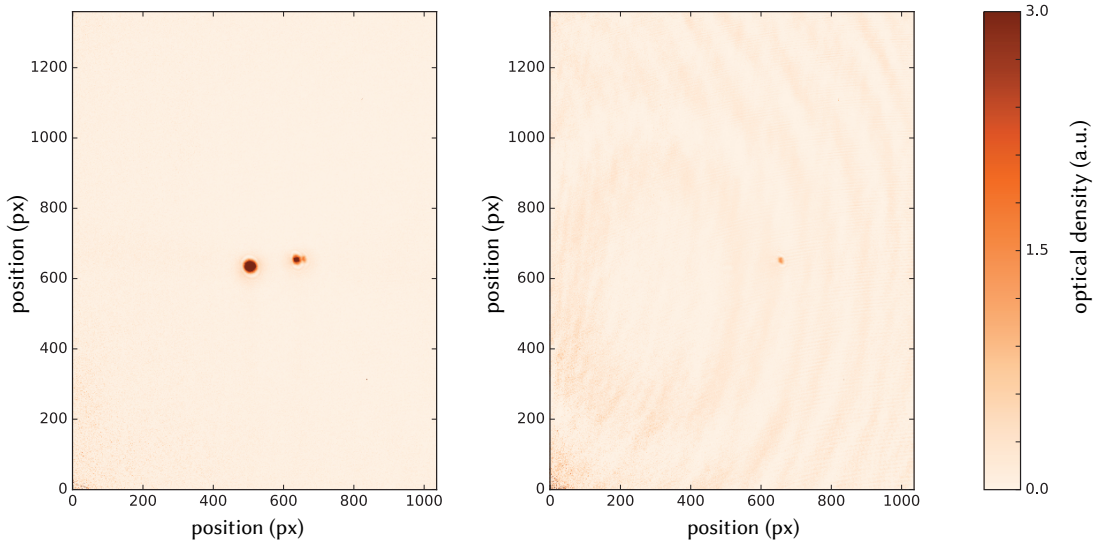

Figure 4.10: Stern-Gerlach separation along the waveguide. In general, magnetic state resolution is used to analyze the efficiency of different MW transfers. Here, sodium atoms in different Zeeman levels are imaged. States were prepared using the technique described in section 4.3. Both images are prepared identically but imaged differently. **Left:** Atoms are visible in three magnetic states: $|1,1\rangle$, $|1,0\rangle$ and $|2,0\rangle$. **Right:** Only one cloud of atoms in $|2,0\rangle$ is visible. Imaging was without repumper light, thus only atoms in upper manifold $F = 2$ are imaged.

preparation steps are successful, for instance during the MW transfer from $|2,2\rangle$ to $|1,1\rangle$ at the beginning of the ODT stage [Figure 4.10].

4.5 Concluding Remarks

In this chapter we presented the techniques related to the control of the spin states of the atomic clouds.

We presented the creation of an external magnetic field using a pair of large diameter coils. Working with these coils of a large diameter helps to reduce inhomogeneities of the magnetic field along the atoms position. We also presented the implementation of an active stabilization of such a magnetic field. The stabilization setup uses a fluxgate magnetic field sensor integrated in a feedback loop control that compensates for magnetic field drifts detected by the fluxgate sensor.

By means of the magnetic field stabilization we were able to perform Rabi oscil-

lations and to characterize the Rabi coupling of the magnetic sensitive transition $|1,1\rangle \longrightarrow |2,2\rangle$ within the hyperfine ground state of the sodium atoms. From the Rabi measurement we estimate a magnetic field stability in the $\sim 1\,\mathrm{mG}$ regimes. The characterization of the Rabi coupling allowed us to perform Ramsey spectroscopies for the same transition. The Ramsey fringes showed a decay time constant of about $3\,\mathrm{ms}$, that could indicate a magnetic field gradients along the atomic cloud that would induce the dephasing.

We explained that our MW setup has a lower limit in the time it requires to program and output two MW pulses on the order of $600\,\mu\mathrm{s}$. In order to perform the Ramsey spectroscopy, we solved this limitation by implementing an RF switch in the MW setup line. This switch blocks the constant MW signal created by the DDS setup creating thus the two used $\pi/2$-pulses.

Related to the same limitation of our DDS setup, we have implemented a solution that allows us to prepare any population imbalance between the states $|1,1\rangle$ and $|1,0\rangle$ of the sodium atoms trapped in the crossed dipole trap. The preparation is created by applying two MW pulses to drive the transition $|1,1\rangle \longrightarrow |2,0\rangle$ first, followed by a MW pulse driving the transition $|2,0\rangle \longrightarrow |1,0\rangle$. Our solution consist of using an extra function generator to create the second MW pulse.

To obtain information about the individual spin state population we have investigated the Stern-Gerlach separation. Motivated by the orientation of the one-dimensional optical lattice, we wanted to implement a Stern-Gerlach separation along the y-direction. We observed that by using the natural choice of the Gradient coils, the separation occurred along the vertical direction due to a spatial mismatch between the trap minimum of both traps. We could separate the spin components of the cloud along the required axis by driving one Antibias coil and one Curvature coil [64] at relatively low current. However, the separation direction is not reliable from shot to shot as it can be seen in Figure 4.9.

5 Conclusions and Outlook

This thesis presented our work on the experimental setup of the ^{23}Na, ^{6,7}Li mixtures experiment. We have described the modifications introduced in numerous sections of the experimental setup along with the implementation of new hardware. The invested changes aim towards the investigation of hetero-nuclear spin dynamics between both species.

We upgraded the laser setup for both atomic species, improving their performance and reliability. In the case of sodium, we exchanged the laser source employed for all the required frequencies involved in the trapping and cooling of the atoms. The new laser source has reduced dramatically the time needed to start the experiment, as well as it has improved the stability of the available laser power along the day. In the same context, we updated several beam paths that were limiting the adjustment of the optical setup, specifically the MOT beam path and the repumper beam path. Those changes showed to be useful when the new laser was installed, because we adjusted and recoupled every beam path. In the case of lithium, we implemented a fiber injected TA which amplifies the available laser power for the repumper light. The new repumper beam path features a double-pass AOM setup required to trap ^{7}Li.

In order to improve the overlap between sodium and lithium, we modified the vertical waist of the waveguide beam that created the crossed optical dipole trap. We decreased the beam waist from $60\,\mu\mathrm{m}$ to about $33\,\mu\mathrm{m}$ The new differential gravitational sag between sodium and lithium is on the order of $\Delta = 1\,\mu\mathrm{m}$, which is about 1 order of magnitude smaller than the old spatial mismatch. Within the same context of confinement of the atoms, we described the implementation of a new one-dimensional optical lattice created with blue detuned light at $532\,\mathrm{nm}$. The implemented lattice has a lattice spacing of about a_{lat} =$10.6\,\mu\mathrm{m}$. The maximum trap depth for sodium is $75\,\mathrm{E_R}$, where the energy recoil is $E_{\mathrm{R}} = h\times\,20\,\mathrm{Hz}$, and the trapping frequency is about $1\,\mathrm{kHz}$. Due to the construction of the lattice, it is not difficult to change those parameters. The lattice spacing is given by the focusing lens, which is $f = 200\,\mathrm{mm}$ at the moment. On the other hand, the lattice depth can be changed by controlling the maximum power of the beams.

We implemented an actively stabilized magnetic field offset to tune the energy difference between the Zeeman states $|1,1\rangle$ and $|1,0\rangle$ of both sodium and bosonic lithium. We calibrated the magnetic field by performing spectroscopy on the magnetic sensitive and stable transition $|1,1\rangle \rightarrow |2,2\rangle$ yielding to a magnetic field stability in the $\sim 1\,\mathrm{mG}$ regime. In order to perform such spectroscopy techniques, we investigated the

time limitations of our MW setup and we observed it had a dead time of about $0.6\,\mathrm{ms}$ between MW pulses, even if the two pulses are equal. This posed great limitations for the implementation of the Ramsey spectroscopy and further state manipulations. We detailed our solution consisting on the integration of a GPIB function generator to the MW setup, which is programmed by the same control system that manages the experimental sequences.

In order to demonstrate the control over the Zeeman states we gained with the updated MW setup, we have shown the possibility to prepare an arbitrary population ratio between the states $|1,1\rangle$ and $|1,0\rangle$ of sodium, using two consecutive MW transitions. This will allow us to perform hetero-nuclear spin dynamics studies with different initial conditions. To measure the population of the different Zeeman states, we investigated the Stern-Gerlach separation technique along two perpendicular directions on the horizontal plane. We aim to separate the atoms perpendicularly to the one-dimensional lattice to be able to obtain the population difference of each lattice site. However, our investigations showed that such separation direction was not reliable. We had to drive the coils at low current which resulted in slow separations and visible fluctuations on separation direction. Increasing the driving current would change separation direction to be along the lattice.

Although it would be possible to start performing experiments, several technical challenges will be addressed in the near future in order to obtain more information when performing the experiments within the optical lattice. One particular problem that could harm our measurements, is the non-homogeneity of the magnetic field on the dipole trap area. We can probe such gradient by performing spectroscopy onto the atoms arranged in the optical lattice, however it would require to implement a site resolved Stern-Gerlach separation.

Recently, experimental upgrades have been introduced to the lithium setup. The homebuilt master laser has been exchanged by a commercial diode laser unit (DL PRO, TOPTICA) to improve the performance of the locking scheme. Due to the low mass of the lithium atoms, it is more critical to image them via absorption imaging in comparison to heavier atoms, because lithium atoms are driven out of resonance with a few scattered photons [86]. To improve the detection of the lithium atoms, the imaging camera was exchanged for an EMCCD camera with high quantum efficiency (Nüvü HNü 512).

The oven performance is a topic that has been present in the discussions throughout the years of the experiment. We could find a sweet-spot that allowed us to run the machine for several months without difficulties, however, it is not a final solution. A new oven design has been designed recently, which will not feature the mixing chamber of the current design. It is expected to improve the atomic flux and simplify the refilling process of the material reservoirs.

The modifications introduced in the experiment have shown to be in the right direction towards the studies on coherent spin dynamics between sodium and bosonic lithium. Extending the knowledge about hetero-nuclear spin dynamics can provide more insight on the nature of spin-spin coupling interaction, as well as it can confirm the platform of spinor gases as a reliable tool for the implementation of further challenging systems, such as dynamics of lattice gauge theories in real time [59], and the bosonic kondo effect [87, 88] .

List of Figures

Bibliography

[1] M. H. Anderson, J. R. Ensher, M. R. Matthews, C. E. Wieman, and E. A. Cornell. "Observation of Bose-Einstein Condensation in a Dilute Atomic Vapor". In: *Science* 269.5221 (1995), pp. 198–201. ISSN: 0036-8075. DOI: 10.1126/science.269.5221.198.

[2] C. C. Bradley, C. A. Sackett, J. J. Tollett, and R. G. Hulet. "Evidence of Bose-Einstein Condensation in an Atomic Gas with Attractive Interactions". In: *Phys. Rev. Lett.* 75 (9 1995), pp. 1687–1690. DOI: 10.1103/PhysRevLett.75.1687.

[3] K. B. Davis, M.-O. Mewes, M. R. Andrews, N. J. van Druten, D. S. Durfee, D. M. Kurn, and W. Ketterle. "Bose-Einstein Condensation in a Gas of Sodium Atoms". In: *Phys. Rev. Lett.* 75.22 (Nov. 1995), p. 3969. DOI: 10.1103/PhysRevLett.75.3969.

[4] Franco Dalfovo, Stefano Giorgini, Lev P. Pitaevskii, and Sandro Stringari. "Theory of Bose-Einstein condensation in trapped gases". In: *Rev. Mod. Phys.* 71.3 (Apr. 1999), p. 463.

[5] Immanuel Bloch, Jean Dalibard, and Wilhelm Zwerger. "Many-body physics with ultracold gases". In: *Rev. Mod. Phys.* 80 (3 July 2008), pp. 885–964. DOI: 10.1103/RevModPhys.80.885.

[6] E. A. Cornell and C. E. Wieman. "Nobel Lecture: Bose-Einstein condensation in a dilute gas, the first 70 years and some recent experiments". In: *Rev. Mod. Phys.* 74 (3 Aug. 2002), pp. 875–893. DOI: 10.1103/RevModPhys.74.875.

[7] Wolfgang Ketterle. "Nobel lecture: When atoms behave as waves: Bose-Einstein condensation and the atom laser". In: *Rev. Mod. Phys.* 74 (4 Nov. 2002), pp. 1131–1151. DOI: 10.1103/RevModPhys.74.1131.

[8] Satyendra Bose. "Plancks Gesetz und Lichtquantenhypothese". In: *Z. Phys.* 26.3 (1924), p. 178.

[9] A. Einstein. "Quantentheorie des einatomigen idealen Gases. Zweite Abhandlung". In: *Sitzungber. Preuss. Akad. Wiss.* 1925 (Jan. 1925), p. 3.

[10] W. D. Phillips and H. J. Metcalf. "Cooling and trapping atoms". In: *Scientific American* 256 (Mar. 1987), pp. 50–56. DOI: 10.1038/scientificamerican0387-50.

[11] Claude N. Cohen-Tannoudji and William D. Phillips. "New Mechanisms for Laser Cooling". In: *Phys. Today* 43.10 (Oct. 1990), p. 33.

[12] N. R. Newbury and C. Wieman. "Resource Letter TNA-1: Trapping of neutral atoms". In: *Am. J. Phys.* 64.1 (Jan. 1996), p. 18.

[13] Wolfgang Ketterle and N. J. van Druten. "Evaporative Cooling of Trapped Atoms". In: *Adv. At. Mol. Opt. Phys.* 37.0 (1996), p. 181.

[14] R. Grimm, M. Weidemüller, and Y.B. Ovchinnikov. "Optical dipole traps for neutral atoms". In: *Advances in atomic, molecular, and optical physics* 42 (2000), pp. 95–170.

[15] F. S. Cataliotti, S. Burger, C. Fort, P. Maddaloni, F. Minardi, A. Trombettoni, A. Smerzi, and M. Inguscio. "Josephson Junction Arrays with Bose-Einstein condensates". In: *Science* 293 (Aug. 2001), p. 843.

[16] O. Morsch, J. H. Müller, M. Cristiani, D. Ciampini, and E. Arimondo. "Bloch Oscillations and Mean-Field Effects of Bose-Einstein Condensates in 1D Optical Lattices". In: *Phys. Rev. Lett.* 87 (14 Sept. 2001), p. 140402. DOI: 10.1103/PhysRevLett.87.140402.

[17] Markus Greiner, Olaf Mandel, Tilman Esslinger, Theodor W Hänsch, and Immanuel Bloch. "Quantum phase transition from a superfluid to a Mott insulator in a gas of ultracold atoms". In: *nature* 415.6867 (2002), pp. 39–44.

[18] S. L. Cornish, N. R. Claussen, J. L. Roberts, E. A. Cornell, and C. E. Wieman. "Stable ^{85}Rb Bose-Einstein Condensates with Widely Tunable Interactions". In: *Phys. Rev. Lett.* 85.9 (Aug. 2000), p. 1795.

[19] G. Roati, M. Zaccanti, C. D'Errico, J. Catani, M. Modugno, A. Simoni, M. Inguscio, and G. Modugno. "^{39}K Bose-Einstein Condensate with Tunable Interactions". In: *Phys. Rev. Lett.* 99 (1 July 2007), p. 010403. DOI: 10.1103/PhysRevLett.99.010403.

[20] G. Modugno, G. Ferrari, G. Roati, R. J. Brecha, A. Simoni, and M. Inguscio. "Bose-Einstein Condensation of Potassium Atoms by Sympathetic Cooling". In: *Science* 294.5545 (Nov. 2001), p. 1320.

[21] Tino Weber, Jens Herbig, Michael Mark, Hanns-Christoph Nägerl, and Rudolf Grimm. "Bose-Einstein Condensation of Cesium". In: *Science* 299 (Jan. 2003), p. 232.

[22] Yosuke Takasu, Kenichi Maki, Kaduki Komori, Tetsushi Takano, Kazuhito Honda, Mitsutaka Kumakura, Tsutomu Yabuzaki, and Yoshiro Takahashi. "Spin-Singlet Bose-Einstein Condensation of Two-Electron Atoms". In: *Phys. Rev. Lett.* 91.4 (July 2003), p. 040404.

[23] Simon Stellmer, Meng Khoon Tey, Bo Huang, Rudolf Grimm, and Florian Schreck. "Bose-Einstein Condensation of Strontium". In: *Phys. Rev. Lett.* 103 (20 Nov. 2009), p. 200401. DOI: 10.1103/PhysRevLett.103.200401.

[24] Andrew D. Ludlow, Martin M. Boyd, Jun Ye, E. Peik, and P. O. Schmidt. "Optical atomic clocks". In: *Rev. Mod. Phys.* 87 (2 June 2015), pp. 637–701. DOI: 10.1103/RevModPhys.87.637.

[25] Axel Griesmaier, Jörg Werner, Sven Hensler, Jürgen Stuhler, and Tilman Pfau. "Bose-Einstein Condensation of Chromium". In: *Phys. Rev. Lett.* 94 (16 2005), p. 160401. DOI: 10.1103/PhysRevLett.94.160401.

[26] Mingwu Lu, Nathaniel Q. Burdick, Seo Ho Youn, and Benjamin L. Lev. "Strongly Dipolar Bose-Einstein Condensate of Dysprosium". In: *Phys. Rev. Lett.* 107 (19 2011), p. 190401. DOI: 10.1103/PhysRevLett.107.190401.

[27] K. Aikawa, A. Frisch, M. Mark, S. Baier, A. Rietzler, R. Grimm, and F. Ferlaino. "Bose-Einstein Condensation of Erbium". In: *Phys. Rev. Lett.* 108 (21 2012), p. 210401. DOI: 10.1103/PhysRevLett.108.210401.

[28] C. Pethick and H. Smith. *Bose-Einstein condensation in dilute gases*. Cambridge Univ Pr, 2002. ISBN: 0521665809.

[29] L.P. Pítajevskíj, L.P.P. S. Stringari, L.P. Pitaevskii, S. Stringari, S. Stringari, and Oxford University Press. *Bose-Einstein Condensation*. International Series of Monographs on Physics. Clarendon Press, 2003. ISBN: 9780198507192.

[30] C. J. Myatt, E. A. Burt, R. W. Ghrist, E. A. Cornell, and C. E. Wieman. "Production of Two Overlapping Bose-Einstein Condensates by Sympathetic Cooling". In: *Phys. Rev. Lett.* 78.4 (Jan. 1997), p. 586.

[31] F. Schreck, L. Khaykovich, K. L. Corwin, G. Ferrari, T. Bourdel, J. Cubizolles, and C. Salomon. "Quasipure Bose-Einstein Condensate Immersed in a Fermi Sea". In: *Phys. Rev. Lett.* 87.8 (Aug. 2001), p. 080403.

[32] Andrew G. Truscott, Kevin E. Strecker, William I. McAlexander, Guthrie B. Partridge, and Randall G. Hulet. "Observation of Fermi Pressure in a Gas of Trapped Atoms". In: *Science* 291.5513 (Mar. 2001), p. 2570.

[33] Immanuel Bloch, Markus Greiner, Olaf Mandel, Theodor W. Hänsch, and Tilman Esslinger. "Sympathetic cooling of $^{85}\mathrm{Rb}$ and $^{87}\mathrm{Rb}$". In: *Phys. Rev. A* 64 (2 2001), p. 021402. DOI: 10.1103/PhysRevA.64.021402.

[34] G. Modugno, M. Modugno, F. Riboli, G. Roati, and M. Inguscio. "Two Atomic Species Superfluid". In: *Phys. Rev. Lett.* 89 (19 2002), p. 190404. DOI: 10.1103/PhysRevLett.89.190404.

[35] Selim Jochim, Markus Bartenstein, Alexander Altmeyer, Gerhard Hendl, Stefan Riedl, Cheng Chin, J Hecker Denschlag, and Rudolf Grimm. "Bose-Einstein condensation of molecules". In: *Science* 302.5653 (2003), pp. 2101–2103.

[36] Cheng Hsun Wu, Jee Woo Park, Peyman Ahmadi, Sebastian Will, and Martin W. Zwierlein. "Ultracold fermionic Feshbach molecules of Na23K40". In: *Phys. Rev. Lett.* 109.8 (2012), pp. 18–21. DOI: 10.1103/PhysRevLett.109.085301.

[37] André Schirotzek, Cheng-Hsun Wu, Ariel Sommer, and Martin W. Zwierlein. "Observation of Fermi Polarons in a Tunable Fermi Liquid of Ultracold Atoms". In: *Phys. Rev. Lett.* 102 (23 June 2009), p. 230402. DOI: 10.1103/PhysRevLett.102.230402.

[38] Sebastian Will, Thorsten Best, Simon Braun, Ulrich Schneider, and Immanuel Bloch. "Coherent Interaction of a Single Fermion with a Small Bosonic Field". In: *Phys. Rev. Lett.* 106 (11 Mar. 2011), p. 115305. DOI: 10.1103/PhysRevLett.106.115305.

[39] J. Catani, G. Lamporesi, D. Naik, M. Gring, M. Inguscio, F. Minardi, A. Kantian, and T. Giamarchi. "Quantum dynamics of impurities in a one-dimensional Bose gas". In: *Phys. Rev. A* 85 (2 Feb. 2012), p. 023623. DOI: 10.1103/PhysRevA.85.023623.

[40] Marco Koschorreck, Daniel Pertot, Enrico Vogt, Bernd Fröhlich, Michael Feld, and Michael Köhl. "Attractive and repulsive Fermi polarons in two dimensions". In: *Nature* 485.7400 (2012), pp. 619–622. ISSN: 00280836. DOI: 10.1038/nature11151.

[41] R Scelle, T Rentrop, A Trautmann, T Schuster, and MK Oberthaler. "Motional coherence of fermions immersed in a Bose gas". In: *Phys. Rev. Lett.* 111.7 (2013), p. 070401.

[42] Tobias Rentrop. "Observation of the Phononic Lamb Shift with a Synthetic Vacuum". PhD thesis. University of Heidelberg, 2016.

[43] J. Stenger, S. Inouye, D. M. Stamper-Kurn, H. J. Miesner, A. P. Chikkatur, and W. Ketterle. "Spin domains in ground-state Bose-Einstein condensates". In: *Nature* 396.6709 (1998), pp. 345–348. DOI: 10.1038/24567.

[44] C. Gross, T. Zibold, E. Nicklas, J. Estève, and M. K. Oberthaler. "Nonlinear atom interferometer surpasses classical precision limit". In: *Nature* 464.7292 (2010), pp. 1165–1169. DOI: 10.1038/nature08919.

[45] D. M. Stamper-Kurn, M. R. Andrews, A. P. Chikkatur, S. Inouye, H.-J. Miesner, J. Stenger, and W. Ketterle. "Optical Confinement of a Bose-Einstein Condensate". In: *Phys. Rev. Lett.* 80.10 (Mar. 1998), p. 2027.

[46] Cheng Chin, Rudolf Grimm, Paul Julienne, and Eite Tiesinga. "Feshbach resonances in ultracold gases". In: *Rev. Mod. Phys.* 82 (2 Apr. 2010), pp. 1225–1286. DOI: 10.1103/RevModPhys.82.1225.

[47] M. Bartenstein, A. Altmeyer, S. Riedl, S. Jochim, C. Chin, J. Hecker Denschlag, and R. Grimm. "Collective Excitations of a Degenerate Gas at the BEC-BCS Crossover". In: *Phys. Rev. Lett.* 92 (20 May 2004), p. 203201. DOI: 10.1103/PhysRevLett.92.203201.

[48] C. A. Regal, M. Greiner, and D. S. Jin. "Observation of Resonance Condensation of Fermionic Atom Pairs". In: *Phys. Rev. Lett.* 92 (4 Jan. 2004), p. 040403. DOI: 10.1103/PhysRevLett.92.040403.

[49] M. W. Zwierlein, C. A. Stan, C. H. Schunck, S. M. F. Raupach, A. J. Kerman, and W. Ketterle. "Condensation of Pairs of Fermionic Atoms near a Feshbach Resonance". In: *Phys. Rev. Lett.* 92 (12 Mar. 2004), p. 120403. DOI: 10.1103/PhysRevLett.92.120403.

[50] T. Bourdel, L. Khaykovich, J. Cubizolles, J. Zhang, F. Chevy, M. Teichmann, L. Tarruell, S. J. J. M. F. Kokkelmans, and C. Salomon. "Experimental Study of the BEC-BCS Crossover Region in Lithium 6". In: *Phys. Rev. Lett.* 93 (5 July 2004), p. 050401. DOI: 10.1103/PhysRevLett.93.050401.

[51] Dan M. Stamper-Kurn and Masahito Ueda. "Spinor Bose gases: Symmetries, magnetism, and quantum dynamics". In: *Rev. Mod. Phys.* 85 (3 July 2013), pp. 1191–1244. DOI: 10.1103/RevModPhys.85.1191.

[52] A. T. Black, L. D. Turner, E. Gomez, S. Jung, and P. D. Lett. "Spin dynamics in an antiferromagnetic spin-1 condensate". In: *2007 Quantum Electronics and Laser Science Conference*. May 2007, pp. 1–2. DOI: 10.1109/QELS.2007.4431783.

[53] H. K. Pechkis, J. P. Wrubel, A. Schwettmann, P. F. Griffin, R. Barnett, E. Tiesinga, and P. D. Lett. "Spinor Dynamics in an Antiferromagnetic Spin-1 Thermal Bose Gas". In: *Phys. Rev. Lett.* 111.2 (2013), p. 025301. ISSN: 0031-9007. DOI: 10.1103/PhysRevLett.111.025301.

[54] J S Krauser, U Ebling, N Fläschner, J Heinze, K Sengstock, M Lewenstein, a Eckardt, and C Becker. "Giant spin oscillations in an ultracold Fermi sea." In: *Science* 343.6167 (2014), pp. 157–60. ISSN: 1095-9203. DOI: 10.1126/science.1244059.

[55] Xiaoke Li, Bing Zhu, Xiaodong He, Fudong Wang, Mingyang Guo, Zhi-Fang Xu, Shizhong Zhang, and Dajun Wang. "Coherent Heteronuclear Spin Dynamics in an Ultracold Spinor Mixture". In: *Phys. Rev. Lett.* 114 (25 June 2015), p. 255301. DOI: 10.1103/PhysRevLett.114.255301.

[56] Arno Trautmann. "Spin Dynamics and Feshbach Resonances in Ultracold Sodium-Lithium Mixtures". PhD thesis. University of Heidelberg, 2016.

[57] V Kasper, F Hebenstreit, M Oberthaler, and J Berges. "Schwinger pair production with ultracold atoms". In: *arXiv preprint arXiv:1506.01238* (2015).

[58] V Kasper, F Hebenstreit, F Jendrzejewski, M K Oberthaler, and J Berges. "Implementing quantum electrodynamics with ultracold atomic systems". In: *New Journal of Physics* 19.2 (2017), p. 023030.

[59] T. V. Zache, F. Hebenstreit, F. Jendrzejewski, M. K. Oberthaler, J. Berges, and P. Hauke. "Quantum simulation of lattice gauge theories using Wilson fermions". In: *ArXiv e-prints* (Feb. 2018). arXiv: 1802.06704.

[60] T. Rentrop, A. Trautmann, F. A. Olivares, F. Jendrzejewski, A. Komnik, and M. K. Oberthaler. "Observation of the Phononic Lamb Shift with a Synthetic Vacuum". In: *Phys. Rev. X* 6 (4 Nov. 2016), p. 041041.

[61] C. A. Stan and W. Ketterle. "Multiple species atom source for laser-cooling experiments". In: *Review of Scientific Instruments* 76.6 (2005), p. 063113.

[62] Marc Repp. "Aufbau einer Vakuumapparatur für Experimente mit ultrakalten fermionischen und bosonischen Quantengasen". Diplomarbeit. University of Heidelberg, 2007.

[63] Agilent Technologies Inc., ed. *High and Ultra-High Vacuum for Science Research.* Seminar Handbook. 2011, p. 15.

[64] Jens Appmeier. "Immersed Quantum Systems: A Sodium Bose-Einstein Condensate for Polaron Studies". PhD thesis. University of Heidelberg, 2010.

[65] Daniel A Steck. "Sodium D line data". In: *Report, Los Alamos National Laboratory, Los Alamos* 124 (2000).

[66] Tanja Behrle. "Construction and Characterization of a Diode Laser Setup and Spectroscopy Cell for 6Li and 7Li". Bachelor thesis. University of Heidelberg, 2014.

[67] Arno Trautmann. "Feshbach Spectroscopy of Sodium and Sodium-Lithium Mixtures". Diplomarbeit. University of Heidelberg, 2011.

[68] Matthias Henrich. "Design and Realization of a Laser System for ATTA of Argon 39". Diploma thesis. University of Heidelberg, 2010.

[69] Jan Krieger. "Zeeman-Slower und Experimentiersteuerung für das NaLi-Experiment". Diplomarbeit. Universität Heidelberg, 2008.

[70] Wolfgang Ketterle, Kendall B. Davis, Michael A. Joffe, Alex Martin, and David E. Pritchard. "High densities of cold atoms in a dark spontaneous-force optical trap". In: *Phys. Rev. Lett.* 70 (15 Apr. 1993), pp. 2253–2256.

[71] F. Schreck, G. Ferrari, KL Corwin, J. Cubizolles, L. Khaykovich, M.O. Mewes, and C. Salomon. "Sympathetic cooling of bosonic and fermionic lithium gases towards quantum degeneracy". In: *Physical Review A* 64.1 (2001), p. 011402.

[72] C. J. Myatt, E. A. Burt, R. W. Ghrist, E. A. Cornell, and C. E. Wieman. "Production of Two Overlapping Bose-Einstein Condensates by Sympathetic Cooling". In: *Phys. Rev. Lett.* 78 (4 Jan. 1997), pp. 586–589.

[73] David E. Pritchard. "Cooling Neutral Atoms in a Magnetic Trap for Precision Spectroscopy". In: *Phys. Rev. Lett.* 51 (15 1983), pp. 1336–1339.

[74] Ettore Majorana. "Atomi orientati in campo magnetico variabile". In: *Il Nuovo Cimento (1924-1942)* 9.2 (Feb. 1932), pp. 43–50.

[75] A. Görlitz, T. L. Gustavson, A. E. Leanhardt, R. Löw, A. P. Chikkatur, S. Gupta, S. Inouye, D. E. Pritchard, and W. Ketterle. "Sodium Bose-Einstein Condensates in the $F = 2$ State in a Large-Volume Optical Trap". In: *Phys. Rev. Lett.* 90 (9 2003), p. 090401.

[76] Fred Jendrzejewski. "Quantum transport of ultracold atoms in disordered potentials". Theses. Université Paris Sud - Paris XI, Nov. 2012. URL: https://tel.archives-ouvertes.fr/tel-00809290.

[77] Alexander Mil. "Design and Implementation of a Versatile Imaging Objective for Imaging of Ultracold Mixtures of Sodium and Lithium". Master thesis. University of Heidelberg, 2016.

[78] M.E. Gehm. "Properties of ^{6}Li". In: *The current version of the document is available at http://www.phy.duke.edu/research/photon/qoptics/techdocs* 58 (2003).

[79] Wolfgang Muessel, Helmut Strobel, Maxime Joos, Eike Nicklas, Ion Stroescu, Jiří Tomkovič, David B. Hume, and Markus K. Oberthaler. "Optimized absorption imaging of mesoscopic atomic clouds". In: *Applied Physics B* 113.1 (2013), pp. 69–73. ISSN: 1432-0649. DOI: 10.1007/s00340-013-5553-8.

[80] J. J. Zirbel, K.-K. Ni, S. Ospelkaus, T. L. Nicholson, M. L. Olsen, P. S. Julienne, C. E. Wieman, J. Ye, and D. S. Jin. "Heteronuclear molecules in an optical dipole trap". In: *Phys. Rev. A* 78 (1 2008), p. 013416. DOI: 10.1103/PhysRevA.78.013416.

[81] Raphael Scelle. "Dynamics and Motional Coherence of Fermions Immersed in a Bose Gas". PhD thesis. University of Heidelberg, 2013.

[82] G. Breit and I. I. Rabi. "Measurement of Nuclear Spin". In: *Phys. Rev.* 38 (11 Dec. 1931), pp. 2082–2083. DOI: 10.1103/PhysRev.38.2082.2.

[83] Marcel W. Gall. "Active Magnetic Field Stabilisation for Ultracold Sodium Lithium Mixtures". Master thesis. University of Heidelberg, 2015.

[84] Norman F. Ramsey. "A Molecular Beam Resonance Method with Separated Oscillating Fields". In: *Phys. Rev.* 78 (6 June 1950), pp. 695–699.

[85] A. Görlitz, T. L. Gustavson, A. E. Leanhardt, R. Löw, A. P. Chikkatur, S. Gupta, S. Inouye, D. E. Pritchard, and W. Ketterle. "Sodium Bose-Einstein Condensates in the $F = 2$ State in a Large-Volume Optical Trap". In: *Phys. Rev. Lett.* 90.9 (Mar. 2003), p. 090401.

[86] A. Bergschneider, V. M. Klinkhamer, J. Hendrik Becher, R. Klemt, G. Zürn, P. M. Preiss, and S. Jochim. "Spin-resolved single-atom imaging of ^{6}Li in free space". In: *ArXiv e-prints* (Apr. 2018). arXiv: 1804.04871 [cond-mat.quant-gas].

[87] L.-M. Duan. "Controlling ultracold atoms in multi-band optical lattices for simulation of Kondo physics". In: *EPL (Europhysics Letters)* 67.5 (2004), p. 721.

[88] Michael Foss-Feig and Ana Maria Rey. "Phase diagram of the bosonic Kondo-Hubbard model". In: *Phys. Rev. A* 84 (5 Nov. 2011), p. 053619. DOI: 10.1103/PhysRevA.84.053619.

Agradecimientos

In this page, I would like to say thanks to all the people that were involved in one way or another in the realization of this thesis.

- To Prof. Markus Oberthaler, for letting me work in the NaLi experiment, allowing me to learn about experimental ultracold gases. His support along the years and his curiosity for physics has been very valuable and inspiring for me.
- To Prof. Fred Jendrejewski, for the supervision and support throughout the years working in the NaLi. For the ideas and solutions whenever a problem appeared in the experiment, which were not a few! And for the corrections on this manuscript.
- To Prof. Matthias Weidemüller, for his willingness to prepare the second evaluation of this thesis.
- A mi familia, por todo lo que significan para mi. A mis padres, por el apoyo sin condiciones a lo largo de todos estos años de estudios. Por siempre estar presentes para conversar semana a semana, estando al otro lado del mundo. A mis hermanos Blaudio y Felipe, y a mi hermana Valentina, por ser los mejores hermanos. Por siempre entregar ánimos, por apoyarme y por hacer tan inolvidables mis esporádicas visitas a la familia.
- A Natalia, por todo el cariño, el apoyo y la paciencia.
- To Alexander Mil, for being the best teammate during all these years. For the teamwork in the lab and all the interesting discussions we had, either looking for solutions to the experimental challenges or about discovering music to listen to in the lab. For the discussions about vacuum, ion pumps and Aluminiumfolie together with Rammstein, Carpenter Brut and Dynatron. To Arno Trautmann, for teaching me about the experimental setup, arduinos and for the willingness to clarify my doubts. For the origin of the *umlaut* too. To Tobias Rentrop, for the welcoming to the NaLi team, for teaching me about the NaLi experiment and

for the advices. To the New NaLi members! Kai, Apoorva, Jan, Manu, little Alex, Lilo: for the perfect environment in the office as well as in the lab. All the best for your projects.

- To the Matterwavers, for the cooperative working atmosphere and the discussions that helped us to progress in our experiment, and for the BBQs, pizza days, and Feuerzangenbowle!
- To Helmut, for all the inspiring conversations and for always having the time to help me solving our experimental difficulties.
- To Dagmar and Christiane, for all the organizational help that keeps the team running.
- To Jürgen Schölles and Mr. Azeroth from the electronics department, for the help when required. As well as to Mr. Spiegel and the people from the Diplomandenwerkstatt.
- A los amigos de acá, por toda la compañía a lo largo de los años. A Marcelo y a Nohora, por el apoyo, los momentos juntos y por la música, ¡que tocamos hasta en The Cave! Y junto con Agnese, Miguel y Alda por tantos buenos recuerdos. A todos los que compartieron de su tiempo estando acá: Gustavo, Priyata, Mauro, Felipe, Santi, Oscar, Ana María y muchos más. A lo lejos, a Mauro F. y a Gonzalo F., que cuando nos vemos, las conversaciones valen por todo el año. Y a tanta gente que ayudó a que este proceso sea aún mejor.

Thanks.

Gracias.

Bibliography

Erklärung:

Ich versichere, dass ich diese Arbeit selbstständig verfasst habe und keine anderen als die angegebenen Quellen und Hilfsmittel benutzt habe.

Heidelberg, den 27.07.2018 . . . . . .